Title

Understanding the Biophysical and Metabolic Regulations of the Epithelial Jamming Transition

Author

Bermudez, Alexandra Gabrielle

Publication Date

2024

Peer reviewed|Thesis/dissertation

UNIVERSITY OF CALIFORNIA

Los Angeles

Understanding the Biophysical and Metabolic Regulations of the Epithelial Jamming Transition

A dissertation submitted in partial satisfaction
of the requirements for the degree
Doctor of Philosophy in Bioengineering

by

Alexandra Gabrielle Bermudez

2024

ABSTRACT OF THE DISSERTATION

Understanding the Biophysical and Metabolic Regulations of the Epithelial Jamming Transition

by

Alexandra Gabrielle Bermudez
Doctor of Philosophy in Bioengineering
University of California, Los Angeles, 2024
Professor Neil Lin, Chair

Epithelial cells play a crucial role as they line every organ in our bodies and perform essential physiological functions. During the development of epithelial tissue, injury repair, or wound healing, these cells undergo cell crowding – a canonical tissue process where the cells continuously migrate and proliferate until they form a tightly packed, quiescent layer. To understand the underlying mechanism of such a "fluid-to-solid" transition in epithelia, researchers have successfully utilized the jamming transition framework to describe its physical control parameters including cell density, morphology, and motility. However, the molecular events governing these control parameters, as well as their downstream biological impacts, remain relatively underexplored. In my thesis, I developed a platform for investigating the modulus heterogeneity in a live monolayer to identify a correlation between cell size and stiffness, facilitating a deeper understanding of how cell mechanical properties influence morphological phenotype. I then combined transcriptomics and metabolomics to characterize cell behavior during crowding and identified the functional role of cell metabolism in regulating cell motility. I then described the origin of morphological heterogeneity in epithelial monolayers and how such heterogeneity can promote variations in gene expression.

The dissertation of Alexandra Gabrielle Bermudez is approved.

William M. Gelbart

Jimmy Kuanghsian Hu

Andrea M. Kasko

Amy Catherine Rowat

Gerard Chee Lai Wong

Neil Lin, Committee Chair

University of California, Los Angeles

2024

TABLE OF CONTENTS

LIST OF FIGURES

LIST OF TABLES

ACKNOWLEDGMENTS

I am grateful for the contributions and support from my team: Z.G., E.S., A.M., and Z.L., the Hu lab, and the Goldstein lab. I would also like to acknowledge my collaborators, family, partner, and all the taqueros in West LA for getting me through my Ph.D.. Lastly, I want to express my sincere gratitude for a mentor I highly respect and owe all my accomplishments to. Thank you for not only always believing in me, but teaching me how to believe in myself, N.Y.C.L..

VITA

2014–2018	B.S. in Physics University of California, Los Angeles Los Angeles, CA.
2018–2020	Teacher Excelsior Preporatory High School Arcadia, CA.
2020–2021	Teaching Assistant Bioengineering Department University of California, Los Angeles Los Angeles, CA.
2021–2024	Graduate Student Researcher Mechanical & Aerospace Engineering Department University of California, Los Angeles Los Angeles, CA.
2022–2024	Ph.D. Candidate Bioengineering Department University of California, Los Angeles Los Angeles, CA.

PUBLICATIONS

D. Choi, Z. Gonzalez, S.Y. Ho, **A. Bermudez**, and N.Y.C. Lin,"Cell-cell adhesion impacts epithelia response to substrate stiffness: Morphology and gene expression," *Biophysical Journal*, vol. 121, pp. 336–346. (Choi et al., 2022)

A. Bermudez, Z. Gonzalez, B. Zhao, E. Salter, X. Liu, L. Ma, M.K. Jawed, C. and Hsieh, and N.Y.C. Lin,"Supracellular measurement of spatially varying mechanical heterogeneities in live monolayers," *Biophysical Journal*, vol. 121, pp. 3358–3369. (Bermudez et al., 2022)

A. Bermudez, S. Negrete Muñoz, R. Blaik, A.C. Rowat, J. Hu, and N.Y.C. Lin, ,"Using Histologic Image Analysis to Understand Biophysical Regulations of Epithelial Cell Morphology," *The Biophysicist* (Bermudez et al., 2023)

CHAPTER 1

Introduction

Multicellular systems, such as epithelial cell collectives, undergo a fascinating transition reminiscent of inert physical systems like grains and foams. Initially adaptable, they can transition between a fluid-like state and a structurally stable, solid-like state — a phenomenon termed "cell jamming." While jamming and unjamming in multicellular collectives resemble those in granular collectives, understanding the origin of these phenomena and their implications for cell biology remains challenging. Specifically, although they adhere to the fundamental physics principles delineated by the jamming diagram, cell jamming and unjamming are inherently biological processes. In this introduction, I discuss how biological events, guided by biochemical and biomechanical cues, regulate this transition. This discussion focuses on the biological regulation of jamming axes that comprise the jamming phase diagram, with an emphasis on fluctuation (cell crawling) and geometric incompatibility, as well as the interplay between cytoskeletal activities, cell-cell interactions, and upstream signaling pathways that orchestrate cell crawling and morphology during this dynamic process.

Driven by internal forces, tissue patterning and reorganization involve locally controlling cell flux while maintaining global structural stability. This architectural change, which relies on the delicate balance between fluid-like deformability and solid-like structural integrity, is crucial for orchestrating development, guiding regeneration, and preserving tissue functions. To achieve such a balance, many multicellular systems, including epithelial cell collectives, can transition between a fluid-like, malleable state and a solid-like, structurally stable state, a process akin to familiar particulate systems like sand. Just as sand flows initially but becomes jammed as particles pack tightly, cell collectives undergo

a similar transition. Understanding the rheological aspects of cell jamming, such as transitions between viscoelastic liquids and solids, provides valuable insights into tissue behavior.

Cell jamming has been proposed to be governed by a universal phase diagram, similar to the traditional jamming transition observed in inert systems. In this introduction, I adopt a recently proposed version wherein jammed states are situated near the origin of a parameter space with axes representing inverse density, fluctuation, and geometric incompatibility. Both the density and fluctuation axes are directly derived from the classical jamming diagram. As the density of cells in a system increases, they become more crowded, eventually reaching a point where they have no space to move. The fluctuation axis describes cell crawling, providing cells with the energy to escape the "cage" created by their neighbors, akin to the role of temperature in glass transition. Finally, geometric incompatibility accounts for force balance between cells due to contractility, cell–cell adhesion, and cytoskeletal elasticity.

While whether a tissue is fluidized or solidified needs to adhere to basic physics principles described by the jamming diagram, such a process is essentially driven by biological events dictated by biochemical and biomechanical cues. Therefore, in this introduction, I provide a brief discussion on the molecular regulation of the jamming axes with a focus on the fluctuation (cell crawling) and geometric incompatibility. I will first describe four representative jamming and unjamming examples observed in in vivo and in vitro systems. I will then discuss how cell crawling and morphology are regulated by cytoskeletal activities and cell-cell interactions as well as their upstream signaling pathways.

1.0.1 Biology insights in cell jamming

Tissue development and injury repair require more than just biochemical signaling, in which cell jamming and unjamming have been implicated in multiple fundamental stages that underlie these processes. In this introduction, I discuss four representative in vivo

and in vitro settings that have been widely employed for studying cell jamming and unjamming.

1.0.1.1 Ventral furrow formation

Gastrulation is a fundamental embryonic development stage where a single-layered blastula (a hollow ball of cells, formed after the zygote cleavage) undergoes extensive morphogenetic changes to form the three primary germ layers: ectoderm, mesoderm, and endoderm. In Drosophila, gastrulation begins with the ventral furrow formation (Fig. 1a), where cells on the ventral side of the embryo fold inward, creating a furrow-like depression. This process, known as invagination, is one of the first steps of gastrulation and leads to the formation of the mesoderm, playing a key role in establishing the embryonic germ layers and body axis. To initiate ventral furrow, localized cell shape changes and actomyosin-driven contraction collectively induce invagination, influenced by mechanical cues from tissue tension. As cells undergo apical constriction, cell jamming stabilizes tissue structure. Ventral furrow formation is a biomechanically driven process, in which reduced junction integrity and myosin II activity result in diminished driving forces, leading to ventral furrow failure (Kasza et al., 2019; Brodland et al., 2010). Furthermore, the directional tissue flows arise from the interaction between myosin-driven tissue contraction and the embryo curvature (Gehrels et al., 2023). By analyzing the cell packing during ventral furrow formation, researchers found that cell shape and its variability are governed by a purely geometrical relationship, indicating a connection between jamming behavior and geometric constraint that transcends living organisms and physical systems (Atia et al., 2018; Bi et al., 2014; Schoetz et al., 2013). In the same system, two packing order parameters, volumetric and shear order parameters, have been proposed to distinguish the jammed and unjammed states (Yang et al., 2021). After the ventral furrow establishment, the germband is then formed through the invagination of cells on the ventral side of the embryo. During germband extension, cell alignment becomes crucial, along with cell shape, in determining whether the embryonic tissue exhibits characteristics of a solid-like or fluid-like state (Wang et al., 2020).

1.0.1.2 Blastoderm spreading

Another fundamental embryonic development stage is blastoderm spreading. Blastoderm forms during the blastulation phase when the zygote undergoes cleavage divisions, resulting in a hollow ball of cells called the blastula. This single-layered epithelium envelops the blastocoel, the fluid-filled cavity within the blastula, and serves as the precursor for the embryo's germ layers, which ultimately give rise to all the specialized tissues and organs. After blastulation, a blastoderm spreads to establish the embryonic axis and organize the future body plan of the embryo (Fig. 1b). This process involves a series of coordinated steps (Pinheiro et al., 2022), beginning with the expansion of blastoderm cells over the yolk surface, followed by convergence and extension movements that shape the embryonic tissue, all through the precise orchestration of cell movements and interactions. At the onset of spreading, the viscosity of the central blastoderm changes by roughly two orders of magnitude within 30 minutes, thereby initiating 'doming' movements (Petridou et al., 2019). In contrast to Drosophila furrow formation, in zebrafish blastoderm spreading, cell shape changes or packing configurations do not reliably predict the jamming and unjamming states. Instead, changes in the pattern of cell-cell contacts are a reliable proxy for the blastoderm viscosity (Petridou et al., 2021).

1.0.1.3 Wound healing

Modern study of epithelial wound healing can be traced back to early 20th century (Ross et al., 1970; BUSCHKE, 1949; Burrows, 1912) enabled by the maturation of light microscopy, but has only been recently considered as a jamming/unjamming transition. The wound healing process can be roughly divided into two steps. First, when a wound is introduced, epithelial cells at the wound edge migrate to re-epithelialize the exposed area, often accompanied by cell proliferation to replenish the lost cells (Fig. 1c). At this stage, the presence of a wound decreases the local stress on the boundary cells, inducing changes of the cell propulsion (Chepizhko et al., 2018), alignment strength (Chepizhko et al., 2018), and metabolism (Verstappe and Berx, 2023) that are subsequently transmitted

to the bulk cells, eventually leading to unjamming of the entire monolayer. Moreoever, tissue fluidity directly determines the wound healing speed, controlled by the intercelular junction tension and corresponding intercalating rate (Tetley et al., 2019). After the cells have closed the gap, they then re-establish adherens junctions and tight junctions to re-establish tissue integrity and barrier function. This stage of wound healing can be considered as a fluid-to-solid transition, which is usually studied using cell crowding models (Sadati et al., 2014; Angelini et al., 2011; Garcia et al., 2015).

1.0.1.4 Airway epithelium

During an asthma exacerbation, the airway undergoes narrowing, leading to epithelial buckling (i.e., tissue fold due to mechanical forces), resulting in exposure to compressive stress. This condition can be mimicked in vitro by subjecting cells to mechanical compression with a pressure differential of 30 cm-H2O from the apical to the basal side (Fig. 1d) (Park et al., 2015; Mitchel et al., 2020). Using primary human bronchial epithelial cells, it has been shown that the applied mechanical compression induces unjamming transition with elongated cell phenotype (Park et al., 2015). In this specific case, the cell shape elongation (shape index, cell perimeter divided by square root of area) acts as a predictor of the phase transition. Strikingly, such unjammed cells preserve many epithelial phenotypes such as apical-basal polarity, matured E-cadherin junctions and lack of epithelial-to-mesenchymal marker expression. This finding suggests that both the epithelial-to-mesenchymal transition and the unjamming transition may provide alternative gateways to cellular migration (Park et al., 2016).

1.0.2 Physics insights in cell jamming

One exciting perspective in using physics to understand complex systems is to identify emergent behaviors and self-organizing principles that arise from the constituent interactions. Jamming transition exhibits many hallmarks akin to conventional second-order phase transitions, demonstrating critical behavior near the transition point, characterized

by diverging length scales (Bi et al., 2011) and power-law trends (O'hern et al., 2003; Majmudar et al., 2007) without involvement of latent heat. In other words, jamming transition is characterized by universality, where systems with diverse microscopic details display similar macroscopic behavior near the critical point with shared critical exponents and scaling laws (Goodrich et al., 2016; Charbonneau et al., 2015; O'hern et al., 2003; Behringer and Chakraborty, 2018).

Because of the relatively established understanding in jamming transition across various physical systems, such as granular materials, colloidal suspensions, foams, emulsions, and glass-forming liquids, cell jamming studies often draw inspirations from these pioneering work. However, most experiments mainly focused on the changes in tissue structure, rheological properties, and dynamic heterogeneity. Studies of scaling and critical phenomena in cell jamming remain mainly theoretical.

1.0.2.1 Cell jamming phase diagram

While the jamming diagram elucidates how the system state can be predicted by its physical parameters, comprehending the mechanism of cell jamming requires understandings of the molecular regulation of these parameters. In cell biology, all three jamming axes (i.e., density, crawling, and geometry) are regarded as downstream phenotypes regulated by intricate signaling pathways and intracellular molecular events. This explains why jamming or unjamming often occurs when more than one axis is changing. A better understanding of the upstream control of these cell phenotypes will enhance our ability to manipulate them, enabling us to identify the primary mechanism driving jamming and unjamming. Fortunately, the fields of developmental biology and mechanobiology have amassed a wealth of knowledge on the mechanistic regulations of cell morphology and migration. This introduction aims to underscore several relevant findings concerning cell jamming to elucidate the close interplay among jamming axes. For simplicity, this introduction will focus on density-independent jamming, as cell number is generally maintained through a balance between proliferation and extrusion in a wide array of

biological processes.

1.0.2.2 Density-regulated cell jamming

In non-confluent tissues, each cell has the ability to move in various directions, such as left or right, and forward or backward in two dimensions. If we consider the cells as "hard spheres" for simplicity, the total number of degrees of freedom in this system is simply the number of cells (N_c) times the number of dimensions (d). As these "hard-sphere" cells become crowded, the contacts between them impose constraints on their movement, in which each intercellular contact adds one constraint. The system becomes jammed when the number of constraints matches the number of degrees of freedom $N_c d$. Conversely, in situations where the system is less dense and the number of contacts low, the cells can easily switch neighbors, allowing the tissue to "flow". Compared to ideal hard spheres, the first layer of complexity to consider in understanding density-driven cell jamming is that cells are soft and motile. Therefore, cell jamming always occurs beyond confluence, where glassy dynamics (Angelini et al., 2011; Sadati et al., 2014; Czajkowski et al., 2019) and cell size reduction (Devany et al., 2023) must be taken into account. Here, cells exhibiting glassy dynamics display sluggish movement, prolonged relaxation times, and a tendency to become trapped in metastable configurations, reminiscent of the behavior observed in glasses and amorphous materials. Second, intercellular interactions are typically adhesive, akin to "sticky particles". Thus, the density-driven cell jamming transition is more dictated by the percolation of cell network connectivity, which is based on the cell-cell adhesion. For example, zebrafish blastoderm exhibits a drastic viscosity change with a slight change in cell packing that readily determines the long-range connectivity of cells (Petridou et al., 2021), consistent with the findings in particulate jamming with attractive inter-particle forces (Trappe et al., 2001).

1.0.2.3 Density-independent cell jamming

Studies have revealed many density-independent pathways that lead to jamming and unjamming, which mostly happen in confluent tissues, where all cells are in contact with their neighbors and the packing density reaches a constant of unity. For instance, in the self-propelled Voronoi (SPV) model of confluent tissues, it has been demonstrated that the processes of unjamming and fluidization are driven by the magnitude of fluctuating propulsive forces, the persistence of these forces, and the strength of cell-cell adhesion (Bi et al., 2016, 2015). Using multiphase field models that describe the melting of a confluent layer of motile deformable particles, it has been shown that jamming and unjamming are intricately controlled by the trade-off between deformability and overlap of cells (Loewe et al., 2020). Predictions in simulations have been recently observed in experiments that utilized morphogen graident (Pinheiro et al., 2022), irradiation (Phung et al., 2023), hydrostatic pressure (Mitchel et al., 2020), or mechanical compression (Cai et al., 2022) to induce unjamming transition without significantly altering cell density.

1.1 Cell motility and jamming

1.1.1 Fluctuation-regulated cell jamming

The concept of fluctuation-regulated cell jamming was derived from the temperature axis of the original jamming diagram. An intuitive way to understand this jamming-unjamming mechanism is that as the system's temperature increases, the constituent element (e.g., an atoms, particles, or cells) gains more energy to escape the constraints imposed by its neighbors, fluidizing the system. In atomic systems, such as glassy liquids, the kinetic energy of atoms directly result from thermal fluctuations. In contrast, most systems that undergo jamming transition, such as granular and cellular systems, are far from thermodynamic equilibrium. For example, the particle kinetic energy in granular systems relies on the continuous energy injection through external mechanical perturbations. In cellular systems, the cell kinetic energy arises from the controlled release of chemical

energy stored in intracellular molecules. Therefore, the "temperature" of these far-from-equilibrium systems is often considered as a concept used to describe the thermal-like behavior.

In this introduction, the focus will be on the fluctuations associated with cell self-propulsion force, often referred to as motility in jamming studies. However, I aim to highlight recent works that generalize fluctuations. If we consider tissue fluidization as a series of structural changes, these changes can arise from two types of cellular events. The first type is T1 transition (i.e., cage escape), where a cell boundary shrinks to zero length, forming a fourfold vertex, which subsequently decomposes, creating a new cell bond. This process alters neighbor relationships while preserving cell numbers. Alternatively, tissue reorganization can result from cell division and extrusion, directly regulating tissue rheology. (Godard and Heisenberg, 2019; Siedlik et al., 2017; Ranft et al., 2010). Furthermore, the fluctuation of cells can be in the form of temporal fluctuation of junctional tension that arises from stochastic contractions due to turnover of junctional Myosin (Devany et al., 2019; Yamamoto et al., 2022; Krajnc, 2020).

1.1.2 Molecular regulation of cell motility

The biological coordination of cell motility involves the interplay of molecular signaling cascades, mechanical cues, and environmental influences. While cell motility has been extensively studied in developmental biology and mechanobiology, with significant progress made in understanding the mechanisms underlying single-cell and collective cell migration, its exploration within the context of unjamming transition remains limited. It is important to note two primary distinctions between unjamming studies and conventional collective cell migration systems as follows: (1) Typical collective cell migration studies, such as wound healing, chemotaxis, or durotaxis, exhibit directionality, with a global migration direction, unlike unjamming transitions where tissue-level cues are absent. Consequently, uncoordinated motion prevails, and the absence of a clear leading edge in the sample results in the absence of well-defined leader cells during tissue fluidization. (2) In motility-driven

unjamming experiments, intercellular adhesions are either maintained or strengthened, contrasting with the cell motility associated with the mesenchymal phenotype observed in collective migration. Despite of these differences, many fundamental mechanisms regulating cell motility discovered in cell migration studies are likely conserved across various settings. Specifically, I focus on discussing the role of cytoskeletal activity and cell-cell interactions in governing cell motion. At the molecular level, networks of signaling pathways, including those mediated by small GTPases such as Rho, Rac, and Cdc42, regulate cytoskeletal dynamics, cell adhesion, and protrusion-retraction cycles. These processes, in turn, determine the cell's ability to navigate through its microenvironment and interact with neighboring cells. By discussing these regulatory mechanisms, I provide a brief summary of how cells coordinate their movements within tissues, thereby driving jamming or unjamming phenomena.

1.1.2.1 Cytoskeletal activities

RhoA/Rac mutual inhibition The mutual inhibition between RhoA and Rac serves as an important regulatory mechanism orchestrating cytoskeletal dynamics and cellular motility. Within this machinery, activated RhoA inhibits Rac activity, while activated Rac reciprocally inhibits RhoA activation, creating a dynamic balance between the two GTPases. This regulatory feedback loop between RhoA and Rac then regulates cell motility through reorganizing cytoskeleton. For example, RhoA activates Rho-associated protein kinase (ROCK), which phosphorylates and activates myosin light chain (MLC), leading to actomyosin contractility and stress fiber formation. Rac, on the other hand, activates WAVE (Wiskott-Aldrich syndrome protein-family verprolin-homologous protein) complex, which promotes actin polymerization and branching, facilitating lamellipodia formation. As such, activation of RhoA leads to decreased cell protrusion and increased cell-substrate adhesion, favoring a static state. Conversely, activation of Rac promotes cell protrusion and reduces cell-substrate adhesion, favoring a more motile state. Importantly, the effects of RhoA and Rac on the cytoskeleton are often localized to specific regions of the cell, allowing for spatially coordinated cytoskeleton activity. During front-rear polarization,

Rac activation at the leading edge of cells promotes the formation of lamellipodia, while RhoA activity is concentrated at the rear of the cell, promoting contractility and retraction.

Several upstream regulators of the RhoA/Rac pathway have been identified, which control the activation or inactivation of these small GTPases in response to various extracellular signals. For example, activation of receptor Tyrosine Kinases (RTKs) via growth factor response leads to the activation of small GTPases including RhoA and Rac through downstream signaling pathways such as Ras and phosphoinositide 3-kinase (PI3K). Other regulators include Guanine Nucleotide Exchange Factors (GEFs), which catalyze the exchange of GDP for GTP on Rho GTPases, initiating their activation, while GTPase-activating Proteins (GAPs) accelerate the hydrolysis of GTP, leading to inactivation. Guanine Nucleotide Dissociation Inhibitors (GDIs) also regulate RhoA/Rac activity by sequestering Rho GTPases in the cytoplasm in their inactive GDP-bound form, preventing their interaction with membranes and downstream effectors. GDIs such as RhoGDI regulate the cycling of Rho GTPases between the cytoplasm and membrane which influence their activation state. Moreover, Regulators of G Protein Signaling (RGS), integrins, and cell-cell adhesion molecules can also modulate RhoA and Rac signaling pathways, integrating extracellular cues to regulate cellular responses. These upstream regulators integrate various extracellular signals to tightly control the activation state of RhoA and Rac, thereby regulating diverse cellular processes including cytoskeletal dynamics, cell migration, adhesion, and tissue organization.

Microprotrusions Another cytoskeletal feature observed in motile confluent epithelia is a microprotrusion, or cryptic protrusions. These dynamic microscopic structures facilitate cell locomotion and movement by exerting forces on the surrounding environment. Microprotrusions, encompassing filopodia and lamellipodia are primarily composed of actin filaments, in which actin polymerizes at the leading edge, mediated by Arp2/3 complex. Concurrently, myosin motor proteins contract actin filaments, generating propulsive forces necessary for cell migration. Adhesion molecules like integrins link the actin cytoskeleton to the extracellular matrix, providing traction for cell movement. Key

regulators of microprotrusion formation include Rho GTPases, which modulate actin dynamics and cell contractility. Rac1 and Cdc42 promote lamellipodia and filopodia formation, respectively, while RhoA regulates actomyosin contractility. Tyrosine kinases, such as EGFR and PDGFR, activate downstream signaling cascades that influence cytoskeletal dynamics and cell motility. Small GTPases like Ras and Arf also play pivotal roles in regulating microprotrusions through their involvement in signaling networks controlling actin polymerization and membrane trafficking. Moreover, integrins and cell-cell adhesion complexes transmit mechanical signals that impact cytoskeletal organization and protrusion dynamics.

1.1.2.2 Cell-cell interactions

Contact inhibition of locomotion (CIL) Contact inhibition of locomotion (CIL) refers to the phenomenon where the movement of a cell is inhibited upon physical contact with neighboring cells. At the molecular level, cell-cell adhesion molecules, such as cadherins, mediate the physical interactions between neighboring cells. Upon cell-cell contact, cadherins cluster at the junction between cells active various downstream signaling molecules, including Rho family GTPases. The activation of Rho GTPases leads to dynamic changes in the actin cytoskeleton via RhoA Rac1 and Cdc42 activity. Specifically, RhoA activation stimulates myosin II activity, leading to increased contractility of the actin cytoskeleton. Meanwhile, Rac1 and Cdc42 activation promotes the formation of actin-rich membrane protrusions, facilitating cell migration.

Front-rear cell polarization Another type of cell-cell interaction that regulates cell motility is front-rear polarization in pathways such as the gradient of RhoA-Rac activity and ERK signaling. Central to this process is the reorganization of the cytoskeleton, particularly through modulation of actin dynamics. As described in previous sections, RhoA, activated by factors like integrin signaling and cell-cell interactions, promotes actin polymerization and myosin-mediated contractility, leading to the formation of stress fibers and focal adhesions at the rear of migrating cells. Conversely, Rac activation

stimulates actin polymerization at the leading edge, facilitating lamellipodia and membrane protrusions.

A mechanism to establish and maintain the RhoA-Rac gradient in collectively moving cells is through ERK(Extracellular Signal-Regulated Kinase)-mediated mechanochemical waves. In migrating cells, mechanical forces between neighboring cells trigger ERK waves that travel in the opposite direction of migration. Activated ERK signaling triggers polarized rear contraction, inducing the pulling of the immediate following cells. To do this, ERK activation induces the accumulation of actin fibers and myosin phosphorylation at the cell periphery through the activation of Rho-associated kinases. Meanwhile, ERK signaling also strengthens cell protrusion through promoting actin capping and bundling.

1.2 Cell geometry and jamming

1.2.1 Geometry-regulated cell jamming

Because of geometric principles, all cell movements in confluent tissue requires geometric changes, and any cell passing its neighbor must induce cell rearrangements such as convergent extension (T1 transition) and intercalation (T2 transition). Geometry-regulated jamming has been mainly studied theoretically, primarily using vertex models (Farhadifar et al., 2007; Bi et al., 2015) and multi-phase models. In these simulations, the geometry-regulated jamming transition in tissues is governed by the 'shape index,' which represents the ratio of the preferred cell perimeter to the square root of the cell area. Tissues with a small shape index display rigidity due to geometrically incompatible cell arrangements, leading to energy barriers for cell rearrangement. Conversely, tissues with a large shape index allow for compatibility of neighboring cell shapes, leading to the fluidization of tissues as energy barriers associated with cell rearrangements disappear. In other words, cells fail to achieve target area and perimeter values in the jammed state, while in the fluid state, cells achieve both targets, yielding a ground state.

It is important to note that the geometry-regulated cell jamming is tension-driven,

in contrast to the repulsion-driven jamming in granular systems. Just as in tensegrity structures where isolated components are held together by tension, cells within a tissue are interconnected by intercellular junctions. When the junctional tension increases, akin to tension in a tensegrity structure, it restricts the cells' ability to rearrange or move freely, resulting in jamming. Such a mechanism is common in biopolymer systems (Storm et al., 2005; Koenderink et al., 2009; Rens et al., 2016).

1.2.2 Molecular regulation of cell geometry

The regulation of cell geometry involves a range of molecular events that control junctional tension and cell-cell adhesion. In recent decades, the vertex model has offered valuable insights into the mechanical aspects of cell geometry regulation. However, there has been a lack of extensive experimental research on the molecular regulation of cell geometry during the jamming transition. As such, I will draw principles from developmental biology to provide a concise overview of epithelial cell shape regulation during tissue development. Specifically, this introduction will concentrate on the regulation of junctional tension, as it directly influences cell shape by maintaining force balance. Additionally, I will discuss how cell-cell adhesion influences cell geometry by modulating cytoskeletal organization and activities.

1.2.2.1 Cytoskeletal activities

Essentially, the shape of cells is determined by networks of junctions that must maintain a mechanical force balance. According to D'Arcy Thompson's theory and the vertex model, the mechanical equilibrium of a cell monolayer is achieved by minimizing an energy function. This function entails each cell in the tissue striving to attain specific target areas and perimeters. These targets are primarily influenced by the tension in the junctions and the contractility of the cortex, both of which are directly controlled by cytoskeleton activity. The three components of the cytoskeleton—actin, microtubules, and intermediate filaments—each have unique roles in influencing cell morphology. However, they often

interact or affect each other when altering cell size and shape. Among these components, actin typically plays the dominant role. For instance, the balance of junctional tension, and thus cell shape, is primarily determined by cortical tension regulated by the actomyosin cortex. Cell area is mainly controlled by the contractile belt, which forms through cortical flows driven by increased myosin motor density at the cortex. These cortical flows align the actin filaments, enhancing cortical belt tension and reducing cell area.

The actin cortex consists of a network of crosslinked actin filaments located beneath the cell's plasma membrane. Its pivotal role in controlling cell shape arises from its attachment to the cell membrane and its capacity for contraction. Contractile forces are crucial; heightened contraction generally results in a reduced cell area, while non-uniform forces across the tissue can induce changes in cell shape and tissue remodeling. These forces are regulated by the alignment and positioning of actin, as well as the molecular control of the actin network. The primary components responsible for actin network contraction are actin filaments and myosin II. Their interaction gives rise to two types of contraction: myosin II motor-independent and myosin II-dependent contraction. Contraction independent of myosin II motor activity occurs through the polymerization and depolymerization of actin filaments. In myosin II-dependent contraction, myosin II serves as the primary force generator, converting energy into motion and interacting with the cytoskeletal network via its motor heads, which "walk" in an antiparallel manner along actin filaments to induce contraction. Even in myosin II-independent contraction, myosin II still functions as one of many crosslinkers that facilitate actin filament depolymerization and contraction, thereby reducing cell area. Both processes play crucial roles in cell contraction and can operate individually or in tandem.

In addition to actin, microtubules also play a role in regulating cell area and elongation. Microtubules primarily influence cell area by controlling cell height. The protrusion and reorganization of microtubules transition the cell from a squamous to a columnar morphology. Disruption of microtubules leads to a significant decrease in cell height and consequently an increase in cell area due to volume conservation. Moreover, aligning the microtubules along the apicobasal axis enhances cell elongation. The interaction between

microtubules and actin is crucial for regulating cell morphology. For instance, microtubules help balance actomyosin tension at proximal-distal junctions during polarization and control actomyosin organization, particularly junctional actin filaments. Microtubule shortening drives actomyosin contraction through stimulation of RhoA activity. These modulations of the actomyosin cytoskeleton also stabilize and regulate the junctional clustering of E-cadherin, thereby promoting the epithelial phenotype and corresponding cell morphology.

Intermediate filament networks, although less studied, also significantly influence cell morphology. Specifically, keratin intermediate filaments form extensive cytoskeletal networks that offer mechanical support to cells by bundling filaments. Due to their mechanical integrity, the positioning of intermediate filaments within the cell also governs cell shape. Similar to actin and microtubules, keratin filaments do not function independently. Disruption of contractile actin filaments leads to the reorganization of the keratin filament network. It is important to note that actin and keratin filaments form separate networks with distinct biomechanical properties. For example, keratin filaments are crucial for elasticity and flexibility, while actin filaments primarily contribute to contractile force and cell stiffness.

1.2.2.2 Cell-cell interactions

While cell-cell interactions do not biomechanically control cell geometry, they significantly regulate cell phenotype and actomyosin tension, thereby affecting cell morphology. Adherens junctions, for instance, facilitate the transmission of mechanical forces between neighboring cells, which is crucial for processes like morphogenesis and tissue remodeling. Cadherins serve as the principal structural components of adherens junctions, governing cortical actin organization. Specifically, the cadherin-catenin complex forms through the binding of cadherin adhesion molecules to cytoplasmic catenin proteins (such as β-catenin and α-catenin), which then connect to the actin cytoskeleton. These interactions confer mechanical strength to adherens junctions and regulate the dynamics of actin polymeriza-

tion, depolymerization, and bundling. Moreover, β-catenin can translocate to the nucleus and modulate gene expression, thereby influencing the expression of actin regulatory proteins at the transcriptional level.

As cell-cell junctions govern cytoskeletal dynamics, stabilizing these junctions is crucial for regulating cell shape. Actin filaments play a vital role in the assembly of adherens junctions, where the disruption of the cadherin-actin linkage can lead to the disorganization of adherens junctions, thereby altering cell shape. Moreover, the desmosome-keratin filament complex is pivotal for cell-cell adhesion, where desmosomal cell-cell junctions and keratin intermediate filaments act together as an opposing force to actomyosin contraction. Consequently, weakened interactions between desmosomes and keratin filaments can impair cell-cell attachment. Beyond actin and intermediate filaments, microtubules also impact adhesion by serving as tracks for delivering adhesive molecules, such as cadherins and integrins, to cell-cell junctions.

Lastly, recent studies have also highlighted the potential significance of tricellular junctions, specialized regions where three cells meet, in regulating cell geometry. Tricellulin, a primary protein component of tricellular junctions, plays a crucial role in organizing actomyosin during junction formation and controlling actomyosin contractility. Additionally, it regulates the configuration of cell-cell junctions at tricellular contacts. These contacts are particularly important for determining cell shape through junctional tension. Knockdown of tricellulin results in cells exhibiting irregular polygonal shapes with tortuous cell borders and impairs the organization of F-actin fibers at tricellular contacts during cell-cell junction formation.

CHAPTER 2

Supracellular Measurement of Spatially Varying Mechanical Heterogeneities in Live Monolayers

2.1 Overview

The mechanical properties of tissues have profound impacts on a wide range of biological processes such as embryo development (Handorf et al., 2015; Stooke-Vaughan and Campàs, 2018), wound healing (Darby et al., 2014; Valero et al., 2014; Smith et al., 2019; Wiegand and White, 2013), and disease progression (Wei and Yang, 2016). Specifically, the spatially varying moduli of cells largely influence the local tissue deformation and intercellular interaction. Despite the importance of characterizing such a heterogeneous mechanical property, it has remained difficult to measure the supracellular modulus field in live cell layers with a high-throughput and minimal perturbation. In this work, we developed a monolayer effective modulus measurement by integrating a custom cell stretcher, light microscopy, and AI-based inference. Our approach first quantifies the heterogeneous deformation of a slightly stretched cell layer, and converts the measured strain fields into an effective modulus field using an AI inference. This method allowed us to directly visualize the effective modulus distribution of thousands of cells virtually instantly. We characterized the mean value, standard deviation, and correlation length of the effective cell modulus for epithelial cells and fibroblasts, which are in agreement with previous results. We also observed a mild correlation between cell area and stiffness in jammed epithelia, suggesting the influence of cell modulus on packing. Overall, our reported experimental platform provides a valuable alternative cell mechanics measurement tool that can be integrated with microscopy-based characterizations.

2.2 Introduction

The mechanical properties of tissues play an essential role in regulating various biological processes and can be used as a biomarker for label-free, low cost, and rapid disease diagnosis (Handorf et al., 2015; Wells, 2013; Chiang et al., 2013; Sorba et al., 2019; Christ et al., 2010; Discher et al., 2005; Franze et al., 2009; Thompson et al., 2019). During embryogenesis, tissue viscoelasticity instructs the differentiation, migration, and organization of cells (Christ et al., 2010; Discher et al., 2005; Franze et al., 2009; Thompson et al., 2019). In developed organs, tissue stiffness regulates the cellular homeostasis and physiological functions (Handorf et al., 2015; Wells, 2013). In diseased organs, tissue modulus has been shown to act as a physical cue influencing the pathogenesis and progression of fibrosis (Wells, 2013), asthma (Polio et al., 2019), and Crohn's disease (de Bruyn et al., 2018). Moreover, the tumoral tissue elasticity has been found to correlate with malignancy, metastatic potential, and drug resistance (Gavara, 2017; Chiang et al., 2013).

To study these mechanically regulated processes, the ability to characterize cell modulus heterogeneities at the supracellular scale is critical. For example, cell migration is largely impacted by local cell stiffness, which determines the system's response to the intercellular force (Remmerbach et al., 2009; Lange and Fabry, 2013; Wang et al., 2002). This cell modulus variation has also been shown to induce cell competition that functions as a quality control mechanism by expelling "loser cells" (Amoyel and Bach, 2014; Di Gregorio et al., 2016). Recently, it has been demonstrated that this modulus-regulated cell competition can be harnessed as a defense against precancerous cells (Powell, 2019; Murphy et al., 2020).

While many pioneering cell stiffness measurement methods have been developed in the past few decades, characterizing the supracellular spatial distribution of cell modulus remains challenging. One of the earliest methods for measuring cell modulus is micropipette aspiration, a cost-effective technique that can track a sample's mechanical properties over time *in vivo* (Lee and Liu, 2014; Guevorkian and Maître, 2017). Although

micropipette aspiration can achieve a cell-level resolution, it does so in a low-throughput manner and requires cell detachment for characterizing adherent cells (Lee and Liu, 2014; Mierke). Atomic force microscopy (AFM) is currently the most widely used tool for studying adherent cell stiffness at a subcellular resolution. When using a pyramidal tip, the measured modulus, however, may correspond to a specific organelle which does not represent the overall cell stiffness, introducing uncertainties in interpreting the supracellular measurement (You and Yu, 1999; Müller and Dufrêne, 2011; Hoh and Schoenenberger, 1994). Moreover, depending on the indentation used or region probed, it can be difficult to distinguish the cellular contributions to the measurement from that of the substrate for penetration depths greater than 10% of the cell thickness (Gavara, 2017). Lastly, AFM cannot directly probe the in-plane modulus of the monolayer, which is more relevant to physiological processes compared to the transverse modulus typically acquired by AFM.

Another common technique is magnetic twisting cytometry (MTC), which is a high-throughput method able to characterize hundreds of cells by twisting magnetic microbeads that bind to membrane receptors (Zhang et al., 2017). The binding of the microbead to the cell surface, however, can induce formation of focal adhesion complex, which reorganizes the cytoskeleton and can alter cells' rheological properties. Additionally, the substrate can interfere with the MTC measurement, akin to AFM (Zhang et al., 2017). Similar to the working mechanism of MTC, a recent experiment used magnetic droplets to probe the local tissue stiffness. While this method addresses the cytoskeletal reorganization and substrate issues, it can be difficult to generate cell-scale ferrofluid droplets, which determine the spatial resolution of the measurement (Serwane et al., 2017). Cell shape based inference models are a non-perturbative approach for extracting a monolayer's mechanical property at the cellular or tissue level using microscopy (Gómez-González et al., 2020). In this method, only stress is directly determined, thus requiring independent local strain measurements to infer the modulus (Kong et al., 2019; Maître et al., 2016, 2015), in which this approach, however, has remained untested. Alternatively, cell stretchers are a versatile device that have been routinely used to characterize *in vitro* cell monolayer mechanics. It has been demonstrated that by either culturing cell

layers on thin elastomer substrates, or by detaching intact cell layers from the substrates, the overall monolayer stiffness can be determined using a stretcher (Sorba et al., 2019). Building upon these studies, we developed a monolayer mechanics measurement platform by integrating a custom-built stretcher, transmitted light microscopy, and AI inference. This integration allows us to directly visualize the heterogeneous effective modulus field in live cell monolayers. Additionally, we unmask the mechanical contributions of cells from the substrate by growing the cells on a soft (12.7 kPa) and thin (18.9 μm) biocompatible membrane (Figs. 2.1A and 2.1B). Our stretcher features an imaging window that enables us to conduct high-magnification transmitted light microscopy during experiments, which resolves the supracellular variation of cell deformation due to the applied strain. The AI inference model then converts the measured deformation field into an effective modulus field (Fig. 2.1C). Using this measurement platform, we characterized the effective modulus distribution in live epithelial (Fig. 2.1D) and fibroblast cell layers. These results allowed us to identify a mild correlation between cell moduli and morphological features in jammed Madin-Darby canine kidney (MDCK) cells.

2.3 Materials and Methods

Cell culture

MDCK cells were cultured in 1X Dulbecco's Modified Eagle media (Gibco, 11885084) supplemented with 5% fetal bovine serum (FBS) (Gibco, 16000044) and 1% penicillin–streptomycin (P/S) (Gibco, 15140122), where media was changed every 2 days. During weekly subculturing, ∼80% confluent cells were passaged using 0.05% trypsin-EDTA (Gibco, 25300054). 3T3 cells were cultured using the same base media but supplemented with 10% FBS and 1% P/S with all other conditions identical to that of the MDCK cells. MDCK and 3T3 cells were seeded using a density of 10,000 cells/cm^2.

PDMS membrane fabrication

To fabricate the polydimethylsiloxane (PDMS) membrane, we spin coated Sylgard 184 (base-curing agent ratio = 50:1) at a 2,000 RPM speed for 5 minutes on a glass coverslip that was previously coated with 10% (m/v%) polyvinyl alcohol (PVA) at a speed of 1,000 RPM for 2 minutes. We found that using concentrated 10% PVA for coating the sacrificial layer ensures membrane thickness uniformity. After attaching a cell stretcher jig to the PDMS surface, the composite was then cured at 150°C for 35 minutes. The PDMS-jig setup was autoclaved, treated with 25 μg/ml fibronectin (R&D Systems, 1030FN05M), and incubated at 37°C for 30 minutes. The sample was then washed with phosphate-buffered saline twice before seeding cells at a 10,000 cells/cm^2 density. During culture, the media dissolved the water-soluble PVA layer, lifting-off the PDMS from the coverslip.

To measure the stiffness of the PDMS, we fabricated and clamped 70 mm $\times$ 18 mm $\times$ 2 mm PDMS strips to an Instron 5944 and stretched it at a rate of 10 mm/min. The acquired stress-strain curves were used to calculate the Young's modulus by analyzing their slopes in the linear regime (Fig. 6.1). PDMS membrane thickness was characterized by optically imaging (40X objective) the cross-section of a PDMS layer on the coverslip (Fig. 6.1B) and measuring its thickness using ImageJ (Figs. 6.1C-E).

Cell stretching data acquisition and analysis

To prepare the cell-PDMS bilayer sample for stretching (Fig. 6.1F), the bilayer spanning the two jig legs was cut and then mounted to the cell stretcher as shown in Fig. 6.1G and 6.2A. Subsequently, media was added to the media chamber to submerge the sample, and the supportive T-bar was removed. The stretcher assembly (Fig. 6.2B) was placed on a microscope (Nikon Ti) and stretched the sample at a rate of 25 μm/sec until 5% strain (0.5%strain/sec), corresponding to a 250 μm stretch for a duration of 10 seconds. Simultaneously, differential interference contrast (DIC) images were acquired using a 10X objective (NA 0.45) at 20 fps. The acquired images were registered using the ImageJ plugin StackReg (Thevenaz et al., 1998), and used for particle image velocimetry

(PIV) analysis with PIVlab (Thielicke and Sonntag, 2021) to determine the displacement of cells between the initial unstretched image and the final stretched image. Strain-xx ($\epsilon_{xx} = \Delta u_x/\Delta x$), strain-xy ($\epsilon_{xy} = 0.5(\Delta u_y/\Delta y + \Delta v_x/\Delta x)$), and strain-yy ($\epsilon_{yy} = \Delta v_y/\Delta y$) values were calculated and assigned to points in the image using MATLAB, where Δu_x is x-displacement difference of x-adjacent elements, Δu_y is x-displacement difference of y-adjacent elements, Δv_x is y-displacement difference of x-adjacent elements, Δv_y is y-displacement difference of y-adjacent elements, Δx is x-position difference of adjacent elements, and Δy is y-position difference of adjacent elements.

Cell-PDMS bilayer mechanical measurement

To measure the overall sample stiffness, the cell-PDMS bilayer was cyclically stretched to 5% strain using the cell stretcher while force was recorded by a force transducer (FUTEK LSB201 LSB205 Load Cell). Following this, the media in the chamber was replaced with 0.5% trypsin-EDTA and the sample was incubated at 37 °C for cell detachment (Fig. 2.2A). After confirming cell detachment using light microscopy, the cell-free PDMS membrane was then again cyclically stretched to 5% strain while force was measured.

AI inference model training

To generate the datasets for training the strain-to-modulus AI inference, we performed a series of finite element analyses (FEA) that described the mechanical response of cell-PDMS bilayers under tensile strain. The PDMS and cell layers were individually modeled in 3D using triangular shell elements in Abaqus, in which the model parameters including cell mean modulus (4.0 kPa for MDCK and 12.2 kPa for 3T3 cells), cell height (9.2 mum for MDCK and 6.3 μm for 3T3 cells (Liu et al., 2019)), Poisson ratio (0.5 for both MDCK and 3T3 cells (Schulze et al., 2017; Harris et al., 2012)), PDMS modulus (12.7 kPa), and PDMS thickness (18.9 μm), were either taken from previous studies or determined experimentally (Fig. 6.1). We discretize the finite element to 16,638 three-node elements, in which the size of the FE mesh is controlled to be $\sim$ 8.3 μm. This fine mesh setting

allows us to vary the length scale of heterogeneities in FEA simulations on supracellular scales, in which all data were included for AI model training.

The cell layer and PDMS membrane were modeled as incompressible elastic materials. We impose material continuity in simulations, suggesting that the cell layer mechanically interacts with its surroundings, where the interpretation of such continuity may have different implications depending on the size of the cell. Specifically, for small (10-15 μm) MDCK cells, this continuity implies that cells are directly interacting with neighboring cells, whereas in larger ($\sim$ 50 μm) 3T3 cells, this continuity implies continuity of cellular components within a cell.

To simulate cell modulus heterogeneity, we generated random cell modulus fields from normal or log-normal distribution with a standard deviation ranging from 30% to 70% of the mean modulus. In simulation, one side of the sample was uniaxially stretched to 5% strain where a non-slip boundary condition was applied at the cell-PDMS interface.

In other cell stretching experiments, cell-substrate adhesions have been observed to remain intact and stable, especially for short time and length scales (Kreutzer et al., 2014; Bartalena et al., 2011; Gong et al., 2018). The displacement of individual cells was recorded, and the corresponding strain fields were calculated (Fig. 6.3A). The resulting strain (ϵ_{xx}, ϵ_{xy}, and ϵ_{yy}) and modulus fields were loaded into the AI model training framework, as summarized in Fig. 6.3B.

Statistical analysis

Data were reported as mean values $\pm$ standard deviation. Statistical analysis was performed using OriginLab. Statistical significance was determined using paired t-tests. Significance levels are indicated with asterisks in each figure. P-values less than 0.05, 0.01, and 0.001 were denoted by *, **, and ***, respectively.

2.4 Results

Visualizing monolayer mechanical heterogeneities

To visualize the spatially varying mechanical properties of cell monolayers, we cultured MDCK cells on a PDMS membrane (Fig. 2.1B) and imaged its heterogeneous response to a tensile strain. During stretching, the tested cell-PDMS bilayer behaves analogously to a spring system, in which individual cells with different moduli can be considered as springs with different spring constants Fig. 2.1A). In this approach, it is critical to use a thin, soft, and freestanding PDMS membrane to prevent the substrate from masking the cell contribution to the overall strain response. Stretched elastomeric membranes such as PDMS have been routinely used to demonstrate uniform displacement fields and have been widely used for characterizing cell deformation (Ghosh et al., 2021; Seelbinder et al., 2020; Friedrich et al., 2019).

The freestanding PDMS membrane was fabricated by adapting a previous protocol (Boulogne et al., 2016; Addae-Mensah et al., 2007) in which a sacrificial PVA layer was utilized to facilitate the membrane lift-off process, as described in *PDMS Membrane Fabrication*. We then mounted the sample on our custom-made cell stretcher, which features an imaging window that is compatible with inverted microscopy and functions as a cell culture media reservoir (Fig. 6.2A). The piezomotors of our stretcher provide stretching motion stability to ensure imaging focus during experiments. To prevent folding and tearing of the thin bilayer, the two jig legs that suspend the sample are fixed by a connecting T-bar during handling, which is then removed after sample mounting (Fig. 6.1G).

To confirm that the mechanical contribution from the cells can be observed in our bilayer system, we used a force transducer to measure the stress response difference between the cell-PDMS bilayer and PDMS-only samples. We first measured the effective modulus of the bilayer and repeated the measurement for the cell-free PDMS membrane by enzymatically detaching the cells (Fig. 2.2A). This procedure is similar to the cell removal

protocol routinely used in traction force microscopy for characterizing the substrate deformation (Plotnikov et al., 2014; Sabass et al., 2008). As shown in Fig. 2.2B, we found that the cell-PDMS bilayer stress-strain curve exhibited a slope greater than that of the cell-free PDMS, which is attributed to the mechanical contribution from the cell layer. Using the spring analogy as depicted in Fig. 2.1A, we then calculated the cell monolayer modulus (Fig. 2.2C) E_c:

$$E_c = \frac{E_b(A_m + A_c) - E_m A_m}{A_c} \sim 4.0 \pm 1.5\, kPa \tag{2.1}$$

Here, $E_b = 16.7 \pm 1.5$ kPa, $E_m = 12.7 \pm 4.2$ kPa, $A_m = 18.9 \pm 0.5$ μm, and $A_c = 9.2 \pm 0.7$ μm is the bilayer effective modulus, membrane modulus, membrane cross-sectional area, and cell monolayer cross-sectional area, respectively for MDCK samples. In MDCK FEA simulations, E_c was used as the mean modulus, and A_c was determined using confocal microscopy (Fig. 6.1F). The remaining parameters were determined as described in *AI inference model training*. In addition, using a similar measurement approach, MDCK cells treated with 25 μM blebbistatin for 24 hours exhibited a 3-fold lower modulus compared to untreated MDCK cells (Figs. 6.4A-D). This finding further validates that the PDMS membrane can reveal the mechanical contribution arising from the cell layer.

After validating the mechanical contribution from cells in our bilayer samples, we mounted the stretcher on a microscope and applied a 5% tensile strain to a cell-PDMS sample while simultaneously imaging cell deformation. With the acquired image data, we performed PIV to determine the displacement field (Fig. 2.2D) resulting from the stretch. Since our applied tensile deformation is symmetric, the displacement field shows minimal x-y translation which maximizes the analyzable field of view.

We then calculated the corresponding strain fields, where the components (ϵ_{xx}, ϵ_{xy}, and ϵ_{yy}) are shown in Figs. 2.2E-H. Specifically, we found that ϵ_{xx} has a mean of $\sim$ 4.9%, which was consistent to the applied global strain value. In agreement with previous studies (Vincent et al., 2015; Serra-Picamal et al., 2012), we observed spatial fluctuations in all strain components which suggest the presence of mechanical heterogeneity in the

tested MDCK monolayer. For example, ϵ_{xx} had a relative standard deviation of $\sim 20\%$. Additionally, we found that ϵ_{xy} and ϵ_{yy} have mean values and fluctuations an order of magnitude less than that of ϵ_{xx} (Fig. 2.2I), which was anticipated since the stretch was applied uniaxially in the x-direction. Importantly, all these values are greater than the strain uncertainty associated with PIV limitations (Nobach and Bodenschatz, 2009). Furthermore, the high image resolution (1 pixel ~ 0.65 μm) of our system allowed us to visualize strain field heterogeneity at the cellular level. As shown in Fig. 2.2F, we found that the strain fluctuation of ϵ_{xx} spans a few cells. This finding is consistent with the cell mechanical heterogeneity found in AFM measurements (Fujii et al., 2019) and free-standing epithelium stretching experiments (Harris et al., 2012).

Converting strain responses to modulus fields

The strain field of a deformed material is directly determined by the moduli of its constituents and the globally applied strain. Conversely, having access to the strain components of cells within a stretched cell monolayer allows us to infer the effective modulus field from the strain fields. However, converting strain fields into a modulus distribution can be challenging due to their complex relationship in structurally disordered and mechanically heterogeneous systems. In our approach, the deformation of a cell is influenced by both its own stiffness and the surrounding modulus field. Thus, the determination of local effective modulus values requires the knowledge of the entire strain fields for all components, rather than just the value at a local position. To capture such a high-dimensional strain-modulus relationship, we employed a U-net based neural network architecture that analyzes both strain and modulus fields across multiple length scales. Specifically, our AI model utilized a generator and a discriminator, which are both convolutional neural networks (Fig. 2.1C). The generator network was based on a U-Net architecture (Ronneberger et al., 2015; Ounkomol et al., 2018) and learned the nonlinear relationship between the FEA simulated ϵ_{xx}, ϵ_{xy}, and ϵ_{yy} distributions and its corresponding FEA simulated modulus distribution. During the training process, the neural network minimizes the loss function by calculating the pixel-to-pixel differences

between the prediction and target. Here, the target is the FEA simulated modulus distribution of a cell layer. Our three strain inputs first propagated through the U-Net, where the resulting generator output (predicted modulus) was loaded into the discriminator network. The discriminator network then used a conditional generative adversarial network (cGAN) (Isola et al., 2017) to estimate the probability of similarity between the predicted and target image. The discriminator output, which is an adaptive loss function, is iterated over a set number of cycles through the model to optimize the prediction. Once this iteration process is completed, the resulting trained model was used for predicting effective modulus distributions of cell layers from experimental ϵ_{xx}, ϵ_{xy}, and ϵ_{yy} distributions. Similar methods have been commonly utilized in a wide range of 2D field conversion tasks including the translation, segmentation, and classification of image data (Elitas and Sengul, 2021; Zhang et al., 2019; Hashemi-Beni and Gebrehiwot, 2020).

To train our AI model, we used FEA to numerically model a stretched bilayer system that closely recapitulates the heterogeneous modulus distribution in the cell monolayer. Specifically, since our experiment operates on the time scale of seconds, we model our cell and PDMS layer individually as elastic materials (Khalilgharibi et al., 2019; Pajic-Lijakovic and Milivojevic, 2019; Thoumine and Ott, 1997). Here, we assume a non-slip boundary condition between the cell and PDMS layers such that the applied strain results in a direct mechanical deformation of cell layer (Figs. 6.5A-C). This training framework is synthetic data-based, which has been commonly used in vision research, and shown to yield robust and traceable AI prediction performance (Liu, 2019; Tallman et al., 2019). More importantly, the use of FEA data grants us access to the strain inputs ϵ_{xx}, ϵ_{xy}, and ϵ_{yy} and the corresponding modulus outputs (i.e., ground truth), which is infeasible to obtain experimentally. The AI model was trained by utilizing the generated FEA data to infer the general strain-modulus relationship, which was used to construct a conversion function capable of determining the effective modulus field from experimental strain fields.

To characterize the AI prediction accuracy, we compared the ground truth (i.e., modulus distribution assigned in FEA) to the AI predicted effective modulus field (Fig. 2.3A and Fig. 6.6A). Additionally, to test whether a single-component strain measurement

would be sufficient for inferring the effective modulus field, we included an ϵ_{xx} predicted modulus distribution, which was obtained by using the best fit between FEA simulated ϵ_{xx} and modulus values (Fig. 6.6B). We found that while the effective modulus field can be roughly estimated using solely the tensile strain component, ϵ_{xx}, the most accurate effective modulus field is inferred by considering the spatial distribution of all three strain components. As shown in Fig. 2.3A, the AI prediction captures both the localization and fluctuation level of the modulus ground truth significantly better than the ϵ_{xx} prediction, suggesting that some mechanical heterogeneities are only reflected in the spatial distribution of ϵ_{xy} and ϵ_{yy}.

To quantify the accuracy of different effective modulus prediction methods, we calculated the Pearson correlation coefficient between ground truth modulus values and the values predicted using the AI, ϵ_{xx}, ϵ_{xy}, and ϵ_{yy} inferences. Our results, shown in Fig. 2.3B, suggest that the strain components ϵ_{xy}, and ϵ_{yy} alone do not provide adequate information for predicting modulus. Furthermore, we found that the AI prediction accuracy (correlation ~ 0.91) is significantly higher than that achieved by ϵ_{xx} prediction (correlation ~ 0.66). This finding confirms our hypothesis that the spatial distribution of all strain components are required to accurately predict the effective modulus field. We also found that the high accuracy of AI prediction can be achieved by training the model within 400 FEA data sets (Fig. 6.6C). Lastly, compared to conventional reverse problem approaches (Cho et al., 2007; Varady et al., 1997; Martin et al., 1997), our AI-based forward method enables us to overcome technical solution limitations such as existence, uniqueness, and continuity, which are requirements for solution stability (Bertero et al., 1980).

Spatial distributions of cell moduli

We applied our AI model to convert the MDCK strain data into an effective modulus field (Figs. 2.4A and 6.7A). The resulting MDCK effective modulus was 4.0 kPa $\pm$ 1.5 kPa ($\sim$38% fluctuation), in which its probability distribution can be approximated by a Gaussian function (Fig. 2.4B). Compared to literature values obtained from AFM, our

measured mean effective modulus is of the same order of magnitude (Fig. 2.4B), in which the differences may be attributed to different levels of jamming and substrates used (Fujii et al., 2019; Nehls et al., 2019; Pietuch et al., 2015). The similarity between our modulus and AFM measurement may suggest that the in-plane elastic modulus (stretching) is comparable to the transverse elastic modulus (AFM) in MDCK cells, implying that the cellular and organelle structural anisotropies do not necessarily lead to cell modulus anisotropy. We also characterized the length scale of the effective modulus fluctuation by calculating the spatial autocorrelation function:

$$C(\vec{d}) = \frac{\langle (E(\vec{x}+\vec{d}) - \bar{E})(E(\vec{x}) - \bar{E}) \rangle_{\vec{x}}}{E_{var}} \tag{2.2}$$

Here, $E(\vec{x})$ is the effective modulus value at position $\vec{x}$, whereas $\bar{E}$ and E_{var} are the mean and variance of the effective modulus, respectively. For simplicity, we plot the radial part of the correlation function (i.e., using the magnitude of $\vec{d}$ as the variable) in Fig. 2.4C. As shown, we observed an exponential decay $\sim e^{-d/45.2m}$, suggesting a correlation length of $45.2m \sim 3$ cells. Our measurement is consistent with the intercellular modulus correlation determined using AFM, confirming the spontaneous modulus correlation in jammed epithelial monolayers (Fujii et al., 2019).

To demonstrate that our approach is compatible with other adherent cell types, we implemented the same experimental approach to characterize 3T3 fibroblast cell layers (Figs. 2.4D and 6.7B). Consistent with previous studies (Guimarães et al., 2020; Luo et al., 2016; Michaelson et al., 2012; Hutter et al., 2005; Fujii et al., 2019; Nehls et al., 2019; Pietuch et al., 2015), we found that 3T3 cells exhibited a higher mean effective modulus (12.2 kPa) compared to MDCK cells (4.0 kPa) (Fig. 2.4E) . Moreover, we observed that the 3T3 culture shows a greater effective modulus fluctuation than that of MDCK (Fig. 2.4F). The large effective modulus fluctuation may be related to the differences in underlying cytoskeletal activity observed in 3T3 cells (Rotsch et al., 1999) We also found the correlation length of 3T3 cell effective modulus is approximately half that of MDCK cell effective modulus (Fig. 2.4G). As suggested by previous studies, the

relatively long correlation length of MDCK effective modulus might be associated with their intercellular adhesions (Fujii et al., 2019). We acknowledge that unlike MDCK monolayers, there are no intercellular junctions present in 3T3 monolayers, and thus the lack of such junctions may not be captured in the continuity assumption imposed in our FEA simulations. Nevertheless, the space between cell boundaries only occupied roughly 5% of the analyzable field of view (Figs. 6.7A and 6.7B), suggesting that a majority of the heterogeneity observed is within the cell, and can therefore be interpreted as cellular mechanical heterogeneity.

Since our effective modulus measurement is microscopy-based, we can additionally evaluate the morphological phenotype of cells under tensile strain. This capability enabled us to investigate the relationship between effective modulus and morphology in MDCK cells. We analyzed and plotted cell moduli as a function of four morphological features: cell area (Figs. 2.4H and 6.8A), aspect ratio (Figs. 6.8B and S8C), circularity (Figs. 6.8D and 6.8E), and shape index (Figs. 6.8F and 6.8G). Overall, the distribution of raw data did not show a visually obvious correlation between cell effective modulus and area. The difficulty to visualize such a correlation is associated with the relatively narrow distribution of cell size, in which most data points are between the area of 200 m^2 and 400 m^2. To balance the contributions from the data points outside this range, we resampled the data such that cells across the range of area are randomly selected with equal probability. Specifically, we resampled the data so that there was an equal number of cells in bins of 50 m^2. The resampled dataset then revealed a mild effective modulus-area correlation that was previously masked (Fig. 6.8A). Using the same data sampling approach, we also analyzed the cell aspect ratio, circularity, and shape index, in which we did not observe a strong correlation with cell effective modulus (Fig. 2.4I).

Our modulus-area result suggests that the cell modulus may play a role in determining the size of large cells. This finding is consistent with previous studies (Nehls et al., 2019). Biological stochasticity (e.g., gene expression fluctuation and asymmetric cell division) and local geometric constraints have been identified to largely influence cell morphology in jammed epithelia. For example, cells that assemble more stress fibers and spread out

more have been shown to be stiffer (Vichare et al., 2012; Tee et al., 2011; Stroka and Aranda-Espinoza, 2011). Additionally, the local force balance in jammed systems is often achieved by compressing the softer constituents and reducing their size. Alternatively, it is also possible for the converse of this hypothesis to be true, such that cell morphology instead may play a role in regulating cell modulus, although further studies such as micropatterning experiments or inhibition of specific signaling pathways are required to validate these hypotheses.

2.5 Discussion

We reported a microscopy-based cell mechanics characterization platform that allows visualization of supracellular modulus heterogeneities. Our method measures the heterogeneous strain fields in a stretched cell-PDMS bilayer, and converts them into an effective modulus field using an AI-based inference. Using this approach, we measured the effective modulus distribution in MDCK (4.0 ± 1.5 kPa) and 3T3 (12.2 ± 3.1 kPa) cell layers. Our measured effective mean modulus values, standard deviations, and correlation lengths are in agreement with previous studies (Rotsch et al., 1999; Pietuch et al., 2015; Nehls et al., 2019). Furthermore, we observed a mild correlation (Pearson correlation coefficient ~ 0.24) between MDCK cell modulus and area, implying that the cellular stiffness may affect the size and packing of jammed epithelial cells. Collectively, our reported experimental platform and results can provide useful cell mechanics information for improving theoretical models of epithelial jamming (Fujii et al., 2019), collective migration (Ebata and Kidoaki, 2021), and homeostasis (Cox and Erler, 2011), all of which can be influenced by cell stiffness heterogeneity (Handorf et al., 2015).

In our method, we applied a 5% tensile strain to reveal the cell modulus heterogeneity. While such a strain can potentially induce changes in cell behavior, cell stretching experiments are considered relatively non-perturbative (Cui et al., 2015; Kamble et al., 2016; Wang et al., 2005) compared to contact-based cell mechanics measurements (Schaus and Henderson, 1997). In future studies, we aim to reduce the applied strain by improving

the imaging resolution and PIV accuracy. In addition, because our stretching experiment operates on the time scale of seconds, we consider the cell layer viscoelasticity, which typically emerges on the time scales of minutes to hours (Esfahani et al., 2021; Pajic-Lijakovic and Milivojevic, 2019; Thoumine and Ott, 1997; Schulze et al., 2017; Khalilgharibi et al., 2019; Harris et al., 2012; Kubitschke et al., 2017; Sorba et al., 2019), relatively negligible. Furthermore, the timescale of seconds prevents the cell-substrate contacts from rearranging as this typically occurs on the timescale of minutes, and thus ensures the imposed non-slip boundary condition. Overall, our relatively short timescale of stretching primarily probes the elastic response of cell monolayers, which was captured by our FE model. A limitation of our current inference model is that any experimental strain measurement error would lead to AI prediction error, since the FEA strain fields used for training the inference model do not contain any noise. In the future, it would be useful to implement other AI training frameworks including data augmentation and neural network perturbations to improve the robustness of the inference model (Wang et al., 2019; Mikołajczyk and Grochowski, 2018; Kong et al., 2021; Mustafa and Mantiuk, 2020; Romero et al., 2019).

Similar to other stretching experiments, our method requires growing cells on soft substrates, which can potentially alter cell properties (Discher et al., 2005; Yeung et al., 2005; Tee et al., 2011). For example, it has been shown that cells exhibit a lower modulus when cultured on a soft substrate (Chiang et al., 2013; Jalali et al., 2015). While our previous work has shown that jammed epithelial cells with well established intercellular adhesions are not strongly influenced by substrate stiffness (Choi et al., 2022), it would be useful to conduct further cell mechanics measurements in future experiments. We also acknowledge that the PDMS substrate uniformity plays an important role in our measurement. While it would be ideal to characterize the substrate uniformity of the specific substrate used in experiments, doing so proved to be technically challenging since introducing detectable particles to our substrate for PIV to track significantly altered the local mechanical properties of such a thin, soft substrate. Nevertheless, previous work has demonstrated the mechanical homogeneity of similar elastomeric substrates

also used in stretching experiments by calculating the strain resulting from the applied deformation using traction force microscopy (Seelbinder et al., 2020). The results of such an experiment demonstrate a uniform strain distribution under 10% strain. In addition, other past works have shown that PDMS produces equiaxial and uniform strain fields under stretching (Kreutzer et al., 2014; Bartalena et al., 2011), and that both stretched and unstretched PDMS substrate homogeneity has been validated by measuring the modulus of three distinct spatial locations on the substrate, in which all were in statistical agreement with one another (Boulter et al., 2020).

Our effective modulus measurement approach is a useful alternative tool for conducting supracellular-level mechanics studies that require simultaneous access to microscopy. For example, our system can be used for investigating the relationship between cell signaling, gene expression, and mechanics in developing or injured tissues. Moreover, our stretcher is compatible with microscope on-stage incubators, enabling the characterization of the effective modulus field evolution in cell monolayers that undergo phenotypic changes. Such measurements could be utilized to identify mechanical signatures in the development of fibrotic diseases and solid tumors (Handorf et al., 2015).

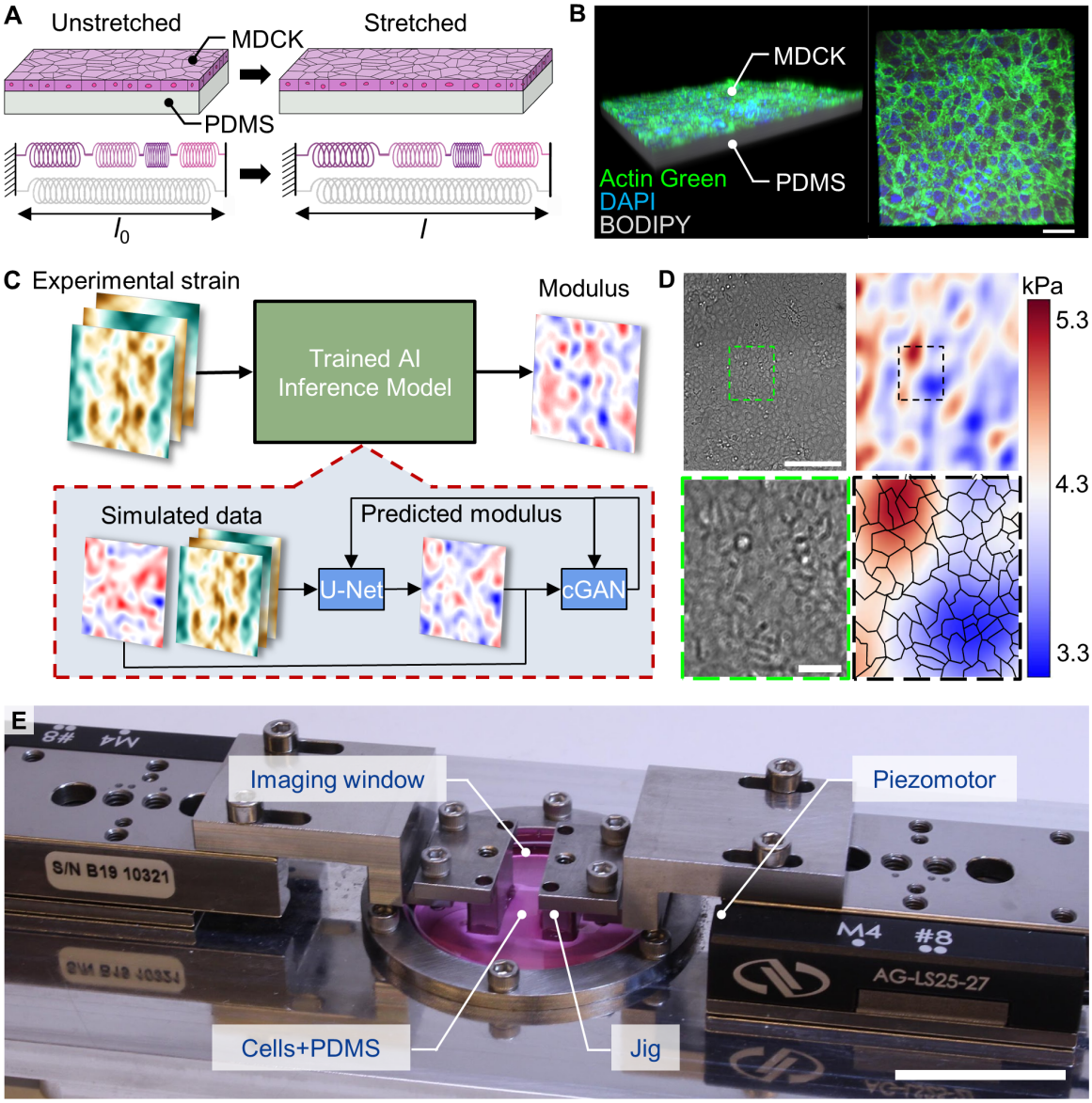

Figure 2.1: Visualization of mechanical heterogeneities in cell monolayers (A) By growing a cell monolayer (MDCK) on a ultrasoft PDMS membrane, the cell mechanical heterogeneity, which is illustrated by distinct Hookean springs, can be revealed by stretching the bilayer system. (B) 3D reconstruction of a cell-PDMS bilayer tested in our experiment. (C) An AI inference model is used to convert experimentally measured strain fields into effective modulus distributions, in which the inference model (cGAN U-Net) is trained using finite element analysis data. (D) Example DIC (left) and effective modulus (right) data of MDCK cells. Dashed box indicates the zoom-in area. (E) Our cell stretcher applies a uniform tensile strain to a free-standing cell-PDMS bilayer suspended by the jig legs, using piezomotors. The imaging window allows for microscopy while containing the media during experiments. For B, scale bar = 50 μm. For D, scale bars = 200 μm and 50 μm for top and bottom images, respectively. For E, scale bar = 2.5 cm.

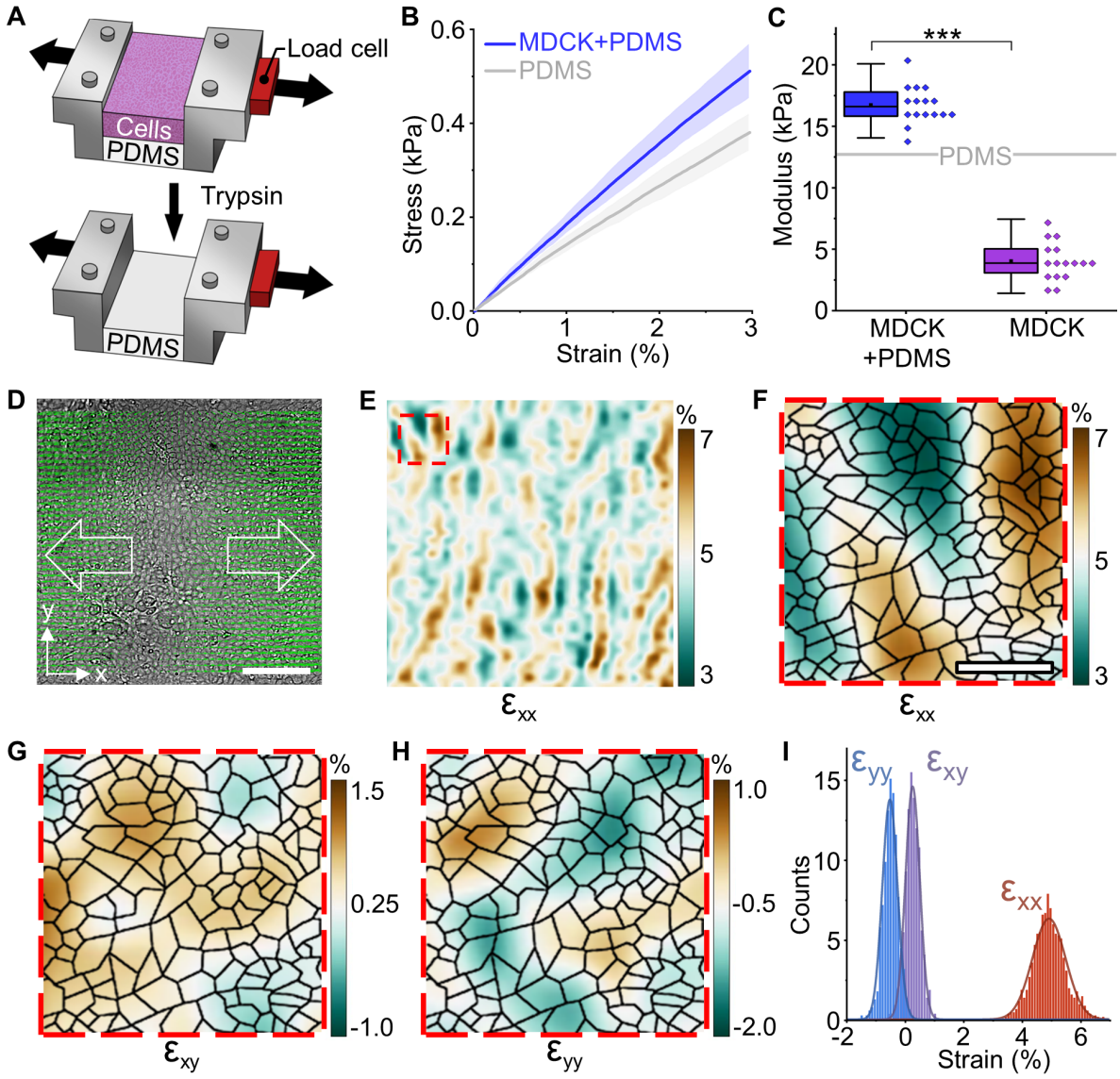

Figure 2.2: Heterogeneous strain responses in MDCK monolayers
(A) After measuring the effective modulus of the cell-PDMS sample, we used trypsin to detach the cells and measured the cell-free PDMS membrane modulus. (B) Stress-strain curves for cell-PDMS (MDCK+PDMS) and PDMS samples. Shaded area denotes the standard deviation. (C) Using the Hookean model illustrated in Fig. 2.1A, MDCK stiffness (4.0 $\pm$ 1.5 kPa) was estimated using equation (1). n = 16. (D) DIC image of a stretched MDCK sample annotated with displacement fields. (E) Heatmap of the *xx* component (ϵ_{xx}) of strain calculated from the displacement field in (D). (E-H) Close up of (E) showing heatmaps of ϵ_{xx}, ϵ_{xy}, and ϵ_{yy}, respectively. (I) Histograms for all strain components fitted by Gaussian curves. Scale bar for D-E = 200 μm. Scale bar for F-H = 50 μm.

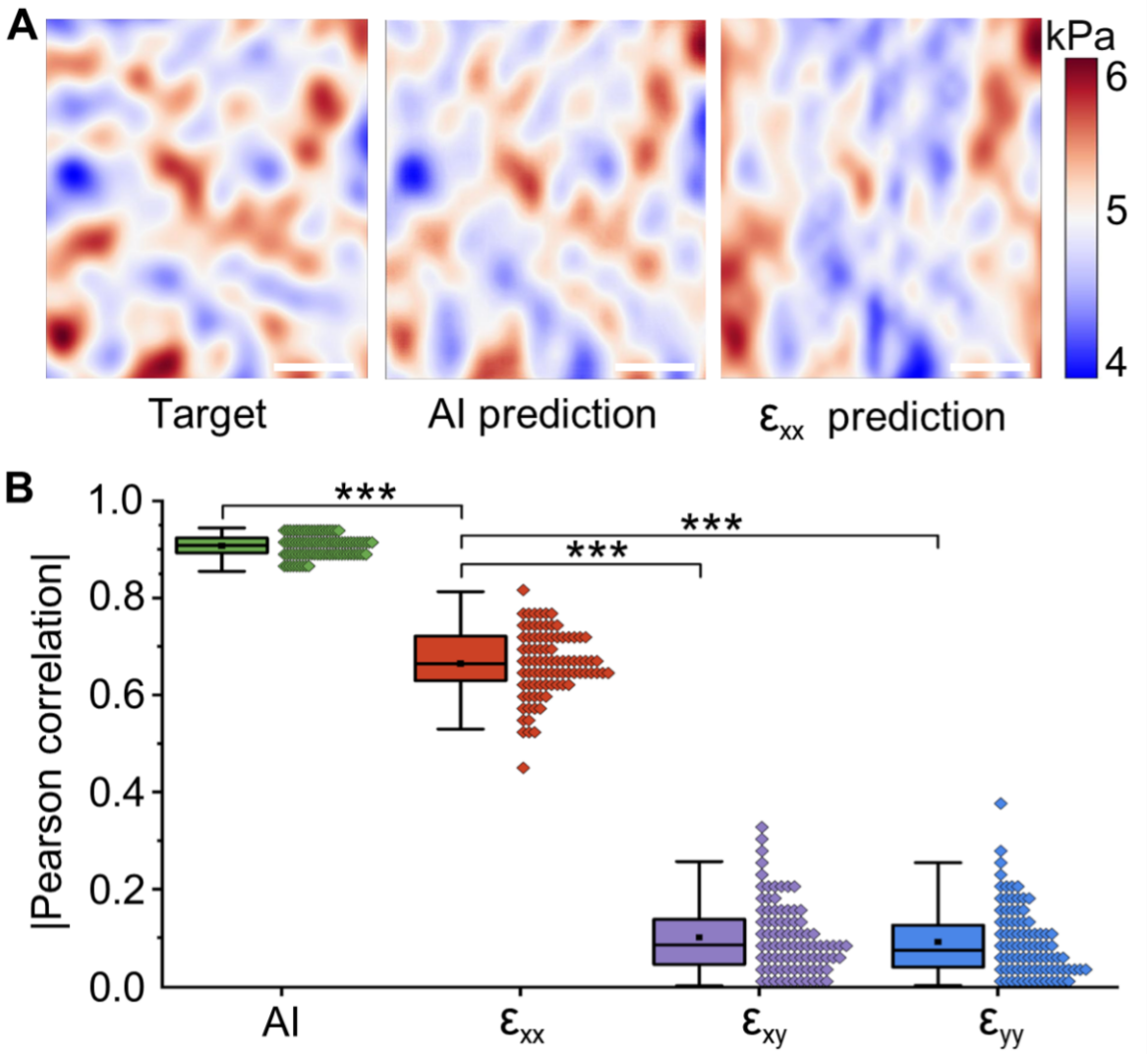

Figure 2.3: Strain-modulus AI inference

(A) Comparison of the modulus fields generated by FEA simulation (Target), predicted by the AI inference model, and predicted from only strain-xx values. (B) Pearson correlation between the target modulus values and predictions made using the AI inference, ϵ_{xx}, ϵ_{xy}, and ϵ_{yy}. We found that ϵ_{xx} exhibits a higher correlation than xy and yy components, and AI-predicted values are significantly more correlated than ϵ_{xx}. Scale bars for A = 200 mum.

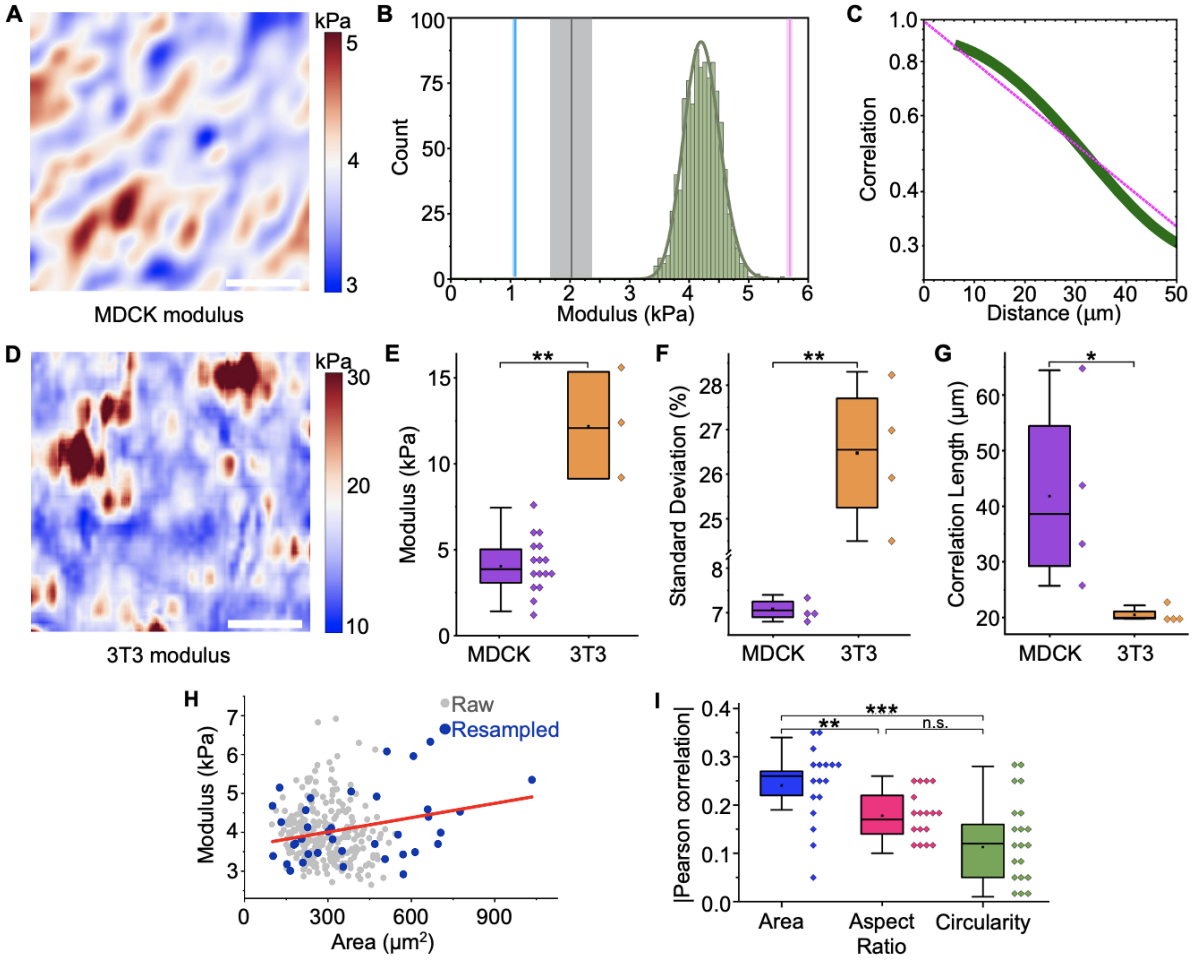

Figure 2.4: Effective modulus fields in MDCK and 3T3 cell monolayers
(A) Effective modulus heatmap of an MDCK monolayer predicted by AI inference. (B) Histogram of (A) showing the AI-predicted MDCK effective modulus in comparison to literature values. The cyan, gray, and pink lines denote the mean moduli reported in (Fujii et al., 2019; Nehls et al., 2019; Pietuch et al., 2015), respectively, with the standard deviation illustrated by the shaded area. (C) Correlation function of the measured MDCK effective modulus field exhibits an exponential decay $\sim e^{-d/45.2}$ (dashed magenta line). (D) Effective modulus heatmap of a 3T3 cell layer predicted by the AI inference. (E) Mean moduli for MDCK and 3T3 cells determined using the force measurement. The 3T3 cells are approximately four times stiffer than MDCK cells. (F) 3T3 cells exhibit a greater effective modulus fluctuation (standard deviation $\sim 27\%$) than that of MDCK cells (standard deviation $\sim 7\%$). (G) MDCK cells exhibited an effective modulus distribution that is more spatially correlated (correlation length $\sim$ 40 m) than that of 3T3 cells (correlation length $\sim$ 20 m). (H) Effective modulus and area measurements for individual cells (n = 286). Blue points denote a resampled dataset (n = 36) that has an even probability distribution across area values. The fit for resampled data (red line) shows a correlation between effective cell modulus and area. (I) Pearson correlation between morphological features and effective modulus values. We observed weak correlation between effective cell modulus, area, and aspect ratio. Scale bar for A and D = 200 μm.

CHAPTER 3

Metabolic Reprogramming during Epithelial Crowding Underlies Jamming Transition

3.1 Overview

Jamming, crucial for maintaining tissue integrity during morphogenesis and wound healing, becomes dysregulated in carcinoma metastasis and asthma. Despite its pathological significance, the molecular mechanisms governing jamming remain poorly understood. In this study, we utilized time-course transcriptome analysis and isotopologue metabolomics to elucidate the metabolic changes associated with jamming. Our findings reveal an energy-independent increase in glucose oxidation, specifically pyruvate anaplerosis, during cell jamming. We further demonstrated that reverting this metabolic shift by inhibiting the mitochondrial pyruvate carrier leads to upregulation of cell motility, effectively abolishing the jamming transition. This metabolically induced tissue fluidization is characterized by uncoordinated cell movements with enriched Rac/RhoA activity, in contrast to the collective migration observed in previous unjamming experiments. Additionally, we show that the preserved E-cadherin junction facilitates motility-driven elongation of cells. The identification of this metabolic regulation of jamming transition holds significant implications for understanding cancer dissemination and embryonic morphogenesis, both of which involve substantial metabolic reprogramming.

3.2 Introduction

Epithelial tissues typically maintain a stable, solid-like structure under healthy physiological conditions, but can exhibit a fluid-like and migratory behavior during developmental processes, tissue remodeling, wound healing, and in cases of malignant invasion or metastasis (Thiery et al., 2009; Friedl and Gilmour, 2009). This transition from solidity to fluidity is governed by a complex interplay of biochemical and physical interactions among cells and their environment. As tissue density increases, cell motility becomes constrained until a critical density is reached, leading to a jamming transition that solidifies the collective. This transition not only ensures proper tissue development, but also acts as a mechanism suppressing tumor growth. Conversely, a reversal of this transition, known as unjamming, facilitates epithelial cell motility and tissue flow. In carcinogenesis, a certain degree of fluidity is necessary for tissue proliferation, migration, and dissemination of cancer cells (Coghlin and Murray, 2010). Cellular unjamming, characterized by cooperative cellular motion akin to fluid flow, represents a key process enabling epithelial cells to acquire migratory behavior. The transition from a static to a migratory state is crucial in various physiological and pathological contexts, such as embryonic development and cancer progression (Guillot and Lecuit, 2013; Friedl and Gilmour, 2009). While experimental observations suggest that this transition resembles the jamming transition seen in particulate matter (Alt et al., 2017), the molecular mechanism driving cellular jamming and unjamming in biological systems remains largely unknown.

Increased motility generally entails higher energy demand, a topic often explored in the context of cell motility and metabolism, primarily through the lens of epithelial to mesenchymal transition (EMT) and cancer biology. The Warburg Effect, seen in cancer cells, highlights their preference for time-effcient aerobic glycolysis over yield-efficient mitochondrial respiration, potentially enhancing invasiveness and motility (Lu, 2019). However, the importance of studying metabolism's role in regulting cell behavior extends beyond cancer. For example, during development neural crest cells undergoing EMT demonstrate a unique metabolic phenotype with increase glycolytic flux (Bhattacharya

et al., 2020). Recent advancements have been able to investigate metabolism in context of wound healing in which they demonstrate that collective cell migration initiated from wound repair induces a glycolytic phenotype in a migrating epithelium (DeCamp et al., 2020). However, how unjamming is influenced by cell metabolism in a physiological setting remains unclear. Our data works towards addressing this knowledge gap by integrating multiomic time course experimetns to identify cell metabolism as a key molecular regulator of the jamming transition in which a shift from glutaminolysis to pyruvate aneplerosis was observed as cells jam, and that mitochondrial pyruvate inhibition promotes fluidization fueled by T1 transitions in a jammed epithelium.

3.3 Materials and Methods

Cell Culture and Drug Treatment

All experiments were conducted using Madin Darby Canine Kidney cells (MDCK) cultured in MEM-α (Fisher Scientific, 12561-056) supplemented with 10% fetal bovine serum (FBS) (Fisher Scientific, 12662-029) and 1% Penicillin-Streptomycin (Fisher Scientific, 15140-122). Cells were maintained at 37 °C and 5% CO_2 with humidity. For all assays, cells were passaged when they reached $\sim$ 80% confluence using Trypsin/EDTA solution (Fisher Scientific, 25300-054). Cells utilized in all experiments were seeded at 30,000 cells/cm^2.

For MPC inhibition, 2 or 5 μ M UK5099 was used (Selleckchem, S5317). These optimal concentrations were determined by titrating doses to achieve their primary functions without causing other adverse effects, such as apoptosis. All pharmacological agents were administered at 37 °C and 5% CO_2 near the onset of confluence, or roughly 64 hours after seeding at 30k cells/cm^2.

RNA extraction

RNA was extracted from cells using the Zymo RNA extraction kit (R2072) following the manufacturer's protocol. Sequencing was performed on one lane of a Novaseq S4

200cycles, for a 44M/sample read depth.

ATAC-seq sample processing

Briefly, the omni-ATAC-seq protocol was utilized fro sample preparation (Corces et al., 2017). The optimized transposition reaction was performed by pelleting 50k cells at 500 RCF at 4°C for 5 minutes before resuspending in a solution of 0.1% NP40 (Thermo Scientific, 28324), 0.1% Tween20 (Thermo Scientific, 28320), and 0.01% digitonin (Promega, G9441). After incubating on ice for 3 minutes the lysis was washed with a buffer containing 0.1% Tween20. Nuclei were then pelleted at 500 RCF for 10 min at 4C followed by supernatent aspiration and resuspended in a transposition mixture containing 100nM transposase, PBS, 1% digitonin, 0.5 μl 10% Tween20, and ultra pure water (Invitrogen, 10977-015). Samples were then incubated at 37C for 30 minutes in a thermomixer with 1000 RPM mixing. Samples were then cleanup use using a Zymo DNA Clean and Concentrator Kit (D4014) following the manufacturer's instructions. Resulting elution was then amplified using a mixture containing 25 μM i5 adaptor, 25 μM i7 adaptor, NEBNext master mix (M0541L), and 20 μl of the sample. Thermocycling settings used were: 72C for 5 min 98C for 30 sec followed by 5 cycles of [98C for 10 sec, 63C for 30 sec, 72C for 1 min] then held at 4C. qPCR was then performed to determine the additional number of cycles required using the amplification plot. A mixture of ultra pure water, PCR primer mix, SYBR Gold (in DMSO) (Invitrogen, S11494), NEBNext master mix, and 5 μl pre-amplified sample were used for qPCR and the cycling conditions utilized were: 98C for 30 sec, followed by 20 cycles of [98C for 10 sec, 63C for 30 sec, 72C for 1 min]. The libraries were then purified using AMPure XP beads (Beckman Coulter, A63881). Libraries were quantified using quibit and tapestation. Sequencing was performed on a Novaseq S4 (2000-2500M/lane).

RNA-seq and ATAC-seq analysis

The RNA-seq and ATAC-Seq reads were preprocessed for the quality control using fastQC (https://www.bioinformatics.babraham.ac.uk/projects/fastqc/) and then trimmed to remove the adapter and low quality sequences using Cutadapt (Martin, 2011) before they were used for alignment. The ultrafast universal RNA-seq aligner, STAR program (version 2.7.10a) (Dobin et al.) was employed to align the RNA-seq reads to the dog genome canFam4 and RefSeq All (ncbiRefSeq) genes obtained from the USCS genome site (https://genome.ucsc.edu). The read counts of the genes from the STAR output were subsequently normalized and analyzed for differential comparison using R limma package (Ritchie et al., 2015). The ATAC-Seq reads were mapped to the canFam4 genome using bowtie2 (Langmead and Salzberg). The non-unique mapped and duplicate reads were subsequently removed from the alignments using Picard tools (http://broadinstitute.github.io/picard/). MACS2 (Zhang et al., 2008) was used to identify peaks in each sample. The R package DiffBind (Ramírez et al., 2016) was then implemented to compute read counts and generate the consensus peaks present in more than 3 out of 45 samples. The genomic features associated with the peaks were then annotated using the annotatePeaks function from Homer package (http://homer.ucsd.edu/homer/ngs/peaks.html). For the creation of heatmap plots, the count matrix within the 5k bp upstream and downstream of the peak regions was calculated using computeMatrix function of deepTools (Stark et al., 2011).

Immunostaining

Cells plated in a 4-chamber Ibidi slide (Ibidi, 80426) were fixed in 10% neutral buffered formalin with 0.03% Eosin (Sigma-Aldrich, F5304-4L) for 10 minutes at room temperature. Permeabilization and blocking were performed with 2% Donkey Serum (Fisher Scientific, D9663-10ML) and 0.25% Triton X-100 in PBS with calcium and magnesium (Fisher Scientific, 14040-133) for 30 minutes. After three washes with PBS, cells were incubated with primary antibodies: E-cadherin, YAP, RhoA, Rac, or ECCD2 (abcam, ab11512;

Novus Biologicals, NB110-58358; Cell Signaling Technology, 2117T; Invitrogen, PA1-091 or Invitrogen, 13-1900, respectively) for 30 minutes. Subsequently, cells were washed thrice with PBS and incubated with secondary antibodies (anti-mouse Alexa Fluor 488 or anti-rabbit Alexa Fluor 647) (Invitrogen, A21042 and 4414S, respectively), along with DAPI (abcam, ab228549) and either phalloidin (Invitrogen, A12379) or actin (Invitrogen, R37110), for 30 minutes at room temperature.

Imaging and Analysis

Fluorescent images were acquired using either a confocal microscope (RCM1 with Nikon Eclipse Ti-E, NIS-Elements software, or NL5+ with Nikon Ni-E, Micromanager software) or a widefield fluorescent microscope (Etaluma LS720 Lumaview 720/600-Series software, or ECHO (76490-288). A 20× WI/0.95 NA, 20×/0.75 NA, or 40× oil/1.30 NA objective was used for images taken using confocal microscopy. A 20×/0.40 NA objective was used for the widefield fluorescent images with the Etaluma microscope and 20×/0.75 NA objective for the ECHO microscope. The imaging conditions were consistently maintained across all experiments. To quantify fluorescent intensity, z-projected images obtained from z-stack imaging using a step size of $\sim$2 μm were used. In time lapse imaging, images were taken using the Etaluma microscope every 15 minutes with media changes performed every two days. Morphological segmentation was performed using Cellpose (Stringer et al., 2021). Quantifications were performed using MATLAB (version R2023a) or ImageJ (version 2.1.0/1.53c).

Glucose and glutamine tracing

MDCK cells were seeded at 30k cells/cm^2 in a 6-well plate such that all cells for every time point were harvested at the same time. UK5099 samples were treated with 2μM UK5099 for 80 hours. Cells were cultured for 24 hours in glucose free DMEM medium (Gibco, 11966-025) or glutamine free DMEM medium (cat) supplemented with [U-13C]glucose (Cambridge Isotope Laboratories, CLM-1396-PK) or [U-13C]glutamine, respectively. Be-

fore metabolite extraction, the [U-13C]glucose or [U13C]glutamine medium was aspirated and cells were washed with cold 150 mM ammonium acetate at a pH of 7.3. 500 μL of cold 80 % methanol was then added to each well and cell detachemnt was facilitated using a cell scraper. 10 μl of 1mM norvaline (Sigma) was added to the resulting suspension as an internal standard. Each sample was briefly vortexed before being centrifuged at 17,000g for 5 min at 1 °C. 400 μL of the resulting supernatant was then transferred to an ABC vial (Fisher Scientific) and evaporated (EZ-2Elite evaporator, Genevac).

Dried metabolites were resuspended in 300 μL 50% ACN: water and centrifuged for 15 min at 4°C. 5 μL of the clarified extract was loaded onto a Luna 3um NH2 100A (150 $\times$ 2.0 mm) column (Phenomenex). The chromatographic separation was performed on a Vanquish Flex (Thermo Scientific) with mobile phases A (5 mM NH4AcO pH 9.9) and B (ACN) and a flow rate of 200 μL/min. A linear gradient from 15% A to 95% A over 18 min was followed by 7 min isocratic flow at 95% A and reequilibration to 15% A. Metabolites were detected with a Thermo Scientific Q Exactive mass spectrometer run with polarity switching in full scan mode with a range of 70-975 m/z and 70.000 resolution. Maven (v 8.1.27.11) was utilized to quantify the targeted metabolites by AreaTop using accurate mass measurements (¡ 5 ppm) and expected retention time previously verified with standards.

Values were normalized to cell number or protein content of extracted material. Normalization was performed by trypsinizing a sacrificial well at each time point and performing a cell count with the suspension. For the cell count, an automated cell counter (Countess II) and trypan blue was used and the average of two measurements was utilized as the cell count. Relative amounts of metabolites were calculated by summing up the intensity values for all detected isotopologues of a given metabolite. C13 natural abundance corrections were made using AccuCor. Data analysis was performed using in-house R scripts.

Seahorse assay

Oxygen consumption rate (OCR) and the extracellular acidification rate (ECAR) were measured in a Seahorse XFe24 Extracellular Flux Analyzer (Agilent Technologies). A total of 57,000 cells/well were seeded on a Seahorse XF24 plates. On the day of the assay, cells were washed with assay medium (unbuffered DMEM assay medium supplemented with 8 mM glucose, 2 mM glutamine, 1 mM sodium pyruvate, and 5 mM HEPES; pH 7.4). Compounds were injected sequentially during the assay resulting in final concentrations of 2 μM oligomycin (Port A), 0.75 μM FCCP (Port B), 1.35 μM FCCP (Port C), and 1 μM rotenone and 2 μM antimycin (Port D). OCR and ECAR were measured in parallel. Rate measurements were normalized to the number of nuclei stained with 10 μg/mL Hoechst dye counted on an Operetta High-Content Imaging System (PerkinElmer). ATP production rates were calculated as described by Desousa et al. (Desousa et al., 2023). Data was analyzed according to Divakaruni et al. (Divakaruni et al., 2014).

Data analysis and Statistics

GraphPad PRISM (version 10) and MATLAB (version R2023a) were used to perform statistical analysis and create figures. Data is presented as mean ± standard deviation. For correlative analyses, both the Pearson correlation coefficient and the Spearman correlation coefficient were calculated in addition to the p-value, false discovery rate (FDR), and confidence interval (CI), all of which are summarized in tables 6.1-6.3. False discovery rate (FDR) was evaluated using a Monte Carlo simulation that randomly permutes the X Y values of data points. P-values > 0.05 are denoted as not significant (ns), while p-values ≤ 0.05, ≤ 0.01, ≤ 0.001, and ≤ 0.0001, are represented as *, **, ***, and ****, respectively.

3.4 Results

Multi-omic characterization revealed dynamic changes in cell morphology, gene expression, and epigenetic landscape, during the cell crowding

To understand the molecular regulation of cell motility during the epithelial jamming transition, we began by conducting a multi-omic time course experiment using Madin-Darby canine kidney (MDCK) cells in which we performed morphological, RNA-sequencing, and ATAC-sequencing analysis at 15 time points throughout crowding (Fig. 3.1A). The 15 time point data acquisition began 24 hours after seeding to avoid any potential artifacts due to cell settling, and ended 144 hours after seeding at 30k cells/cm^2 to capture the fully jammed state. The intermediate timepoints were selected to capture critical changes in cell behavior resulting from crowding at a fine temporal resolution.

A well-known hallmark of a jammed system is the decline of cell motility (Park et al., 2015). We therefore performed a motility analysis using MDCK cells for approximately six days, beginning from when cells were in small colonies to several days after reaching confluence (Fig. 3.1B). We confirmed that the root mean squared (RMS) velocity was high, $\sim 75\mu$m/hr, when the cells were subconfluent, but quickly decayed after the cells reached confluence. Furthermore, we also observed that the cells reached a kinetic steady state after $\sim$ 120 hours post-seeding, validating that our timepoint selection encompassed immotile, jammed cells.

In addition to cell motility, we also characterized two additional hallmarks of crowding: E-cadherin (E-cad) junction formation and YAP-inactivation (Figs. 3.1C-3.1F). Specifically, we performed immunofluorescent imaging of MDCK cells probed for E-cad (Fig. 3.1C) and quantified its localization at the cell-cell junction (Fig. 3.1D). We also investigated YAP translocation using immunofluorescent imaging (Fig. 3.1E) by quantifying the ratio between YAP in the cytoplasm and nucleus (Fig. 3.1F). This ratio is often used as a metric to characterize YAP activity, as inactive and active YAP corresponds to YAP sequestered in the cytoplasm and nucleus, respectively. We found that the E-cad

localization and YAP translocation occurred roughly around the same timepoint when cells reached confluence. Together, the maturation of E-cad and the inactivation of YAP both further validate our timepoint selection to capture key molecular events associated with crowding.

After validating our experimental model, we used our morphology, gene expression, and chromatin accessibility data from 15 timepoints to understand the evolution of these cell properties in response to crowding (Figs. 3.1G-3.1I). Using principal component analysis (PCA) we found that all three properties displayed similar non-monotonic trajectories. Specifically, we found the time evolutions to be non-linear with the turning point occurring roughly at the same time, temporally coinciding with onset of confluence in our system. We then used our RNA-sequencing data to unbiasedly screen transcriptional signatures that may underlie cell jamming by performing gene set enrichment analysis (GSEA) on the first and last time points in our sample collection (Fig. 3.1J). Interestingly, we observed consistent transcriptional signatures between early and late crowding (Figs. 3.1K-3.1L) in which early crowding analyzes the first and fifth time point and late crowding analyzes the fifth and last time point. The fifth timepoint was chosen as the division point since it roughly coincides with the turning point of the three PCA trajectories. These similar enrichment profiles suggest that transcriptional changes being early the crowding process and are not fully governed by canonical biochemical activities, such as YAP inactivation or E-cad maturation as these events do not begin to occur until approximately when cells reach confluence. Our GSEA results revealed that in addition to the enrichment of several anticipated pathways associated with cell motion, epithelial phenotype, and cell cycle, there was also significant enrichment of metabolic pathways including glycolysis, oxidative phosphorylation (oxphos), and fatty acid metabolism. Intrigued by this finding, we plotted a heatmap of the key genes comprising the glycolysis, oxphos, and fatty acid metabolism pathways and found that they were roughly linearly differential over time (Fig. 3.1M).

Focusing on related metabolic enzymes associated with this GSEA result, we then integrated our RNA-seq data with our ATAC-seq data to understand the role epigenetics

played in regulating the metabolic activity of MDCK cells during crowding. In this analysis, we only considered promoters from the ATAC-seq data since this refers to a region of DNA where transcription initiation occurs and thus plays a strong role in regulating gene expression. As demonstrated in Fig. 3.1N, most of these metabolic enzymes exhibit consistent differential expression between transcript levels and chromatin accessibility, suggesting that the metabolic changes we observe during crowding may be driven by epigenetic modifications. We then calculated the Pearson correlation between the RNA expression and ATAC peak values using the 15 time points for the previously identified metabolic enzyme encoding genes (Fig. 3.1O). In doing so, we discovered that most of the 31 genes showed a positive correlation, while 16 of these genes exhibited a moderate to strong correlation, with a Pearson correlation coefficient greater than or equal to 0.5. Collectively, by integrating our multi-omic analyses, we showed that there are dynamic changes in cell morphology, gene expression, and epigenetic landscape beginning early in the cell crowding, and that cell metabolism may play a role in governing the cell behavior during crowding via epigenetic modifications.

Pyruvate aneplerosis increased while glutaminolysis reduced during cell jamming

After identifying cell metabolism to play a role in coordinating epithelial jamming, we established an approach to perform metabolic characterization of MDCK cells at three critical timepoints during crowding using metabolic profiling and nutrient tracing. Specifically, we focused on cells at the 48, 64, and 144 hour time point as they respectively correspond to subconfluent, confluent, and fully jammed cells, which also align with the timepoints used to define the two phases of jamming previously described. We first began by performing [U-13C]glucose tracing, which uses an isotope of glucose comprised of six carbons labeled with an extra neutron to monitor how glucose is utilized by tracking the fate of these labeled carbons through metabolic pathways. In this experiment, we mainly focused on studying glucose oxidation (Fig. 3.2A), which is the metabolic process by which glucose is broken down in cells to produce energy in the form of adenosine triphosphate

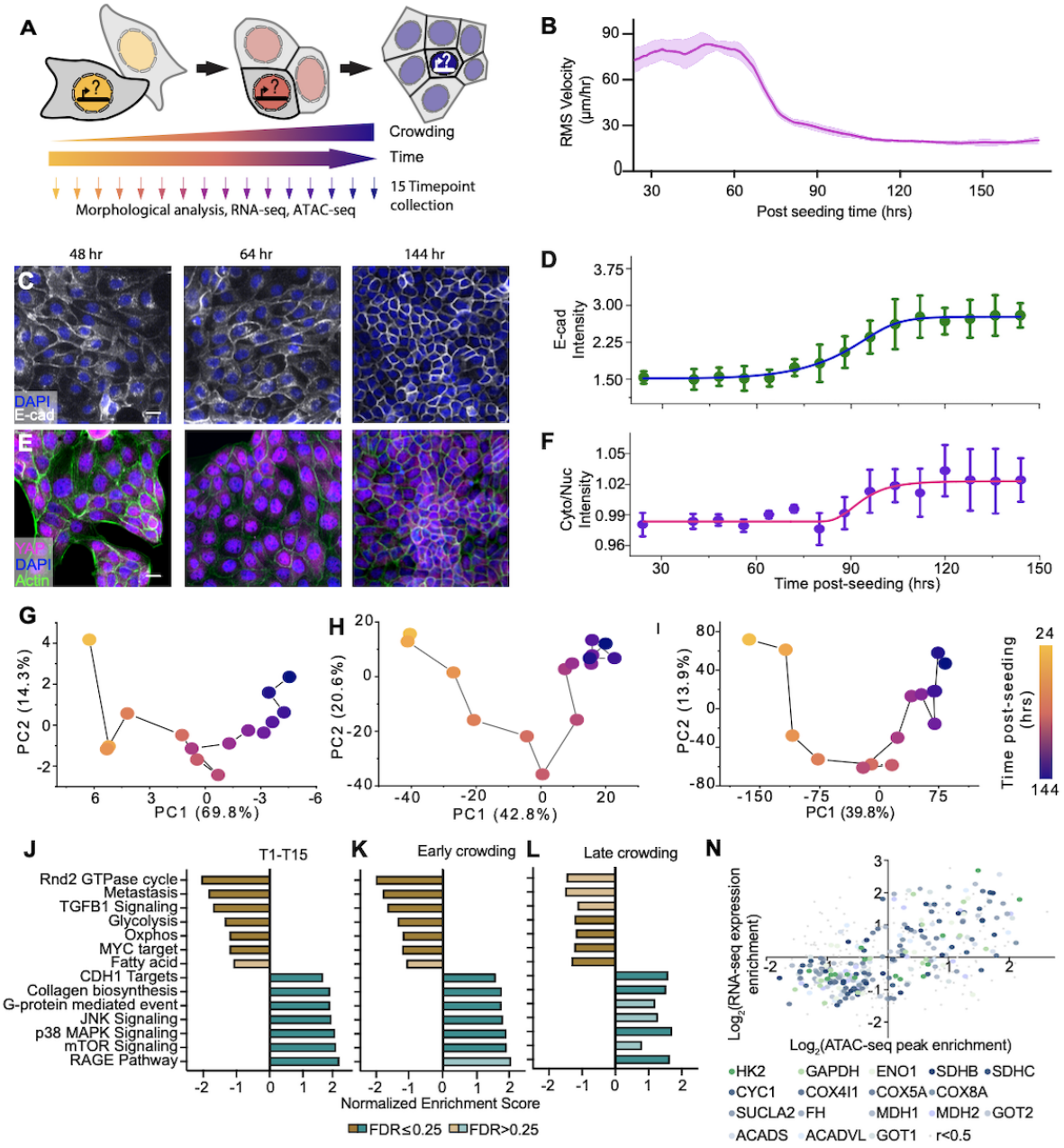

Caption on next page.

Figure 3.1: Multi-omic characterization revealed dynamic changes in cell morphology, gene expression, and epigenetic landscape, during the cell crowding.

(A) Experiment overview. MDCK cells were seeded at 30,000 cells/cm^2 until fully jammed (144 hours). The cell morphology, gene expression, and chromatin accessibility were analyzed at 15 timepoints throughout the crowding process using quantitative microscopy, RNA-sequencing, and ATAC-sequencing, respectively. (B) Cell motility decreases and reaches a steady state root mean squared (RMS) velocity in response to jamming. Solid line denotes the mean while the shaded band denotes standard deviation. (C) Immunofluorescent images of MDCK cells probed for E-cadherin (E-cad) at three representative timepoints. Scale bar = 20 μm. (D) E-cad quantification demonstrating that E-cad intensity and localization to the junction increases as cells undergo crowding. (E) Immunofluorescent images of MDCK cells probed for YAP at three representative timepoints. Scale bar = 20 μm. (F) YAP quantification demonstrating YAP translation from the nucleus to cytoplasm, suggestive of YAP inactivation in response to crowding. Principal component analysis of (G) morphology (H) gene expression and (I) chromatin accessibility throughout crowding. Each data point represents the average of three replicates for each timepoint. Gene set enrichment analysis (GSEA) using RNA-sequencing results for pairwise comparisons of (J) the first and last timepoints (K) the first and 5th timepoint, and (L) the 5th and last timepoint. The 5th timepoint was identified as a point of interest since it roughly coincides with the turning point of the trajectories shown in (G-I). (M) Heatmaps of the metabolic pathways glycolysis (left), oxidative phosphorylation (oxphos) (middle), and fatty acid (right) metabolism identified by GSEA. (N) Scatter plot of $\log_2$ RNA-seq expression enrichment versus $\log_2$ ATAC-seq peak enrichment for metabolic enzymes. Only promoters were considered in the ATAC-seq peak enrichment analysis. (O) Bar chart of the Pearson correlation coefficients between the RNA expression and ATAC peak values for metabolic enzymes.

(ATP). Using our [U-13C]glucose tracing data, we first performed a PCA using the fractional contribution of all detected metabolites. Here, the factional contribution refers to the proportion or percentage of a specific metabolic pathway or process that is fueled by the labeled glucose compared to other sources, revealing how much of a particular nutrient is being utilized in a given metabolic pathway. This analysis indicated that the metabolic phenotypes of the cells are distinct, illustrated by the tight clustering of the replicates for each condition, and that the metabolic phenotype evolves over time (Fig. 3.2B). We then assessed TCA cycle activity by plotting a heatmap of the fractional contribution of key TCA cycle intermediates (Fig. 3.2C). The collective upregulation of these metabolites suggests that TCA cycle activity has more of a demand as cells jam, and that pyruvate aneplerosis is increased. We also plotted bar charts of these intermediates to confirm the

statistical significance of these results, in which nearly all metabolite displayed significant fractional contribution differences between the first and last timepoint (Fig. 3.2D).

Next, we similarly performed [U-13C]glutamine tracing at the same timepoints. Here, we focused on glutamine oxidation (Fig. 3.2E), which is the metabolic process by which glutamine is broken down and utilized for energy production. Glutamine serves as a crucial substrate for replenishing TCA cycle intermediates and fueling cellular metabolism. Parallel to our glucose tracing analysis, we began by performing an unbiased PCA encompassing the fractional contribution of all detected metabolites, which similarly revealed distinct metabolic phenotypes for each timepoint that continuously evolved throughout jamming (Fig. 3.2F). Using the same TCA cycle metabolites as the glucose tracing analysis, we plotted a heatmap of their corresponding fraction contribution and discovered that glutamine oxidation, specifically glutaminolysis, was decreased in response to jamming (Fig. 3.2G). This result was validated by plotting the bar charts of the corresponding metabolites, as it revealed a statistically significant decrease in glutamine labeled metabolite fractional contribution over time (Fig. 3.2H). Together, these results demonstrate that pyruvate aneplerosis and glutaminolysis are upregulated and downregulated, respectively, during jamming.

After characterizing how glucose and glutamine are utilized during crowding, we sought to examine how these findings translate the ATP production. To do so, we performed a Seahorse assay investigating the oxygen consumption rate (OCR) and extracellular acidification rate (ECAR) for cells at the same three timepoints during jamming. This assay allows us to analyze how cells utilize oxygen and glucose during the different phases of crowding and thus further characterize their metabolic phenotypes. Here, OCR reflects mitochondrial respiration and ATP production through oxidative metabolism, or oxphos, while ECAR reflects glycolytic activity and the production of lactate under anaerobic or aerobic conditions (Fig. 3.2I). We began by studying the basal OCR (Fig. 3.2J) and basal ECAR (Fig. 3.2K) and discovered that jammed cells have a lower basal OCR and basal ECAR compared to subconfluent cells. This result demonstrates that there is a reduction of cellular respiration and glycolysis, which can be due to either a shift in metabolism

or reduced energy demand. To get a better understanding of what is generating such reductions, we plotted the basal OCR/ECAR (Fig. 3.2L) and the oxphos/glycolysis ATP production rate (Fig. 3.2M). This analysis unveiled that the oxphos/glycolysis activity was both relatively high and constant between the 48 and 144 hour timepoints, implying that there is no obvious metabolic shift between glycolysis and oxphos, but that ATP is mainly produced through oxphos.

Collectively, these results demonstrate that while the utilization of oxphos and glycolysis remains unchanged during crowding, ATP is always mainly produced through oxphos. Integrating this with the nutrient tracing results, we found that glucose oxidation is relatively independent of energy production and that glucose oxidation may play a functional role in regulating jamming. We concluded that ATP is mainly generated through oxphos, in which glutamine oxidation is a main pathway of oxphos. We also discovered that an increase of glucose oxidation does not change ATP generation, as they serve different functional roles.

Inhibition of the mitochondrial pyruvate inhibitor induced uncoordinated cell movements and reverted jamming transition

In light of these findings highlighting the altered ATP source and the distinct functional roles of glucose oxidation and glutamine oxidation in ATP generation, we next explored how UK5099, a mitochondrial pyruvate carrier (MPC) inhibitor, modulates cellular phenotypes. To do so, we first began by performing [U-13C] glucose tracing on untreated jammed and UK5099 treated cells (Fig. 3.3A). Specifically, we seeded both the control and UK5099 samples at 30k cells/cm ^{2}. At the 64 hour time point, roughly when cells reach confluence, we administered 2 μM UK5099 to the UK5099 sample only. The media was then supplemented for labeled glucose for the last 24 hours of the experiment to allow a metabolic steady state to be achieved. We began by validating that the UK5099 was on target, in which we found that the fractional contribution of key TCA cycle metabolites expected to be down-regulated upon MPC inhibition were reduced in the UK5099 sample

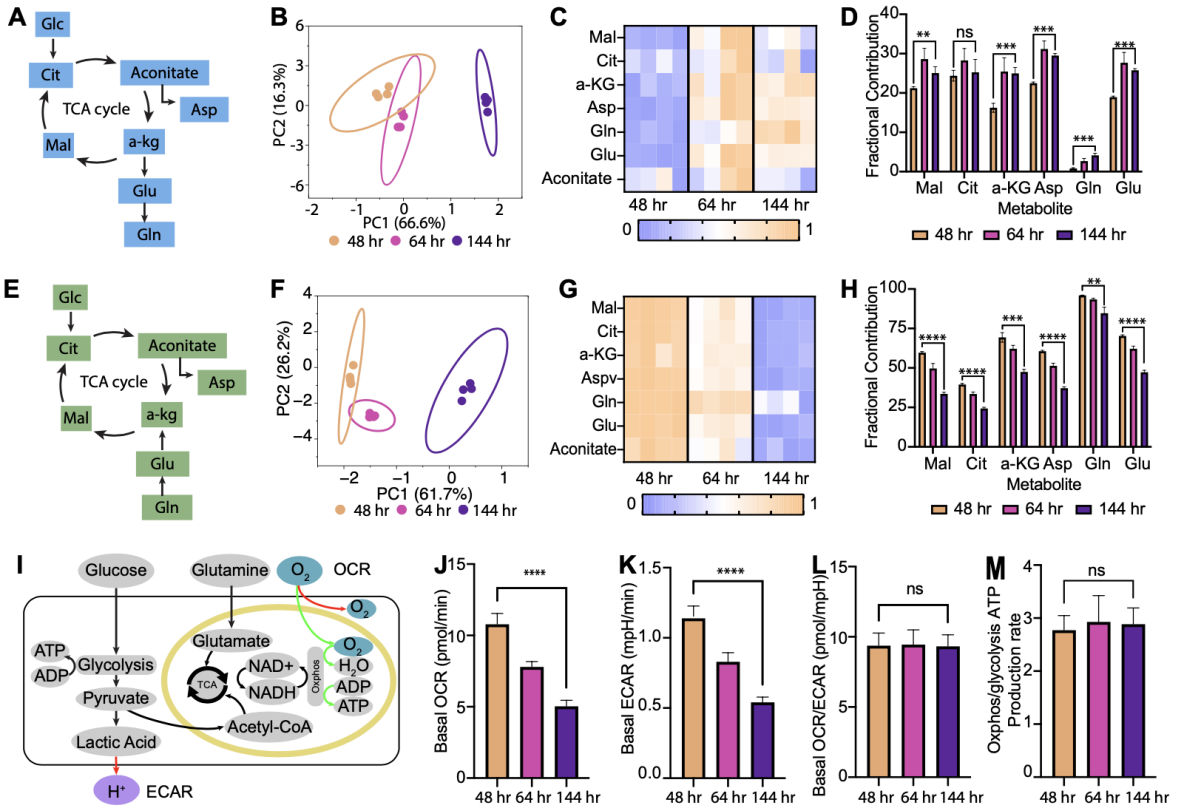

Figure 3.2: Glucose oxidation increased while glutamine oxidation reduced during cell crowding.

(A) Schematic of the glucose oxidation pathway, illustrating the [U-13C] glucose tracing pathway. (B) Principal component analysis (PCA) of fractional contribution from [U-13C]glucose metabolic tracing data. Ellipses represent the 95% confident ellipse for each condition. (C) Normalized heatmap of the fractional contribution of TCA-cycle intermediate metabolites from [U-13C] glucose tracing throughout crowding. Each column represents a replicate. (D) Fractional contribution from [U-13C] glucose to TCA cycle intermediate metabolites throughout crowding with four replicates per timepoint. (E) Schematic of the glutamine oxidation pathway, illustrating the [U-13C] glutamine tracing pathway. (F) Principal component analysis (PCA) of fractional contribution from [U-13C] glutamine metabolic tracing data. Ellipses represent the 95% confident ellipse for each condition. (G) Normalized heatmap of the fractional contribution of TCA-cycle intermediate metabolites from [U-13C] glutamine tracing throughout crowding. Each column represents a replicate. (H) Fractional contribution from [U-13C] glutamine to TCA cycle intermediate metabolites throughout crowding with four replicates per timepoint. (I) Schematic illustrating mitochondrial respiration and glycolysis to obtain oxygen consumption rate (OCR) and extracellular acidification rate (ECAR) measurements. (J) Basal OCR of MDCK cells throughout crowding. (K) Basal ECAR of MDCK cells throughout crowding. (L) Basal OCR/ECAR of MDCK cells throughout crowding. (M) Oxidative phosphorylation (Oxphos)/glycolysis ATP production rate of MDCK cells throughout crowding. "ns", **, ***, ****, refer to p-values ≥ 0.05, < 0.01, < 0.001, and < 0.0001, respectively.

relative to the control (Fig. 3.3B). Similar to the Seahorse assay performed using the three different time points previously discussed, we next performed the same assay on control and UK5099 treated cells. We found that the basal OCR and basal ECAR remained unchanged in response to UK5099 treatment. Together, these results demonstrate that UK5099 reduces glucose oxidation without perturbing energy production. It is well known metabolic activity is closely linked to cell cycle activity due to the high energy demand of cell division (Antico Arciuch et al., 2012). To rule out the possibility of any phenotypic changes observed being due to an artifact of differences in cell cycle or density, we confirmed that there were no differences in cell number between the two samples (Fig. 3.3E) or mean cell area due to UK5099 treatment. We also confirmed that UK5099 treatment did not alter the cell cycle by performing EdU staining (Fig. 6.13).

After validating that UK5099 does not perturb cell cycle or cell density, we next sough to understand how this metabolic perturbation impacts cell jamming. By performing time-lapse imaging, we discovered that UK5099 treatment results in increased cell movement (Fig. 3.3F), after about roughly three days of UK5099 treatment. The root mean squared (RMS) velocity in both samples were relatively high around the time cells have just reached confluence as there is little to no geometric constraint imparted on cells, and begins to decrease as the geometric constraint increases to induce cells jamming. However, the RMS velocity trajectories interestingly begin to bifurcate after this point in which the UK5099 treated sample's velocity increases by nearly 1.5 fold (Fig. 3.3G). This time-delay is in accordance with previous studies that report that UK5099 treatment may require a few days to take full effect on cells (Yang et al., 2014). Finally, we confirm that there are initially no significant differences in the RMS velocities between control and UK5099 treated cells, but that the velocity begins to significantly diverge after treatment (Fig. 3.3H).

Motivated by this discovery, we sought to further characterize the phenotype of these fluidized cells. There are two main type of motion in epithelial monolayers. The first type corresponds to collective cell migration in which a group of cells coordinate to travel together in the same direction, and the second type corresponds to uncoordinated cell

motion, in which T1 and T2 transitions are responsible for tissue remodeling. To gain an understanding of the type of motion being induced by UK5099, we analyzed the velocity field to first understand the direction of cell motion in context of the collective (Fig. 3.3I). This analysis revealed that the motion was relatively uncoordinated, as there was no observation of a large group of cells with velocity fields pointing in the same direction. To quantify this observation, we analyzed the velocity-velocity autocorrelation function, which reveals how correlated one cell's velocity is with its neighbor's velocity at a given time (Fig. 3.3J) in which similar correlation functions were observed. We then extracted the correlation length from this analysis (Fig 3K) to furher classify the mode of fluidization. The results indicated that although the UK5099 sample had a slightly higher correlation length, the mean correlation of both conditions spanned a length roughly consistent with the diameter of two jammed MDCK cells, representative of uncoordinated cell motion.

This relatively short ranged velocity-velocity correlation length implies that the increased cell motion is more likely resulting from neighbor swapping rather than collective cell migration. To evaluate this possibility, we analyzed the strain rates of the cells. We began by investigating the isotropic strain rate, which can report compression or extension. Physically, isotropic strain occurs when a cell experiences the same amount of deformation in all directions, similar to the strain profile anticipated to be induced by a T2 transition. We found that the UK5099 sample expressed a substantially higher strain rate magnitude compared to control cells (Fig. 3.3L). Although it is possible cell division events can similar isotropic strain rate profiles, this is unlikely to be the reason for observation since our EdU staining revealed that there contributions from cell division are negligible in a jammed UK5099 treated monolayer (Fig. 6.13). Since the isotropic strain rate encompasses both compression and extension, we quantified our observations by plotting the standard deviation of the isotropic strain rate, which was significantly higher in UK5099 treated cells (Fig. 3.3M).

To assess the contribution of T1 transitions in our observed fluidization, we next investigated the deviatoric strain rate. In doing so, we observed a higher deviatoric strain

rate in UK5099 treated cells (Fig. 3.3N). Here, deviatoric strain rate characterizes the rate of change of deformation that results in shear or shape changes within the monolayer, assuming incompressibility. We therefore considered deviatoric strain rate to represent T1 transitions, implying that UK5099 treated cells have more T1 transitions. To quantify our observations, we evaluated the mean shear strain rate of both conditions and found that the UK5099 treated cells exhibited a significantly higher mean shear strain rate (Fig. 3.3O).

With these experiments we have demonstrated for the first time that MPC inhibition alters cell metabolic phenotype to induce tissue fluidization in MDCK cells, suggesting that cell metabolism could be a potential molecular mechanism dictating tissue unjamming. This metabolically induced fluidization is characterized by increased cell velocity resulting from T1 and/or T2 transitions.

UK5099-induced motility is driven by Rac/RhoA activity

How does UK5099 upregulate cell motion? We hypothesized that the RhoA/Rac pathway could be a key signaling pathway involved in regulating the metabolically induce motility we observed due to UK5099 treatment. RhoA and Rac are small GTPases associated with cell migration in which RhoA stimulates the assembly of actin stress fibers and focal adhesions, while Rac activation leads to the polymerization of actin filaments at the cell periphery, facilitating cell movement (Ridley, 2001). To test this, we performed immunofluorescent imaging of control and UK5099 treated cells stained with RhoA (Fig. 3.4A) and Rac (Fig. 3.4B). Quantitative analysis revealed that UK5099 treated cells displayed increased levels of both RhoA and Rac (Figs. 3.4C and 3.4D, respectively), suggesting that this could be the pathway cells utilize during metabolically induced motility, although further analysis of GTPase activity and other experiments such as traction force microscopy would be required to rule out other possibilities.

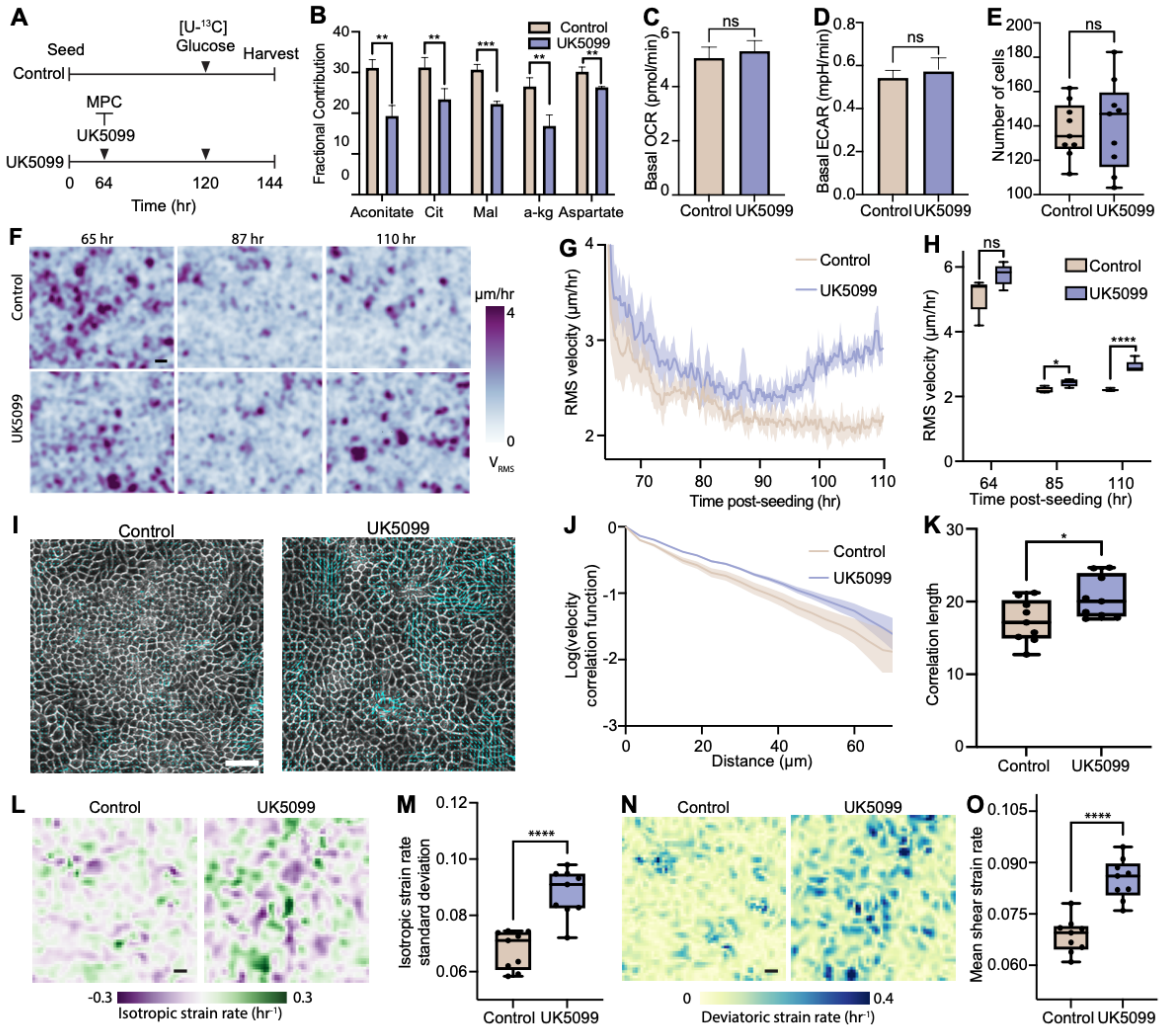

Caption on next page.

Metabolically unjammed cells preserved intercellular junctions while exhibiting a motility-driven elongation morphology

Previous literature has suggested that there are two main modes of epithelial fluidization: the unjamming transition (UJT) and partial epithelial to mesemchymal transition (pEMT) (Mitchel et al., 2020). One main feature distinguishing the two is the presence of E-cad, in which E-cad is maintained during the UJT, but becomes downregulated during pEMT (Mitchel et al., 2020). To further characterize the type of fluidization we observed, we stained cells for both E-cad (Fig. 3.5A) and ECCD2 (Fig. 3.5B), in which the latter

Figure 3.3: Inhibition of glucose oxidation induced uncoordinated cell movements and reverted jamming transition.

(A) Schematic illustrating experiment overview. Cells for both the control and UK5099 sample were seeded at 30k cells/cm^2 and tracer media containing [U-^{13}C]Glucose was exchanged for unlabeled media 120 hours after seeding to allow for a 24 hour incubation time. The UK5099 sample was treated with 2 μM UK5099 64 hours after seeding while the control remained untreated. (B) Reduction in the fractional contribution of key TCA cycle metabolites demonstrated the UK5099 treatment is on target. (C) Basal oxygen consumption rate (OCR) remains unchanged in response to UK5099 treatment. (D) Basal extracellular acidification rate (ECAR) remains unchanged in response to UK5099 treatment. (E) UK5099 treatment does not impact cell density. (F) Velocity heatmap of control (top) and UK5099 (bottom) treated cells at three time points illustrates that MPC inhibition increases cell motility in MDCK cells. Scale bar = 20 μm. (G) Root mean squared (RMS) velocity versus time for control and UK5099 treated cells. Line represents the mean RMS velocity while the shaded band denotes its standard deviation. (H) Box and whisker plot comparing control and UK5099 sample RMS velocities at 65, 85, and 110 hours throughout crowding. (I) Velocity field (cyan arrows) overlaid on phase contrast images of control and UK5099 treated cells. Scale bar = 50 μm. (J) The log of the velocity-velocity auto-correlation function versus time for control and UK5099 treated cells. Line represents the mean correlation function while the shaded band denotes its standard deviation.(K) Cell velocity correlation length box and whisker plot for control and UK5099 treated cells. (L) Isotropic strain rate heatmaps for control and UK5099 treated cells. Scale bar = 50 μm. (M) Box and whisker plot of the standard deviation of the isotropic strain rate for control and UK5099 treated cells. (N) Deviatoric strain rate heatmaps for control and UK5099 treated cells. Scale bar = 50 μm. (O) Box and whisker plot of the mean of the deviatoric strain rate for control and UK5099 treated cells. "ns", *, **, ***, ****, refer to p-values ≥ 0.05, < 0.05, < 0.01, < 0.001, and < 0.0001, respectively.

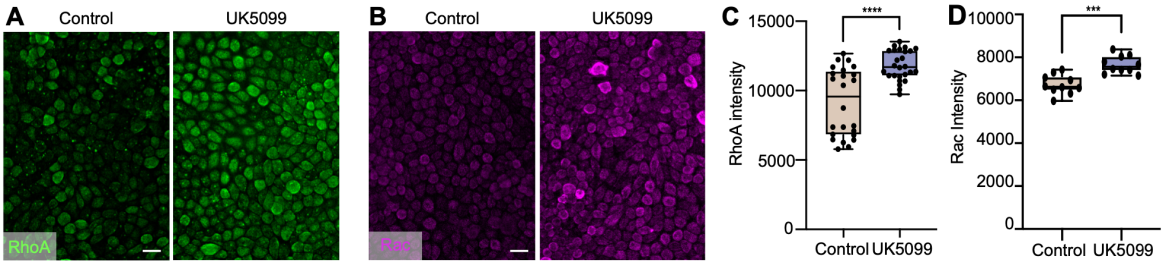

Figure 3.4: UK5099-induced motility is driven by Rac/RhoA activity.
(A) Immunofluorescent images of jammed MDCK cells probed for RhoA in control (left) and UK5099 treated cells (right). (B) Immunofluorescent images of jammed MDCK cells probed for Rac in control (left) and UK5099 treated cells (right). (C) RhoA intensity quantification and (D) Rac intensity quantification demonstrate upregulation of the respective protein in UK5099 treated cells. ***, ****, refer to p-values < 0.001 and < 0.0001, respectively.

recognizes homophillically bound E-cad. Using the E-cad images, we quantified the E-cad intensity localized to the cell-cell junction (Fig. 3.5C), and the thickness of such junctions (Fig. 3.5D). In both analyses, we observed no differences in either parameter, suggesting that E-cadherin is maintained in UK5099 treated cells. Intrigued by this result, we wanted to ensure that the E-cad we observed was in its functional form, so we repeated the intensity analysis using ECCD2 staining. ECCD2 only recognizes the extracellular domain of E-cad under homophilic interactions, and thus reports "functional" E-cad (Chen and Chen, 2009). In doing so, we still observed no differences in ECCD2 intensity (Fig. 3.5E), demonstrating that UK5099 cells still retain functional E-cad at levels similar to untreated cells.

In addition to differences in E-cad, it has been demonstrated that the UJT and pEMT produce their own morphological signatures related to cell shape (Mitchel et al., 2020). We therefore next assessed the cell morphology resulting from UK5099 treatment. To do so, we stained control and UK5099 treated cells with phalloidin to visualize the cell contour (Fig. 3.5F). Using these images, we performed segmentation (Stringer et al., 2021) to obtain the cell aspect ratio (Fig. 3.5G) and shape index (Fig. 3.5H), in which the shape index is a dimensionless structural order parameter defined by $P/\sqrt{A}$ where P is perimeter and A is area (Park et al., 2015). In this analysis, we observed an increase in cell aspect ratio accompanied by no changes in shape index. It is also well known that cells often adapt a more elongated morphology to promote motility (Mendez et al., 2010). In vertex model simulations, it has been demonstrated that by including a "propulsion" parameter without altering cortical tension or junctional tension, the cell aspect ratio could be perturbed without altering shape index (Mitchel et al., 2020). This finding coupled with our results, suggests that our observed cell elongation due to UK5099 treatment may be due to cell propulsion during fluidization.

To categorize fluidization mode, previous studies assess the linear relationship between aspect ratio and shape index (Mitchel et al., 2020). Doing so enables the separates UJT phenotype from pEMT phenotypes since UJT cells exhibit more aspect ratio perturbation compared the shape index, and vice versa. We thus investigated the relationship between

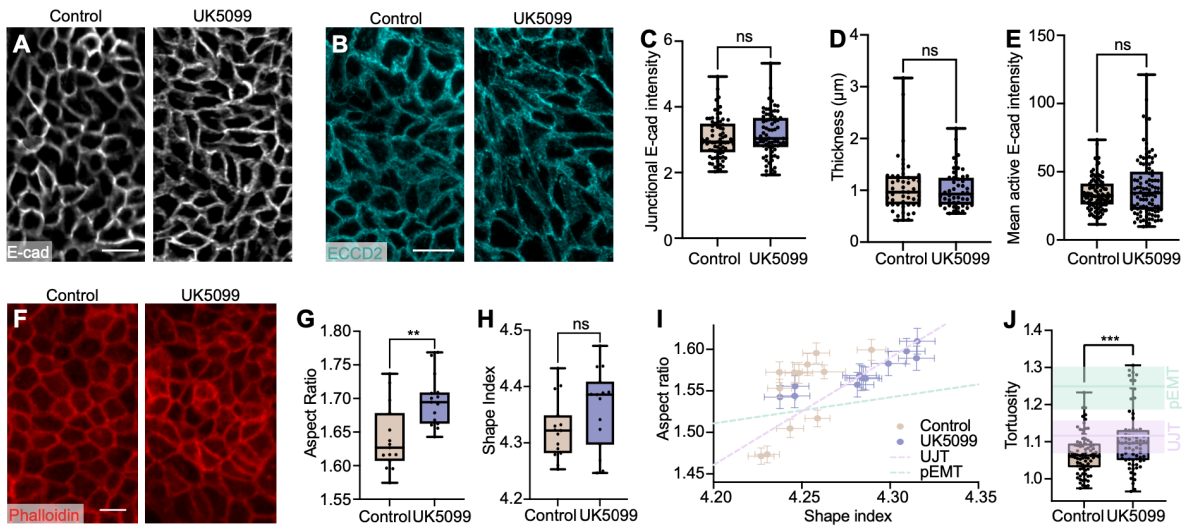

Figure 3.5: Metabolically unjammed cells preserved intercellular junctions while exhibiting a motility-driven elongation morphology.
(A) MDCK cells probed for E-cadherin in control and UK5099 treated cells. (B) MDCK cells probed for ECCD2 (recognizing homophillically bound E-cad) in control and UK5099 treated cells. (C) Quantification of E-cadherin intensity localized at the cell-cell junction. (D) Quantification of E-cadherin junction thickness. (E) Quantification of active E-cadherin intensity localized at the cell-cell junction. (F) MDCK cells stained using phalloidin in control and UK5099 treated cells. (G) Quantification of cell aspect ratio. (H) Quantification of cell shape index. (I) Scatter plot of cell aspect ratio versus cell shape index. Pink dashed line and green dashed line denotes the unjamming transition (UJT) and partial epithelial to mesenchymal transition (pEMT) axes identified in previous literature (Mitchel et al., 2020). Error bars represent standard error. (J) Quantification of cell junction tortuosity. Green and pink solid lines denote the mean tortuosity observed during pEMT and UJT reported in recent literature, respectfully (Mitchel et al., 2020). "ns", **, ***, refer to p-values ≥ 0.05, < 0.01, and < 0.001, respectively.

aspect ratio and shape index in our system by plotting the two against each other (Fig. 3.5I). We observed morphological changes consistent with motility driven elongation in UJT, suggestive that metabolism may be a molecular driver of the UJT.

To further validate this characterization, we evaluated the cell junction tortuosity, as previous work has reported that fluidization resulting from pEMT produces tortuous junctions while the junctions during UJT-induced fluidization demonstrate little tortuosity (Mitchel et al., 2020). In our UK5099 system, we found that most of the cell junctions displayed a tortuosity akin to UJT cells (Fig. 3.5J) reported in previous literature (Mitchel et al., 2020), further implying that UK5099 treatment may induce the UJT.

3.5 Discussion

The epithelial layer typically exists in its functional "solid-like" state, where cells area immotile and quiescent, but can transition to a migratory state when events such as tissue development, growth, remodeling, or wound repair is required. These adaptive transitions can also be exploited in diseases such as tumor invasion or asthmatic airway wall remodeling (Park et al., 2016). In an MDCK monolayer undergoing jamming, we integrated multi-omic time course experiments to characterize cell morphology, transcriptome, and chromatin accessibility, leading to the unbiased identification of cell metabolism as a significantly enriched pathway during jamming. We identified a new molecular pathway to reinstate fluidization in an otherwise jammed, quiescent epithelium. We demonstrated that during jamming, there is a metabolic reprogramming that shift cell metabolism from glutaminolysis to pyruvate aneplerosis, while the oxidative phosphorylation pathway remains the main source of ATP production regardless of the state of confluence. We also discovered that mitochondrial pyruvate carrier inhibition increases uncoordinated cell motion in MDCK cells by physically promoting cytoskeletal elongation and biochemically upregulating the RhoA/Rac pathway. This metabolically-induced motility acts independently of EMT, as we observed maintenance of the E-cadherin junctional thickness and intensity. This finding may reveal important implications in our understanding of cancer dissemination and embryonic morphogenesis, both of which involve substantial metabolic reprogramming (Faubert et al., 2020; Lemma and Nelson, 2023; Tennessen et al., 2014). While these findings significantly advance our understanding of the epithelial jamming transition, they simultaneously bring attention to important open questions in the field.

Previous studies have demonstrated that migrating cells in an advancing epithelium take on a glycolytic metabolic phenotype during wound healing, independent of their position relative to the wound site (DeCamp et al., 2020). Our findings not only agree with this result, but also further shed light on this phenomena by more specifically identifying the metabolic reprogramming from glutaminolysis to pyruvate aneplerosis metabolism observed during jamming. Treating cells with UK5099 could be a useful tool to study how

metabolism-driven unjamming potentially accelerates wound healing, and to understand weather or not collective motion is required for wound healing.

Furthermore, our finding further decouples the effects of density and motility, which are two essential axes comprising the field's current understanding of the jamming phase diagram framework. By only perturbing cell metabolism while leaving the density consistent between conditions, we uncovered that such a metabolic signature is directly associated with cell motility and thus identified the molecular pathway responsible for tuning the fluctuation axis of the jamming phase diagram. It would be important for future work to expand on this finding to test how cells at different densities, and thus with relatively weaker cell-cell junctions, respond to UK5099 treatment to further clarify the metabolic-induced unjamming trajectory in phase space.

This study reveals that metabolism-induced motility lies along the unjamming transition axis rather than partial EMT, as cells maintain E-cad positive with minimal tortuosity of cell-cell junctions. This has important implications in cancer biology, as it may suggest that EMT is not essential for metastasis, potentially revealing metabolism as a biomarker for metastatic potential. Future experiments should explore the effects of UK5099 in cancer spheroid cultures to investigate its effects on metastatic potential, dissemination, and migration phenotype. It would be insightful to study how UK5099 perturbs cell motility in a 3D setting where cells have more surface area to form cell-cell junctions with neighbors, as an increase in cell-cell adhesions has been associated with flocking, which is in contrast to the motility we observed in a 2D setting.

Relatedly, we also morphologically confirmed our system aligned with the UJT phenotype by plotting cell aspect ratio against shape index in which we found UK5099 treatment mainly perturbed aspect ratio. In previous studies, it has been suggested that cell metabolism can be linked to morphology in which cells with a large perimeter demonstrate increased glycolytic activity (DeCamp et al., 2020). Interestingly, it has also been demonstrated that cell morphology can potentially regulate gene expression via epigenetic modifications (Jain et al., 2013). It would therefore be insightful to assess how this metabolic reprogramming influences gene expresion. In our finding, we only observed

a minute perimeter change in response to UK5099 treatment, indicated by the narrow range of shape indices in Fig. 3.5I. Spatial transriptomics could be a powerful tool to harness in unraveling the relationship between morphological and metabolic phenotypes, and if heterogenity in these properties is related to the likelihood of a cell undergoing T1-driven fluidization.

The study of metabolism and epigenetic state is currently and active research field, as many metabolic phenotypes have been associated with post-translational modifications (Kaelin and McKnight, 2013). In our work, we identified a strong correlation between RNA-seq expression and ATAC-seq promoter peak height of metabolic enzymes, suggesting that this may also be the case in our system. Follow up work will investigate the role of chromatin accessibility in metabolically-induced fluidization by performing ATAC-seq in UK5099 treated cells. It would also be important to integrate these findings with spatial transcriptomics to get a more complete understanding of the intricate relationship between morphology, metabolism, and epigenetics. Such experiments will substantially advance the cancer biology and mechanobiology fields.

Although we observed upregulation of Rac and RhoA protein expression, the precise molecular mechanism facilitating the metabolic-induced unjamming requires additional investigation for a complete understanding. Previous studies have identified RAB5A, a GTPase, as a pathway to induce collective cell flocking in an otherwise jammed system (Palamidessi et al., 2019). It would be interesting to investigate RAB5A levels and ERK activity in a UK5099 system to understand if this molecular pathway of unjamming is aligns with the molecular machinery governing the UK5099-induced fluidization, or if this pathways is a unique signature of flocking. Such an experiment will reveal important advancements on our understanding of collective versus uncoordinated motion and thus dissemination.

The jamming transition is an essential process epithelial cells must undergo to maintain tissue integrity, homeostasis, and barrier function, however, these tissues have been known to fluidize to accommodate migration, plasticity, or developmental processes. Our observations gathered from this work suggest that cell metabolism could be a novel way to

initiate tissue fluidization via the RhoA/Rac pathway activation promoting T1 transitions. We also identified that during the jamming transition, cells adopt a metabolism more dependent on pyruvate aneplerosis rather than the glutaminolysis pathway they initially dependent on when subconfluent. This work addresses important open questions in the field investigating how cells receive extracellular cues to biophysically regulate physicals control parameters governing the unjamming transition. Compared to other known pathways to induce unjamming, our metabolic approach occurs physiologically during crowding and can be easily implemented in therapeutic settings.

CHAPTER 4

Epithelial Cell Morphology Heterogeneity Regulates Chromatin Modifications via Nucleus Size Coordination

4.1 Overview

Heterogeneity in cell morphology is ubiquitous across all epithelial collectives and is intimately linked to the tissue mechanical state. However, the origins of cell morphology heterogeneity within a system and its downstream biological effects remain poorly understood. Here, we investigate the morphological evolution of epithelial cells and their nuclei during crowding and identify a persistent correlation between them. We find a consistent log-normal probability distribution for both cell and nucleus areas across several crowding stages and in different epithelial models. This morphological variability is introduced by uneven partitioning during cell division and is sustained thereafter through actomyosin-driven cell-nucleus size coordination. We further show that nucleus morphology impacts the chromatin state, in which constraint of nucleus area downregulates the euchromatic mark H3K9ac and upregulates the heterochromatic mark H3K27me3 by reducing the expression of histone demethylase UTX. Our results reveal that cell morphology heterogeneity extends beyond mere noise and generates diversity in chromatin states.

4.2 Introduction

Variability is inherent in biological systems and can influence the regulations and outputs of biological processes at all length scales (Ilan, 2023; Tsimring, 2014). At the molecular level, chemical reaction noise leads to uncertainties in transcription (Struhl, 2007), translation (Bar-Even et al., 2006), and post-translational modifications (Bowman and Poirier, 2014). At the cellular level, stochastic gene expression imposes profound influences on cell functions, including cell cycle progression (Talia et al., 2007), metabolism (Das Neves et al., 2010), and stress response (Balaban et al., 2004; Rinott et al., 2011). Over the past few decades, substantial efforts have been made to understand the role of noise in gene expression and genome organization, which are usually considered as "upstream noise" (Munsky et al., 2012; Thattai and Van Oudenaarden, 2004). In contrast, cell-to-cell phenotypic heterogeneity, such as morphological variability, is viewed as a consequence of genetic and environmental variations (Pevsner-Fischer et al., 2011; Kiger et al., 2003). As a result, the emergence of cell morphological heterogeneity within a population and its role in regulating gene expression has been relatively underexplored.

Morphological heterogeneity is one of the most noticeable features of phenotypic variability in epithelial cells. Even in a clonal population where all cells are genetically identical, each cell can exhibit a unique size and aspect ratio (AR) (Marcus et al., 1956). Specifically, during epithelial cell crowding, a canonical process wherein cells continue to proliferate until a tightly packed cell layer is formed, each cell's shape can be controlled by its cytoskeletal properties and interactions with the neighboring cells and substrate (Luciano et al., 2022; Fletcher et al., 2014). In addition to these biological regulations, recent studies have also found that cell shape AR in a population follows a nearly universal distribution across different organisms and systems (Atia et al., 2018; Sadhukhan and Nandi, 2022). This universal distribution can be explained by physical principles, such as the packing constraint (Atia et al., 2018), fundamental polygon geometric properties (Sadhukhan and Nandi, 2022), and topological optimal transport (Skinner et al., 2021). These findings thus suggest that the statistical properties

of epithelial cell shapes can be governed by mechanisms that transcend molecular details. However, the process through which morphological heterogeneities initially arise during crowding is not clear, and how similar mechanisms may also regulate the morphological heterogeneity in other organelles, such as the nucleus, remains an important open question.

The functional significance of cell shapes are highlighted in several recent studies that demonstrated the impact of cell shapes on chromatin structures and gene expression (Jain et al., 2013; Makhija et al., 2016). Leveraging engineered single-cell systems, these studies have uncovered the link between cell shapes and chromatin states. For example, cell shape altered by micropatterns can directly influence the levels of lysine trimethylation (Pereira et al., 2020) and acetylation (Jain et al., 2013) of histones, as well as influence the chromosome position(Wang et al., 2017) and chromatin dynamics (Makhija et al., 2016). In addition, deformation of nucleus and cell shapes using topological micro-pillars can induce chromatin structure and gene expression changes (Wang et al., 2023; Li et al., 2015). However, how the epigenetic states of cells are regulated by cell morphological variations in a physiologically relevant setting is not well understood.

To address these questions, we base our analyses on collective cell studies during epithelial crowding, which emulates physiological processes of epithelial biology and has been widely used for studying functional roles of physical cues (Saw et al., 2017; Blonski et al., 2021). In this study, we focus on the emergence of morphological variations and their roles in determining chromatin modifications and organizations. Specifically, we characterized both the cellular and nuclear sizes, in which the nucleus contains several architectural structures that interact with the genome (Foster and Bridger, 2005; Schneider and Grosschedl, 2007) and has been shown to be an important organelle in mechanotransduction (Kalukula et al., 2022; Miroshnikova and Wickström, 2022). By combining such quantitative measurements with pharmacological perturbations, we show that cell and nucleus sizes follow a common log-normal probability distribution, and the cell-nuclear size correlation is regulated by both actomyosin tension and intracellular osmotic pressure balance. Importantly, cell and nucleus size variations are established and maintained upon each cell doubling event, and these size differences have influence

on the expression of UTX, a histone demethylase, which in turn modulates chromatin methylation states, such that nuclear constraint leads to increased H3K27me3. Our results thus demonstrate that cell morphological heterogeneity is not merely a noise during epithelial crowding, but has functional implications on directing the nucleus size and subsequently modulating chromatin changes.

4.3 Materials and Methods

Cell Culture and Drug Treatment

All experiments conducted using Madin Darby Canine Kidney cells (MDCK) were cultured in MEM-α (Fisher Scientific , 12561-056) supplemented with 10% fetal bovine serum (FBS) (Fisher Scientific, 12662-029) and 1% Penicillin-Streptomycin (Fisher Scientific, 15140-122). HaCaT cells were cultured under low-calcium conditions for growth and propagation and under high-calcium conditions for differentiation, as outlined in previous HaCaT culturing protocols (Wilson, 2014). DMEM was used as the base medium for both low-calcium and high-calcium media. Low calcium media was supplemented with 2% 200 nM L-glutamine, 1% of 3.0 mM calcium chloride solution, and 10% low calcium FBS. High-calcium media was made by adding 20 mL of 200 nM L-glutamine, 10 ml of 280 mM calcium chloride solution, and 100 ml of low-calcium FBS to 780 mL of DMEM. Low-calcium FBS was prepared by adding 0.38 g of Chelex 100 resin to 50 mL of FBS and incubating for one hour at 4 °C on a tube rotator. MDCK and HaCaT cells were maintained at 37 °C and 5% CO_2 with humidity. For all MDCK and HaCaT assays, cells were passaged when they reached $\sim$ 80% confluence using Trypsin/EDTA solution (Fisher Scientific, 25300-054). Cells utilized in time course experiments and subconfluent experiments were seeded at 30,000 cells/cm^2, while cells utilized in confluent experiments were seeded at 80,000 cells/cm^2.

To inhibit non-muscle Myosin II, microtubules, and nuclear export, blebbistatin (Millipore Sigma, B0560), nocodazole (Millipore Sigma, M1404), and selinexor (Selleckchem,

KPT-330) were used, respectively. Concentrations used were 5 μM and 10 μM for blebbistatin, 50 nM, 75 nM, and 100 nM for nocodazole, and 10 μM for selinexor. When combined, 10 μM blebbistain was mixed with 30 nM nocodazole. GSK-J1 (Selleckchem, S751) and DS3201 (Selleckchem, S8926) were respectively used as a histone demethylase inhibitor and a histone methylase inhibitor at a concentration of 5 μM. These optimal concentrations were determined by titrating doses to achieve their primary functions without causing other adverse effects, such as apoptosis. All pharmacological agents were administered for 24 hours at 37 °C and 5% CO_2 once cells reached approximately 90% confluence.

Mouse line and procedure

$K14^{Cre}$ (Dassule et al., 2000) and $R26^{mT/mG}$ (Muzumdar et al., 2007) mice were group housed and genotyped as previously published. To generate $K14^{Cre};R26^{mT/mG}$ embryos for experiments, timed pregnancy was set up between $K14^{Cre};R26^{mT/mG}$ mice, and E12.5 embryos were harvested subsequently. Pregnant mice were euthanized by CO_2 followed by cervical dislocation. Both membrane GFP-positive male and female embryos were selected at random and used in all experiments. Embryonic tissues were harvested and fixed in 4% paraformaldehyde (PFA) in PBS overnight at 4 °C. Tissues were subsequently washed with PBS three times and stained as previously described. All mice were maintained in the University of California Los Angeles (UCLA) pathogen-free animal facility. All mouse experiments were approved by the UCLA Institutional Animal Care and Use Committee (Protocol Number ARC-2019-013).

Immunostaining

For cell culture experiments using HaCaT and MDCK cells, cells plated in a 4-chamber Ibidi slide (Ibidi, 80426) were fixed in 10% neutral buffered formalin with 0.03% Eosin (Sigma-Aldrich, F5304-4L) for 10 minutes at room temperature. Cells were then simultaneously permeabilized and blocked using a mixture of 2% Donkey Serum (Fisher Scientific,

D9663-10ML) with 0.25% Triton X-100 diluted in PBS with calcium and magnesium (Fisher Scientific, 14040-133) at room temperature for 30 minutes. After washing three times with PBS, cells were then incubated in a primary antibody solution for 30 minutes at room temperature. The primary antibodies utilized were H3K27me3 and H3K9ac (9733S, 61663, respectively). The cells were then washed three times using PBS before incubating with the secondary staining solution using anti-mouse Alexa Fluor 488 and anti-rabbit Alexa Fluor 647 (Invitrogen, A21042 and 4414S, respectively) secondary antibodies for 30 minutes at room temperature. Nuclei were labeled using DAPI was added along with the secondary antibody.

For mouse embryo staining, the same protocol was utilized except with incubation times of 1 hour for the permeablization/blocking buffer, 24 hours at 4°C for the primary staining solution, 3 hours for the secondary staining solution, and 2 hours for the PBS washes.

Imaging and Analysis

Fluorescent images were acquired using either a confocal microscope (RCM1 with Nikon Eclipse Ti-E, NIS-Elements software) or a widefield fluorescent microscope (Etaluma LS720 Lumaview 720/600-Series software). A 20× WI/0.95 NA, 60× WI/1.00 NA, or 20×/0.75 NA objective was used for images taken using confocal microscopy. A 20×/0.40 NA objective was used for the widefield fluorescent images. The imaging conditions were consistently maintained across all experiments. To quantify fluorescent intensity, z-projected images obtained from z-stack imaging using a step size of $\sim$2 μm were used. In time lapse imaging, images were taken using the Etaluma microscope every 5 minutes for 6 days with media changes performed every other day. Morphological segmentation was performed using Cellpose (Stringer et al., 2021) or Trackmate (Tinevez et al., 2017). Quantifications were performed using MATLAB (version R2023a) or ImageJ (version 2.1.0/1.53c).

Hypotonic shock experiment

MDCK cells with nuclear BFP and plasma membrane GFP were cultured in a 4-chamber Ibidi slide (Ibidi, 80426) until confluent. Z-stack images of both BFP and GFP channels were then acquired using a 60× WI objective. Following this, 10^{-4}% V/V digitonin was added to the cell culture media for 5 minutes and the same imaging protocol was repeated. To introduce a hypotonic environment, the cell culture media containing digitonin is then replaced with a solution 95% Milli-Q water and 5% MEM-α, in which the corresponding osmolarity is then calculated based on the concentration of individual solutes in the final solution. After a 4 minute incubation with the hypotonic solution, cells were imaged using the same imaging procedure described above.

MDCK Cell Transduction

To label plasma membrane with GFP and nucleus with BFP for live imaging, cells were first transfected with a pAcGFP1-Mem vector to produce a plasma-membrane line. These cells were seeded at a density of $2 * 10^4$ cells per well in 12-well plates. Three days after seeding, cells were infected with 250 μL of lentivirus expressing nucleus BFP and 8 ng/μL polybrene (MilliporeSigma, TR-1003-G). The plate was immediately centrifuged at 500×g for 1 hour at room temperature following the infection. After centrifugation, 750 μL culture medium was added without removal of lentiviruses. BFP/GFP double positive clonal populations were sorted by FACS using a BD FACS Aria H. To generate the KASH reporter, MDCK cells were seeded at a density of $2 * 10^4$ cells per well in 12-well plates. Cells were transfected three days after seeding using Lipofectamine Reagents (Invitrogen, 18324012) with 0.75 μg GFP-KASH2 vector (Addgene plasmid no. 187017) and 0.25 μg PiggyBac transposon vector. After neomycin selection, clonal populations were sorted by FACS using a BD FACS Aria H.

Micro-patterning

Micropatterned polydimethylsiloxane (PDMS) stamps, containing circular pillar arrays, were obtained from Research Micro Stamps (Clemson, SC). PDMS stamps underwent sonication in an ethanol bath for sterilization. Following sterilization, the pillars of the stamp were incubated with 20µg/mL fibronectin for 30 minutes at room temperature. The PDMS stamp was then affixed to hydrophobic, untreated petri dishes to transfer the fibronectin. The surface was then treated with Anti-Adherence Rinsing Solution (STEMCELL technologies, 07010) for 45 minutes to minimize nonspecific cell binding.

Data analysis and Statistics

GraphPad PRISM (version 10) and MATLAB (version R2023a) were used to perform statistical analysis and create figures. Data is presented as mean ± standard deviation. For correlative analyses of all presented scatter plots, both the Pearson correlation coefficient and the Spearman correlation coefficient were calculated in addition to the p-value, false discovery rate (FDR), and confidence interval (CI), all of which are summarized in Table S1. False discovery rate (FDR) was evaluated using a Monte Carlo simulation that randomly permutes the X Y values of data points. P-values > 0.05 are denoted as not significant (ns), while p-values ≤ 0.05, ≤ 0.01, ≤ 0.001, and ≤ 0.0001, are represented as *, **, ***, and ****, respectively.

4.4 Results

Correlated evolution of cell and nucleus morphology throughout cell crowding

To understand how cell morphology affects cell behavior, we first set out to examine the evolution of both cell and nucleus sizes, both of which have been shown to play an essential role in transducing mechanical and geometric cues (Kalukula et al., 2022). To do so, we cultured Madin Darby Canine Kidney (MDCK) cells with a seeding density 30k

cells/cm^2 and conducted cell and nucleus segmentation at 24, 64, 72, and 104 hours after seeding (Fig. 4.1A). These timepoints were chosen to capture critical transitions in cell confluency and behavior, encompassing subconfluence, confluence, crowding onset, and a crowded steady-state (Gumbiner, 1996). These distinct stages capture the evolution of cell-substrate and cell-cell interactions, and changes in adhesion strengths and motilities (Garcia et al., 2015). Following known hallmarks of crowding, cell area and nucleus area became progressively smaller, while the adherence junction protein E-cadherin (E-cad) became upregulated and more localized to the intercellular junction (Puliafito et al., 2012).

We next quantified the cell and the nucleus size changes across timepoints. While nucleus and cell sizes refer to their three-dimensional (3D) volumes, within a monolayer, their projected areas are well accepted to approximate the cell and nucleus sizes (Seelbinder et al., 2020; Bankhead et al., 2017). Measuring areas has the benefit of improved statistics, as it enables a higher throughput of data acquisition and analysis. Studying cell and nucleus area would also allow us to compare results with previous studies that mainly performed two-dimensional (2D) analyses (Perez Gonzalez et al., 2018). To validate using area as an approximation for volume in our system, we analyzed the nucleus volume using 3D image stacks (Fig. 6.14A) and showed a strong correlation between area and volume (Pearson correlation coefficient ~ 0.81) in a confluent cell layer (Fig. 6.14B). We further validated our size approximation by demonstrating that the cell layer is relatively flat (Fig. 4.1A middle row and Fig. 6.14C) throughout crowding, consistent with previous findings (Neelam et al., 2016). Together, these results confirmed the reduction of cell and nuclear sizes during epithelial crowding (Fig. 4.1B, 4.1C). Importantly, we found that both cells and nuclei exhibited morphological heterogeneity throughout crowding. The magnitude of such morphological variability, denoted by the large whiskers shown in Figs. 4.1B and 4.1C, well surpassed the magnitude of overall decrease in cell and nucleus area. This finding suggests that the intrapopulation cell-cell variability should not be overlooked when assessing individual cell behavior, as interpreting cell properties solely based on the global average may gloss over important biological information (Han et al.,

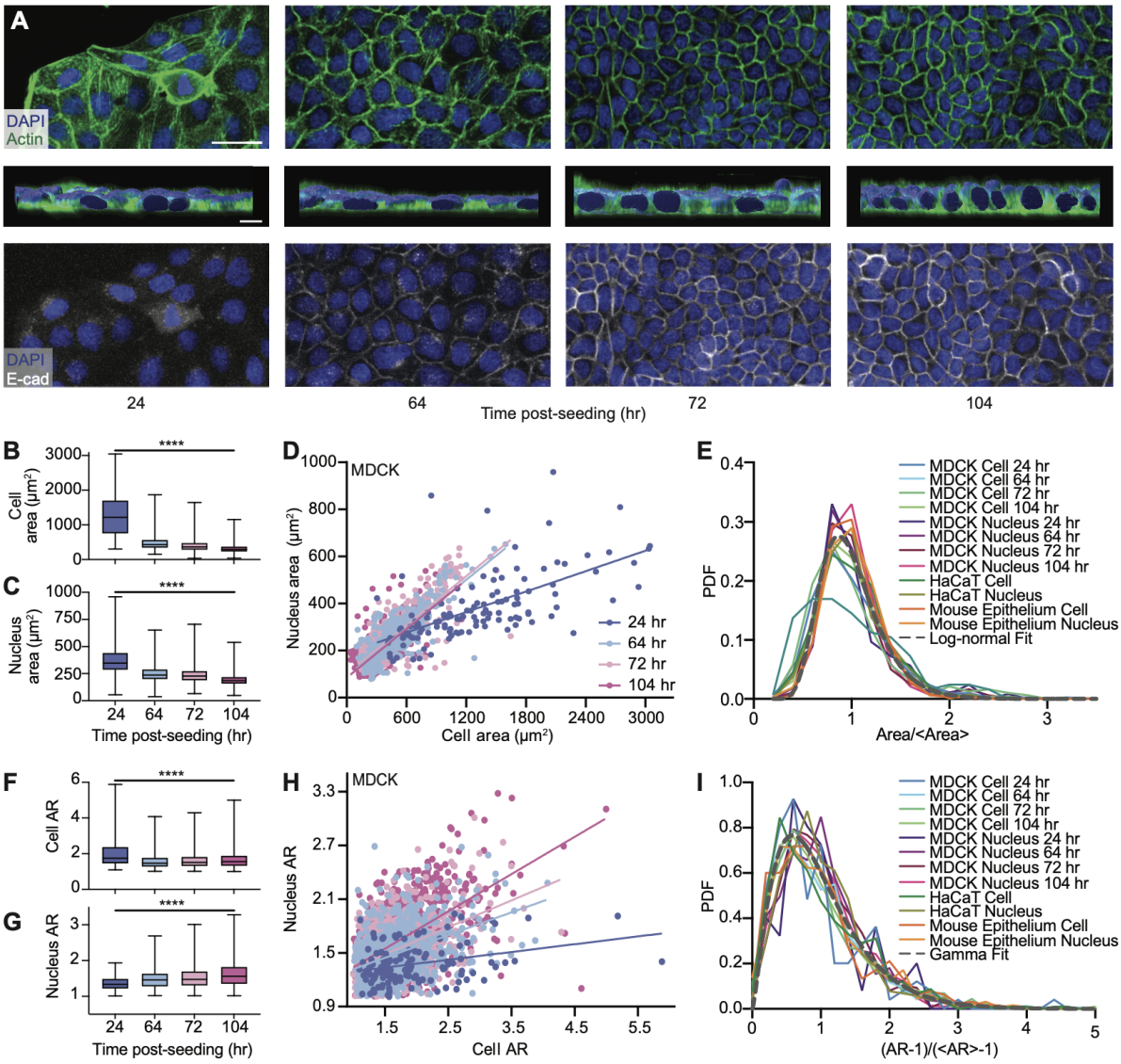

Caption on next page.

2013).

While the variabilities in both cell and nucleus areas may be initially regarded as biological noise, we identified a significant correlation between these characteristics (Fig. 4.1D). Specifically, we found that the nucleus and cell areas are positively correlated throughout crowding, indicating a constant nucleus area to cell area ratio (NC ratio) at each timepoint. Furthermore, this ratio becomes constant upon the 64 hr timepoint when the cell layer reaches confluence. The lower NC ratio at the 24 hr timepoint may be due to cell spreading associated with higher traction forces and actomyosin tension in the

Figure 4.1: Coordinated morphological changes in cells and nuclei during crowding.

(A) Images of MDCK cells demonstrating evolution in cell and nucleus morphology from being subconfluent to crowded (top). Cross-sectional 3D reconstruction of MDCK cells demonstrating monolayer flatness throughout crowding (middle). Scale bar = 10μm. DAPI and actin staining shows that cells progressively acquire a cobblestone-like morphology with decreasing sizes of both cell and nucleus during crowding. E-cadherin (E-cad) staining illustrates the maturation of intercellular junctions in late crowding. Scale bar = 50μm. (B) Quantification of cell area throughout crowding illustrates that the cell area variability surpasses the mean change. N = 124, 732, 803 and 1033 for 24, 64, 72, and 104 hour analyses, respectively. (C) Quantification of nucleus area throughout crowding illustrates that the nucleus area variability also surpasses the mean change. N = 147, 837, 840 and 1107 for 24, 64, 72, and 104 hour analyses, respectively. (D) Persisting nucleus-cell area correlation throughout crowding. 64 hr, 72 hr, 104 hr datasets exhibit the same NC ratio, indicated by the same slope of the best fits (solid lines). N = 124, 808, 802 and 1033 for 24, 64, 72, and 104 hour analyses, respectively. Solid lines represent best linear fits. p-value < 0.0001 for all timepoints. (E) Normalized probability density functions (PDF) for MDCK, HaCaT, and developing E12.5 mouse epithelium cell and nucleus area. All PDFs, except the MDCK cell 24 hr PDF, collapse on a master curve and can be described by a log-normal fit. (F) Quantification of cell aspect ratio (AR) throughout crowding. N = 124, 732, 803 and 1033 for 24, 64, 72, and 104 hour analyses, respectively. (G) Quantification of nucleus AR throughout crowding. N = 124, 808, 803 and 1033 for 24, 64, 72, and 104 hour analyses, respectively. (H) Nucleus-cell AR correlation during crowding showing progressively increased slopes over time. Solid lines represent best linear fits (solid lines). N = 124, 808, 803 and 1033 for 24, 64, 72, and 104 hour analyses, respectively. p-value < 0.0001 for all timepoints. (I) Normalized PDFs for MDCK, HaCaT, and mouse epithelium cell and nucleus AR collapse on a master curve, which can be described by a gamma distribution. **** refers to p-values < 0.0001.

subconfluent state when compared to confluent cells (Hur et al., 2012). To further test if NC ratio is also correlated in other epithelial model systems, we examined the human keratinocyte cell line (HaCaT) and the developing mouse epithelium at embryonic day (E) 12.5, in which the scatter plots are shown in Fig. 6.15. In both cases, we observed NC correlations. Here, while the mouse epithelium is a three dimensional tissue, we analyzed the outermost cells, which form a differentiated and flat layer that can be considered as a two dimensional model system (Richardson et al., 2014). The consistent observation of NC correlation in different models suggests that the nucleus-cell area co-regulation is conserved and likely regulated by a common mechanism across systems.

The observed ubiquitous NC correlation suggests that the morphological variability

of cell and nucleus could be governed by a coordinated process throughout the highly dynamic cell crowding process. To understand the nature of this NC correlation, we next assessed the statistical commonality of such a morphological variability by normalizing the cell and nucleus areas to their respective means (Fig. 4.1E). Aside from the MDCK 24 hr cell area, this normalization revealed a universal collapse of all probability distribution function (PDF) curves, indicating that the area variability for both nucleus and cell share the same statistical properties. We further found that these distributions can be described by a log-normal fit $\mathrm{PDF}(x) \sim \frac{0.25}{x} \exp\left(-\frac{(\ln x+0.05)^2}{0.19}\right)$, consistent with previous findings (Puliafito et al., 2012). Also, the collapse of all curves demonstrates that the degree of area heterogeneity is independent of the post-confluent cell density and model systems, suggesting that the observed feature is conserved in human cells and epithelial development.

Another morphological hallmark of crowding is the transition from an elongated to rounded cell shape, which we confirmed in our MDCK system by measuring the cell AR across different timepoints (Fig. 4.1F). Similar to the area analysis, we also measured nucleus AR throughout crowding (Fig. 4.1G) and found that as the cell AR decreased by 20%, the nuclear AR increased by 10% from the 24 hr timepoint to the 104 hr timepoint. Moreover, both cell and nuclei ARs exhibited variabilities that are greater than the mean change over time ($\sim$ 1.5$\times$mean). Consistent with our area measurements, this observation suggests that heterogeneity must be considered to understand differences between individual cells.

Similar to the nucleus-cell area correlation, there is a mild, but statistically significant, correlation between cell and nucleus ARs in MDCK cells (Fig. 4.1H), HaCaT cells (Fig. 6.16A), and the mouse epithelium (Fig. 6.16B). The ratio between the nucleus and cell ARs increases during crowding, reflecting the simultaneous decrease in cell AR (Fig. 4.1F) and increase in nucleus AR (Fig. 4.1G). After scaling the AR distribution using a previously published (Atia et al., 2018) form $x = (AR - 1)/(\langle AR \rangle - 1)$ where $\langle\rangle$ denotes average, we found that all normalized AR PDFs collapsed to a common curve that can be described by a Gamma distribution $\mathrm{PDF}(x; k) = k^k x^{k-1} e^{-kx}/\Gamma(k)$ where

$\Gamma(k)$ is the Legendre gamma function with $k \sim 2.43$ for our best fit (Fig. 4.1I). This finding is consistent with previous work suggesting that AR heterogeneity in crowded epithelia may be universally described by geometric constraint during jamming transition (Atia et al., 2018). Notably, we found the correlation between area and AR negligible, in which the mean Pearson correlation coefficient is ~ 0.05 (Fig. 6.17). This finding suggests that these two variables are independent morphological features and governed by distinct mechanisms. Overall, our results illustrate that both cells and nuclei share common statistical properties of morphological variability across three distinct epithelial cell models.

Size heterogeneity emerges following cell division

The overall reduction in cell area during crowding must arise from the production of new cells through cell proliferation within a limited space. It is also well known that cell division plays a key role in inducing morphological changes from confluence to a crowded state (Atia et al., 2018). In our experiment, we observed that the cell number tripled from the 64 hr to 104 hr timepoints (Fig. 6.18). This cell number increase prompted us to hypothesize that cell and nuclear morphological heterogeneity may arise following cell divisions, at which point the regulation of NC ratio may have also begun. We therefore set out to track the cellular and nuclear area of dividing cells and their daughter cells, where the plasma membrane is labelled with green fluorescent protein (GFP) and the nucleus is labelled with blue fluorescent protein (BFP) (Fig. 4.2A). We focused our analysis using $\sim 95\%$-confluent monolayers, where cells were crowded but remained proliferative (Fig. 6.18). We then measured the cellular and nuclear area of dividing cells and their daughter cells for 6 hours to observe their morphological evolutions during cell growth. Here, we study areas for up to 6 hours to confirm a stable size has been reached (Fig. 6.19).

As shown by the evolution of cell areas, we found that daughter cells from the same mother do not possess equal areas (0 hr in Fig. 4.2B), rather one is larger than the other. Despite having identical genomes, there is a corresponding difference in nucleus

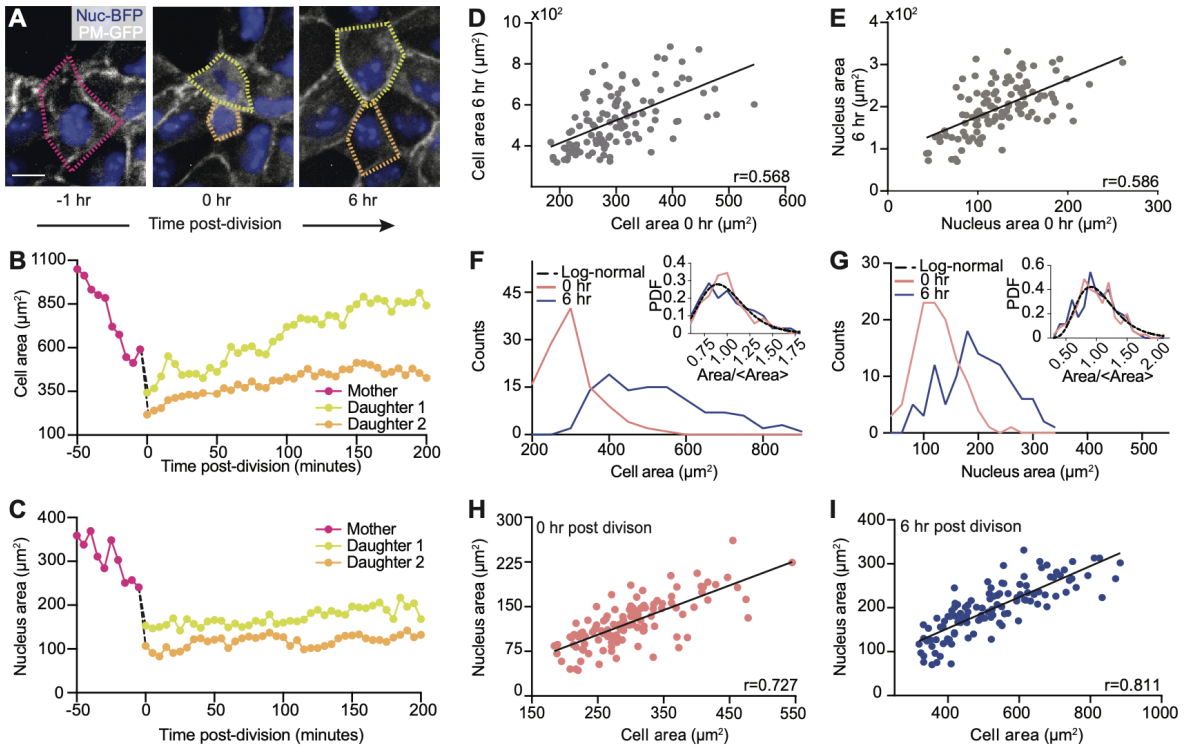

Figure 4.2: Variations in cell and nucleus morphologies arise from uneven cell division.

(A) Images of live cells illustrating cell division and growth. A mother cell 1 hr before division (left). Fuchsia outline denotes mother cell contour. Daughter cells possess different sizes immediately upon division (middle). Yellow outline denotes the larger daughter cell while orange outline denotes the smaller daughter cell. Daughter cells 6 hr after division (right). Scale bar = 15 μm. (B) Cell area evolution of mother and daughter cells shown in (A) illustrates that the area difference increased during cell growth. (C) Corresponding nucleus size evolution shows that the nucleus area differences remained during cell growth. (D) Cell areas at 0 and 6 hrs after division are correlated. N = 116. p-value < 0.0001. (E) Nucleus areas at 0 and 6 hrs after division are correlated. N = 116. p-value < 0.0001.(F) Histogram of cell areas 0 and 6 hrs after division. Inset shows that the normalized cell area PDFs of the 0 hr and 6 hr data can be described by the same log-normal distribution (black dashed line). (G) Corresponding histogram of nucleus areas 0 and 6 hrs after division. Inset shows that the normalized nucleus area PDFs of the 0 hr and 6 hr data can be described by the same log-normal distribution (black dashed line). (H) Nucleus-cell area correlation immediately upon division. N = 116. p-value < 0.0001. (I) Nucleus-cell area correlation 6 hrs after division. Black lines in D, E, H, and I represent best linear fits. N = 116. p-value < 0.0001.

area, with the larger daughter cell owning a larger nucleus (0 hr in Fig. 4.2C). While the size differences between daughter cell size increased, the differences between their nuclei remained relatively constant after $\sim$ 3 hours of growth. By analyzing 58 pairs of

daughters, we confirmed that the area disparity between the two daughters persisted as the cells grew, as demonstrated by the positive correlation between the 0 hr and 6 hr areas for both the cell (Fig. 4.2D) and the nucleus (Fig. 4.2E). The scatter plots also illustrated that the cell area increased more, with a slope of ~ 1.12m, than the nucleus area, with a slope of ~ 0.88, revealing that although co-regulated, most growth occurs within the cells and less so in their nuclei.

The persisting area difference leads to the question of whether the area variability observed in the steady-state system could simply originate from uneven cell divisions. To assess this possibility, we analyzed the statistical properties of cell area and nucleus area at 0 hr and 6 hr after division by plotting their PDFs in Figs. 4.2F and 4.2G, respectively. Consistent with Figs. 4.2D and 4.2E, we found that the distributions of both cell and nucleus area simply broadened as the cells grew. Notably, all PDFs were unimodal and skewed. We found that after normalization, both cell (Fig. 4.2F, inset) and nucleus (Fig. 4.2G, inset) area PDFs can be described by a universal log-normal distribution. This finding suggests that the area variability emerged from uneven cell division and was approximately linearly amplified during cell growth. To understand whether this randomness dominates over any inherited lineage dependent trait, we calculated the cell area-area autocorrelation function, which decays by an order of magnitude at the nearest neighbor distance ~ 10 μm (Fig. 6.20). Such a short correlation length suggests that the final daughter cell area is not an inherit property from mother cells.

The similar evolution between cell and nucleus areas during cell growth indicates that the NC ratio regulation begins as soon as division is completed. To test this, we studied the NC ratio correlation at 0 hr (Fig. 4.2H) and 6 hr (Fig. 4.2I) after division. While we observed a strong correlation regardless of the time after division, the ratio was higher at the 0 hr than at the 6 hr timepoint, which can be attributed to the increase in cell size due to subsequent cell growth after division. This finding indicates that the correlation between cell and nucleus is established before cell growth reaches a steady state following division, and such a correlation is maintained despite their disproportionate size increase during cell growth.

Collectively, our cell division tracking experiments suggest that the cell and nucleus area variability is established in two sequential steps. The first step involves uneven cell division, similar to previously established bacteria models (Amir, 2014). In such models, it has been shown that cell division involves a series of multiplicative random events, which lead to a log-normal distribution of cell size, consistent with our measurements. The second step in the establishment of area distribution is the variability amplification due to size-regulated cell growth, in which the cell growth rate roughly scales with the cell size. Such a cell growth regulation has mainly been observed in unconfined single cells (Cadart et al., 2022). Our results demonstrated a similar mechanism in physiologically confined cells. Lastly, the nucleus and cell size are correlated throughout this two stage process. Our finding also suggests that the log-normal distribution observed in the steady-state cells can simply arise from morphologically asymmetric divisions. In contrast to AR where the origin of heterogeneity is mainly attributed to junctional remodeling (Atia et al., 2018; Sadhukhan and Nandi, 2022), our results indicate that the geometric constraint due to cell-cell interactions mainly determines the final mean size, but not area heterogeneity.

Actomyosin and osmotic pressure balance regulate NC ratio

Having established that all cells within a monolayer share a similar NC ratio, we next asked what mechanism coordinates the nucleus and cell sizes. Previous studies in single cells have shown that nucleus size can be controlled by either cytoskeleton (Li et al., 2014) or intracellular osmotic pressure (Deviri and Safran, 2022; Lemière et al., 2022). To test if these mechanisms play a role in propagating the size heterogeneity from cell to nucleus in confluent epithelia, we performed a series of perturbation experiments to investigate the functional requirement of the cytoskeleton, nucleus-cytoskeleton linkage, and osmotic pressure balance in this context (Fig. 4.3A).

We first investigated whether actomyosin tension regulates nucleus size by measuring the Pearson correlation coefficient of the NC ratio in confluent cells that have been treated with blebbistatin, a non-muscle myosin II inhibitor, or control vehicle (Fig. 4.3B). We

observed a dose-dependent response, as a higher concentration of blebbistatin further attenuates the nucleus-cell area correlation. Notably, although functional actomyosin has been shown to mainly restrict the nucleus height in isolated single cells (Ramdas and Shivashankar, 2015), we here found that it also limits nuclear area and volume in monolayers. We then obtained 3D image stacks of blebbistatin-treated and control nuclei and measured their volumes, since the projected nucleus area change can be due to either volume change or nucleus flattening (Ramdas and Shivashankar, 2015). We found that the area, volume, and height increased by approximately 40%, 75%, and 25%, respectively (Fig. 6.21), suggesting a nearly isotropic expansion of the nucleus when myosin activity is inhibited.

We next assessed the contribution from microtubules, another main component of the cytoskeleton, using nocodazole to inhibit microtubule assembly. However, regardless of the concentrations used, inhibition of microtubules alone was insufficient to reduce the nucleus-cell area correlation (Fig. 4.3C). When mysoin II and microtubules were simultaneously inhibited, we observed a correlation reduction ($\sim$ 30% reduction) similar to the blebbistatin-only samples (Fig. 4.3D, $\sim$ 20% reduction). These results thus suggest that, in confluent epithelia, actomyosin tension plays a more dominant role than microtubules in coordinating the nucleus size with the cell size.

To further understand how cytoskeleton regulates the NC ratio, we investigated the requirements of the nucleus-cytoskeleton linkage, which transfers the strain from the cytoplasm to the nucleus through the Linker of Nucleoskeleton and Cytoskeleton (LINC) complex (Kalukula et al., 2022). To inhibit the nucleus-cytoskeleton linkage, we disrupted the LINC complex by expressing a dominant negative GFP-KASH2 (DN-KASH) protein (Earle et al., 2020). To that end, we found that disruption of the LINC complex significantly reduces the nucleus-cell area correlation (Fig. 4.3E), suggesting that the linkage between the nucleus and cytoskeleton is required for regulating nucleus size.

Besides the cytoskeleton, osmotic pressure balance between the cytoplasm and the nucleus has also been proposed to be a main regulator of nuclear-to-cytoplasmic volume ratio (Deviri and Safran, 2022; Lemière et al., 2022). In this context, the osmotic pressure

difference across the nuclear envelope is predominately driven by active nuclear transport of macromolecules, causing subsequent nuclear size changes. To examine the contribution of osmotic pressure in NC ratio regulation, we first performed a hypo-osmotic shock experiment (Lemière et al., 2022), in which cells were analyzed before and after selective cell membrane permeabilization, followed by an exchange of cell culture medium for a mixture of 95% water and 5% cell culture medium (Fig. 4.3F). This medium exchange reduced the cytoplasmic osmotic pressure from $\sim$ 290 mOsm to $\sim$ 14.5 mOsm (see Materials and Methods), conducive for nuclear expansion. By live imaging cells with nuclear-BFP and plasma membrane-GFP, we found that nuclei significantly swelled after the osmotic pressure drop, while cell size remained roughly constant (Fig. 4.3G). Quantitative measurement showed that nucleus size increased by $\sim$ 50% (Fig. 4.3H), while the nucleus area and cell area correlation was significantly reduced (Fig. 4.3I), likely due to the disproportionate increase in nuclear size across the sample. Osmotic pressure is, therefore, critical for maintaining the NC ratio.

Because osmotic pressure is in part controlled by active transportation of macromolecules across the nuclear envelope (Mukherjee et al., 2016), we next investigated if nuclear transport is required for NC correlation by inhibiting nuclear export using selinexor (SLX), a selective exportin-1 inhibitor (Fig. 4.3J) (Camilli et al., 2023). Consistent with the hypo-osmotic shock experiment described above, we found that nuclei swelled by $\sim$ 1.4 folds in area (Figs. 4.3K,4.3L) 24 hours after selinexor treatment. The corresponding volume increase was also validated by analyzing 3D image stacks (Fig. 6.21). This observation of nuclear expansion is anticipated since molecules could not be shuttled out of the nucleus, leading to an increased osmotic pressure within the nucleus. Importantly, we also observed that the selinexor-treated cells exhibited a significantly lower nucleus-cell area correlation (Fig. 4.3M), suggesting that the macromolecule homeostasis between nuclear and cytoplasmic compartments is required for regulating nucleus size in confluent epithelia. Collectively, our results show for the first time that both osmolarity and the cytoskeleton play an essential role in NC regulation in confluent epithelia.

Nucleus size impacts histone modifications

Is the morphological variability of cells merely a by-product of upstream biological events? Alternatively, could the nucleus size heterogeneity have downstream biological impacts? In the last few decades, seminal studies have demonstrated that physical confinement of cells have profound influences on chromatin organizations, inducing changes in epigenetics and gene expression (Wang et al., 2023; Shivashankar, 2011). Motivated by these findings, we first examined different histone modifications, which control the physical properties of chromatin and the corresponding epigenetic states. For instance, Histone H3 Lysine 27 trimethylation (H3K27me3) is associated with gene silencing, or repression, and with the formation of facultative heterochromatin, while Histone H3 Lysine 9 acetylation (H3K9ac) is an euchromatic mark associated with gene activation (Zhang et al., 2015). By immunostaining H3K27me3 in confluent MDCK cells (Fig. 4.4A) and then analyzing the correlation between nucleus area and H3K27me3 intensity, we found that the H3K27me3 intensity was anti-correlated with the nucleus area (Fig. 4.4B). To control for the intrinsic dependence of intensity measurement on the nucleus size and potential variations in staining and imaging, we normalized the H3K27me3 intensity to the DAPI intensity (Stachecka et al., 2021). The anti-correlation between the normalized H3K27me3 intensity and nucleus area was further confirmed by analyzing isolated nuclei with imaging flow cytometry (Fig. 6.22). Our observed anti-correlation results illustrate that larger nuclei contain less H3K27me3 compared to smaller nuclei. We repeated the same measurement using the developing E11.5 (Fig. 6.23) and E12.5 (Fig. 4.4C) mouse epithelia and observed a similar correlation (Fig. 4.4D), indicative of a conserved process in cultured cells and *in vivo* systems.

Next, we assessed the expression of the euchromatic mark H3K9ac in confluent MDCK cells (Fig. 4.4E). In contrast to the H3K27me3 result, we observed a positive correlation between the nucleus size and H3K9ac intensity, where H3K9ac was upregulated in larger nuclei (Fig. 4.4F). This result was reproduced in the E12.5 mouse embryonic epithelium (Figs. 4.4G, 4.4H). Our results in both MDCK cells and mouse embryos suggest that

there is a universal mechanism dictating H3K27me3 and H3K9ac expression through nucleus size regulation.

To further characterize how nucleus size impacts the chromatin state, we performed systematic spatial analyses of the histone mark intensity within individual nuclei. We focused on two higher-order organization features: chromatin radial distribution and compaction. Here, the radial distribution reports how chromatin is arranged with respect to nuclear lamina (Crosetto and Bienko, 2020), whereas chromatin compaction impacts DNA replication (Liu et al., 2023; Villaseñor and Baubec, 2021) and damage response (Murga et al., 2007). To quantify the radial distribution, we defined the outer 20% of a nucleus as the nuclear periphery and the inner 80% as the center (Fig. 4.4I). We then calculated the intensity ratio between these two nuclear regions. To illustrate the different levels of euchromatin aggregation, we first showed that larger nuclei exhibited more chromatin aggregation when compared to smaller nuclei (Fig. 4.4J). Such an euchromatin aggregation morphology was then confirmed by calculating the coefficient of variation (CV) of the histone intensity (Martin et al., 2021).

By characterizing the radial distribution of H3K9ac in crowded MDCK cells, we found that larger nuclei have less centralized H3K9ac, as illustrated by the positive correlation between the periphery-center ratio and nucleus area (Fig. 4.4K). We also found that this observed correlation does not strongly depend on the split ratio between the nucleus center and the periphery (Fig. 6.24). This finding confirms that nucleus size can influence chromatin spatial distribution. To confirm our findings on the H3K9ac spatial distribution, we performed Airyscan and stimulated emission depletion (STED) microscopy to further visualize stained chromatin marks (Fig. 6.25). By analyzing 16 representative nuclei, we reproduced the positive correlation between the H3K9ac periphery-center ratio and nucleus area (Pearson correlation coefficient ~ 0.29, Fig. 6.25). Lastly, we systematically analyzed how CV and periphery-center ratio correlates with nucleus area for both H3K9ac and H3K27me3, and summarized all the correlation coefficients in Fig. 4.4L. The summary highlights that nuclear size mainly affects the organization of euchromatin, labeled by H3K9ac, more than heterochromatin, labeled by H3K27me3.

Our observed effect of nuclear size on chromatin states is reminiscent to previous micro-patterning constraint studies. In our system, the physical confinement arises from the neighboring cells. To examine if geometric constraint alone without the effect of cell-cell adhesion can induce a similar histone modification change, we micro-patterned 10 μm-diameter fibronectin disks on an anti-adherent substrate to mimic the geometric constraint found in crowded MDCK cells (Fig. 4.4M). We showed that the micro-printed fibronectin was able to confine individual cells. In comparison, subconfluent, unconfined cells exhibited a larger area and irregular cell shape (Fig. 4.4M). Consistent with both previous literature and our findings in monolayers, we found that confinement upregulated H3K27me3 (Fig. 4.4N) and downregulated H3K9ac (Fig. 4.4O) (Hsia et al., 2022; Jain et al., 2013). This finding confirms that geometric constraint can play a role in regulating chromatin modifications. Compared to previous confinement studies, which typically impose a constraint much smaller than the nucleus size (Hsia et al., 2022), our finding suggests that a relatively mild, physiologically relevant constraint emerging during crowding is sufficient to alter chromatin states.

Nucleus size regulates H3K27me3 levels via UTX

To understand how nucleus size alters chromatin states, we investigated the levels of histone-modifying enzymes, which are predominantly responsible for post-translational modifications of histones (Agger et al., 2007). We first characterized how the histone demethylase level depends on nucleus size by immunostaining MDCK cells with UTX (Fig. 4.5A) and compared the normalized UTX/DAPI intensities in the top and bottom 20% of nuclei based on size (Fig. 4.5B). This analysis indicates that UTX levels are anti-correlated with nucleus size (Fig. 6.26A), consistent with our previously observed anti-correlation between the H3K27me3 level and nucleus size. We also assessed how the methylase EZH2 levels relate to nucleus size (Fig. 4.5C), but did not observe a significant correlation (Figs. 4.5D and 6.26). Since UTX and EZH2 play antagonistic roles, we next calculated their intensity ratio (Fig. 4.5E), which could determine the H3K27 methylation level. To that end, we observed a lower EZH2/UTX intensity ratio

in larger nuclei, corroborating the notion that UTX facilitates the coordination between nucleus size and H3K27me3 levels.

To further examine the functional roles of these enzymes, we administered GSK-J1 and DS3201 to inhibit UTX and EZH2, respectively (Fig. 4.5F). We validated both drugs' effects by observing increased H3K27me3 expression upon GSK-J1 treatment and reduced expression upon DS3201 treatment (Fig. 4.5G). By calculating the Pearson correlation coefficient between nucleus size and H3K27me3/DAPI level, we found that the anti-correlation observed in the control group was abolished by either treatment (Fig. 4.5H), demonstrating that both enzymes are required to regulate H3K27me3 levels in response to changes in nucleus sizes. Lastly, since we found that cytoskeletal tension regulates the NC ratio and has been suggested to affect the histone-modifying enzyme recruitment (Jain et al., 2013), we also examined how it affects histone modifications in our system. We found that blebbistatin significantly reduced the UTX level (Figs. 4.5I and 4.5J). Importantly, we also observed reduced correlation between nucleus area and H3K27me3 (Fig. 4.5K) or H3K9ac (Fig. 6.27) levels, indicating that actomyosin is critical for coordinating chromatin modifications with nuclear sizes. Equipped with these findings, we propose in Fig. 4.5L that uneven cell division introduces cell size variation, which propagates into nucleus size variation by actomyosin tension and intracellular osmotic pressure balance. This nucleus size variation, in turn, promotes variation in histone modifications in part through the regulation of UTX expression.

4.5 Discussion

Our paralleled statistical analyses of both the cell morphology and nucleus morphology have provided a detailed statistical description of morphological variabilities in epithelial cells. These analyses unveiled a constant correlation between the cell and the nucleus size, such that they are co-scaled as cell density increases. These results have two important implications on the epithelial cell jamming transition, in which a tissue transitions from a fluid-like state that permits cell rearrangement to a solid-like state that is characterized

by tight cell packing, increased cell-cell adhesion, and reduced cell motility (Angelini et al., 2011; Mongera et al., 2018). First, we demonstrated that the nearly universal distribution of cell size and AR can be extended to the nucleus morphology. This nucleus-cell correlation shows that cells and their nuclei share a similar morphological signature during jamming transition. Therefore, as the cells undergo jamming transition that is facilitated by direct intercellular interactions, nuclei are concurrently influenced by this jamming process through the cytoskeletal tension and osmotic pressure balance. Second, our findings suggest that the variabilities of cell AR and area are governed by distinct mechanisms. Previous studies have demonstrated that cell AR variations are largely impacted by remodeling the intercellular junction (Moshe et al., 2018), which is a multi-cellular effect due to packing. Our result shows that cell area differences, in contrast, are predominantly determined at cell birth, which is mainly a unicellular effect.

Our finding that variability in cell size can arise from uneven cell divisions unveils a source of cell size variability and its universality in a biological system (Ou et al., 2010; Cadart et al., 2014). The current understanding of variability origin is mainly built on conjectures predicting PDFs that are subsequently tested by experiments with a focus on the role of packing geometry. Given that cell divisions can generate daughter cells with different sizes (Kiyomitsu, 2015), our findings here provide a framework on how cell divisions can introduce cell and nucleus size variations within a population, that are subsequently maintained by each cell to generate the observed morphological heterogeneities inherent in the system. Furthermore, our observed persisting cell size disparity supports previously proposed cell growth model by which the molecular synthesis, self-assembly, and transport determine the cell growth rate (Cadart et al., 2019). In future studies, it would be important to determine how cell-cell forces regulate cell cycles and growths, thereby determining the final size of steady-state cells.

To understand how the nucleus-cell size coordination is achieved, we investigated the roles of both active nuclear exportation of macromolecules and actomyosin functions. Our results obtained using a confluent cell layer highlight the importance of intracellular osmotic pressure balance in nuclear size regulation, as well as its requirement for coordinating the

nucleus-cell size ratio. Similarly, perturbations of actomyosin functions or the physical connection of cytoskeleton to the nucleus via LINC resulted in loss of nucleus-cell size coordination as well. Therefore, both osmotic pressure balance and actomyosin are critical for coordinating cell and nucleus sizes. However, it remains unclear whether inhibition of actomyosin hinders nucleus-cell size regulation mechanically or via nuclear transport (Andreu et al., 2022). Future experiments will decipher the two possibilities by observing the elastic response of nucleus upon laser ablation of cytoskeleton. Finally, because asymmetric actomyosin localized at cell cortex can generate unequal forces during cell division to produce daughter cells of unequal sizes (Ou et al., 2010; Cadart et al., 2014), it will be important in the future to determine actomyosin's role in driving size heterogeneities, in addition to the nucleus-cell size correlation we have identified here.

How nucleus morphology can control gene expression, such as through chromatin modifications, is an active research topic (Mukherjee et al., 2016). Leveraging the cell-to-cell variability in our steady-state monolayer system, we directly tested the regulation of chromatin by nucleus sizes without perturbing transient intracellular molecular events, and observed a positive or negative correlation between the nucleus area and the H3K9ac or H3K27me3, respectively. When compared to previous micro-patterning experiments that examined isolated single cells, our observation unveils the pivotal role of nucleus geometry in regulating chromatin organizations in an epithelial monolayer setting. Our result also unveils that UTX facilitates these nucleus size-driven chromatin modifications, in which the UTX levels are controlled by the nucleus size and actomyosin tension. Our finding of the correlation between UTX levels and nucleus size is consistent with recent experiments where nuclear envelope curvature was found to regulate the nuclear pore complex conformation, altering molecular weight-dependent nucleocytoplasmic transport(Andreu et al., 2022). This finding is also consistent with recent theoretical predictions, which posit that the nucleus volume alone can impact the chromatin state by altering the intra-nuclear electrostatic potential (Efremov et al., 2022) and surface area to volume ratio, affecting expression of genes associated with the nuclear lamina (Guelen et al., 2008). Lastly, previous studies have shown that chromatin state and its interaction with the nuclear

envelope can determine nuclear morphology (Lionetti et al., 2020). Our work highlights that a reverse regulation can too take place, as the nuclear morphology, controlled by the cytoskeleton and nuclear transport, can modulate the levels and distributions of different chromatin marks.

Finally, our findings here provide a potential mechanism by which cells in living tissues can generate diversity in cell shapes, fates, and behaviors. For instance, concomitant changes in cell/nucleus sizes and differentiation can occur following asymmetric cell divisions during *Drosophila* neuroblast differentiation (Albertson and Doe, 2003), mouse keratinocyte differentiation (Gdula et al., 2013), and mouse blastocyst patterning (Niwayama et al., 2019). In a pathological setting, cancer cells with larger nuclei are often linked to a more metastatic state (Zink et al., 2004). It is therefore plausible that variations in cell and nucleus sizes, regardless of how they are produced, help generate a spectrum of chromatin modifications that in turn modulate gene expression and fate changes across different cells. Taken together, our results unveil the process through which cell and nucleus sizes are coordinated to control chromatin modifications and distribution, thus translating variations in cell sizes into differences in chromatin organizations. Cell morphological heterogeneity that is present in any tissue may therefore play an important role in generating cell diversity.

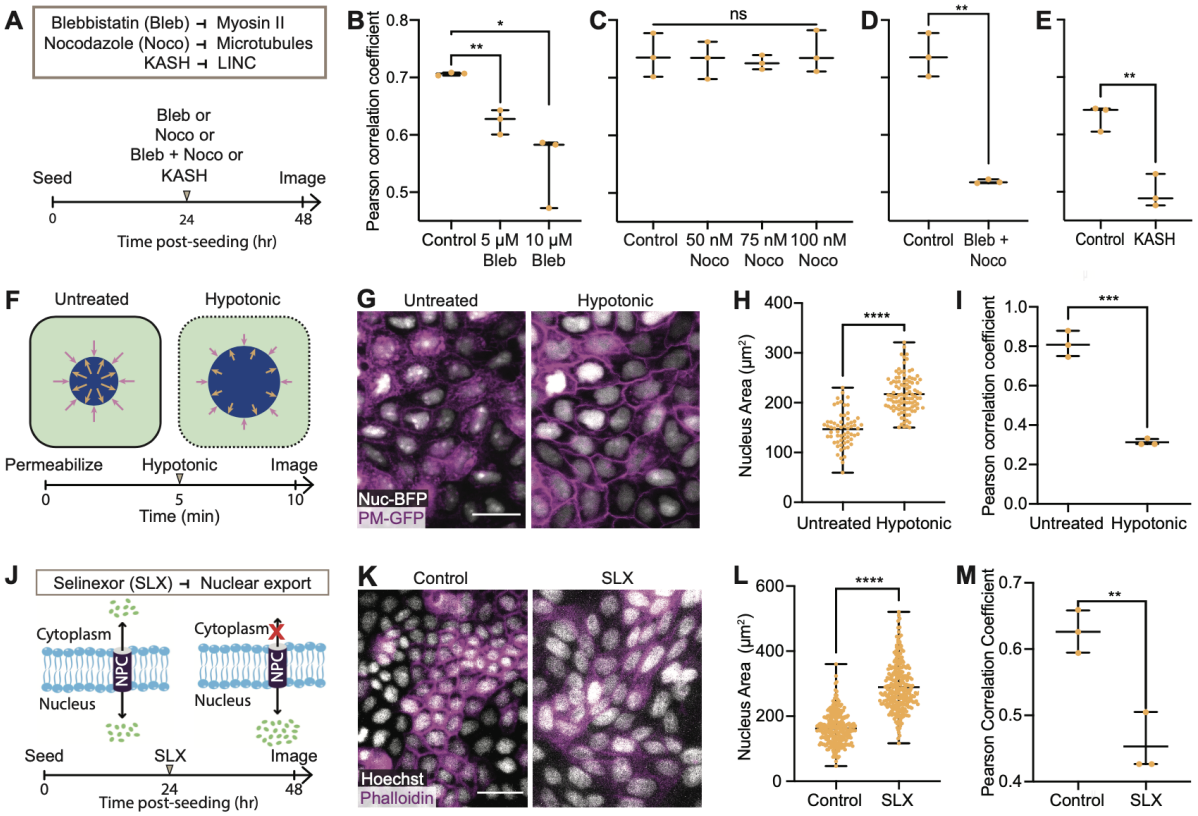

Figure 4.3: Actomyosin and osmotic pressure balance coordinate the cell and nucleus areas.

(A) Experimental overview. Inhibitions of myosin II (blebbistain or Bleb), microtubules (nocodazole or Noco), and the nucleo-cytoskeletal coupling through LINC (KASH) were performed for 24 hours before sample characterization. (B-E) Pearson correlation coefficient of cell area and nucleus area in (B) Bleb-treated cells, (C) Noco-treated cells, (D) Bleb- and Noco-treated cells, and (E) KASH cells. (F) Schematic illustrating the hypotonic experiment overview and timeline. Cells were first treated with digitonin for 5 minutes to selectively permeabilize the cell membrane (dotted outline). Cell culture medium was subsequently exchanged with a 95% water solution, inducing a decrease in osmotic pressure. Purple and gold arrows indicate osmotic pressure into and out of the nucleus, respectively. Reduction of arrow size in the hypotonic cell illustrates a decrease in osmotic pressure. (G) Image of control and hypotonic-shocked cells. Nuc-BFP/PM-GFP cells were used for real-time visualization of cell and nucleus morphology. Scale bar = 25 μm. (H) Nucleus area of untreated and hypotonic-shocked cells. (I) Pearson correlation coefficient of cell area and nucleus area of untreated and hypotonic-shocked cells. (J) Schematic illustrating that selinexor (SLX) inhibits nuclear exportation through nuclear pore complex (NPC), increasing the intranuclear osmotic pressure. Cells were treated with SLX for 24 hours before characterization. (K) Image of control and SLX-treated cells. Scale bar = 25 μm. (L) Nucleus area of control and SLX-treated cells. (M) Pearson correlation coefficient of cell area and nucleus area of control and SLX-treated cells. All correlation measurements shown in B, C, D, E, I, and M were conducted using at least N = 100 cells, in which all p-values < 0.05. "ns", *, **, ***, ****, refer to p-values ≥ 0.05, < 0.05, < 0.01, < 0.001, and < 0.0001, respectively.

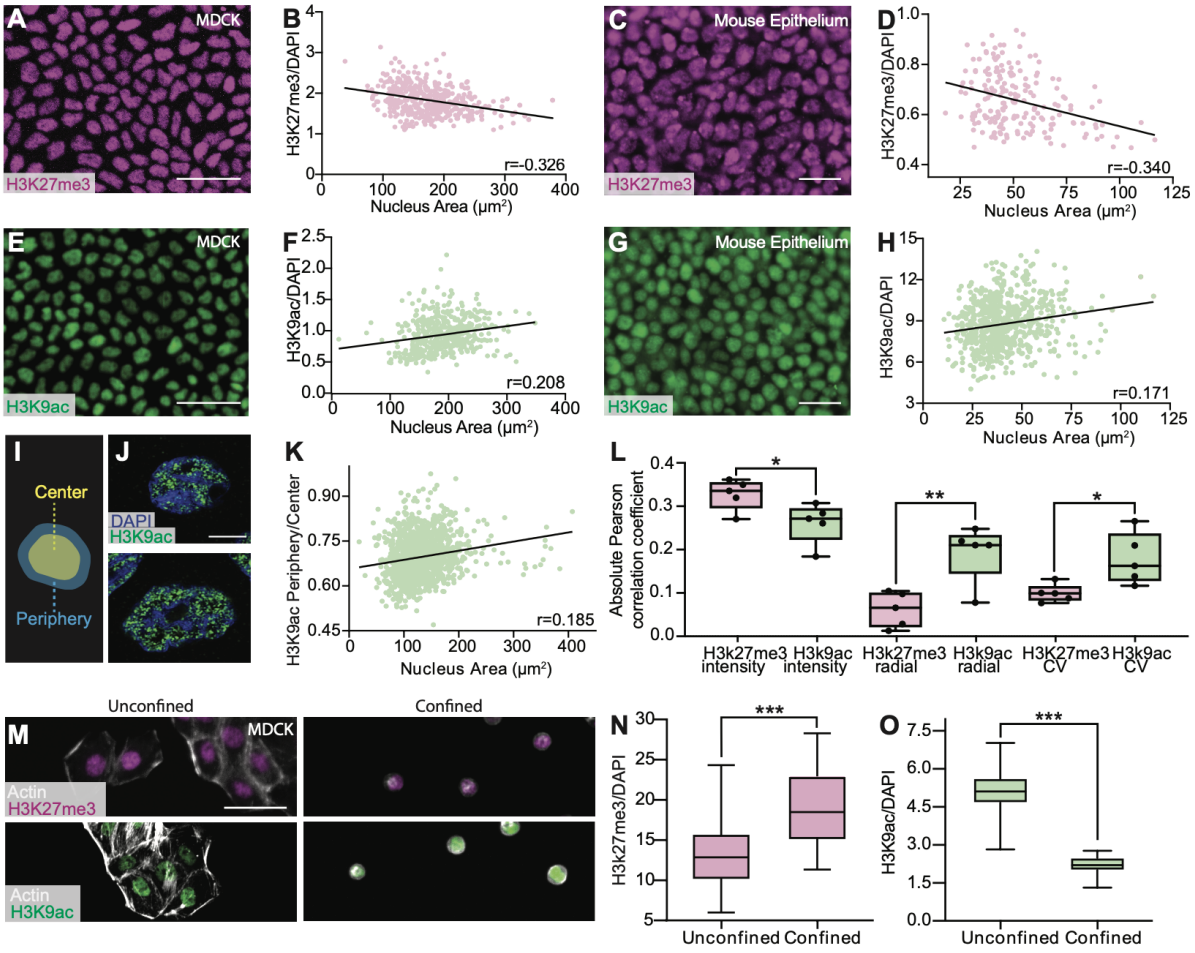

Caption on next page.

Figure 4.4: Nucleus size regulates the expression of histone marks.

(A) Image of MDCK cells stained with Histone H3 Lysine 27 trimethylation (H3K27me3) illustrating its variable expression levels in different cells. Scale bar = 50 μm. (B) Correlation between normalized H3K27me3 expression level and nucleus area in MDCK cells. N = 461. (C) Image of an E12.5 mouse epithelium stained with H3K27me3. Scale bar = 25 μm. (D) Correlation between normalized H3K27me3 expression and nucleus area in the mouse epithelium. N = 130. (E) Image of MDCK cells stained with Histone H3 Lysine 9 acetylation (H3K9ac). Scale bar = 50 μm. (F) Correlation between normalized H3K9ac expression and nucleus area in MDCK cells. N = 1130. (G) Image of an E12.5 mouse epithelium stained with H3K9ac. Scale bar = 25 μm. (H) Correlation between normalized H3K9ac expression and nucleus area in the mouse epithelium. N = 713. (I) Schematic of the nucleus region split for radial distribution analysis. Yellow shaded region occupying 80% of total nucleus area is classified as the center, while the outer 20% shaded in blue is classified as the periphery. (J) Airyscan image of a small (top) and large (bottom) nucleus of crowded MDCK cells illustrating differences in the radial distribution of H3K9ac. Scale bar = 5 μm. (K) Correlation between H3K9ac periphery-center ratio and nucleus area of crowded MDCK cells. N = 1246. (L) Summary of the absolute value of the Pearson correlation coefficient between nucleus area and intensity or spatial distribution analyses in crowded MDCK cells. N = 5. (M) Images of unconfined (left) and confined (right) MDCK cells stained with H3K27me3 (top) or H3K9ac (bottom). Cells were confined using circular 10 μm fibronectin micro-patterned substrates. Scale bar = 50 μm. (N) Box and whisker chart demonstrating an increase of normalized H3K27me3 intensity in confined cells. N= 59 and 75 for unconfined and confined cells, respectively. (O) Box and whisker chart showing a decrease of normalized H3K9ac intensity in confined cells. N = 50 and 52 for unconfined and confined cells, respectively. *, **, and ***, refer to p-values < 0.05, < 0.01, and < 0.001 respectively.

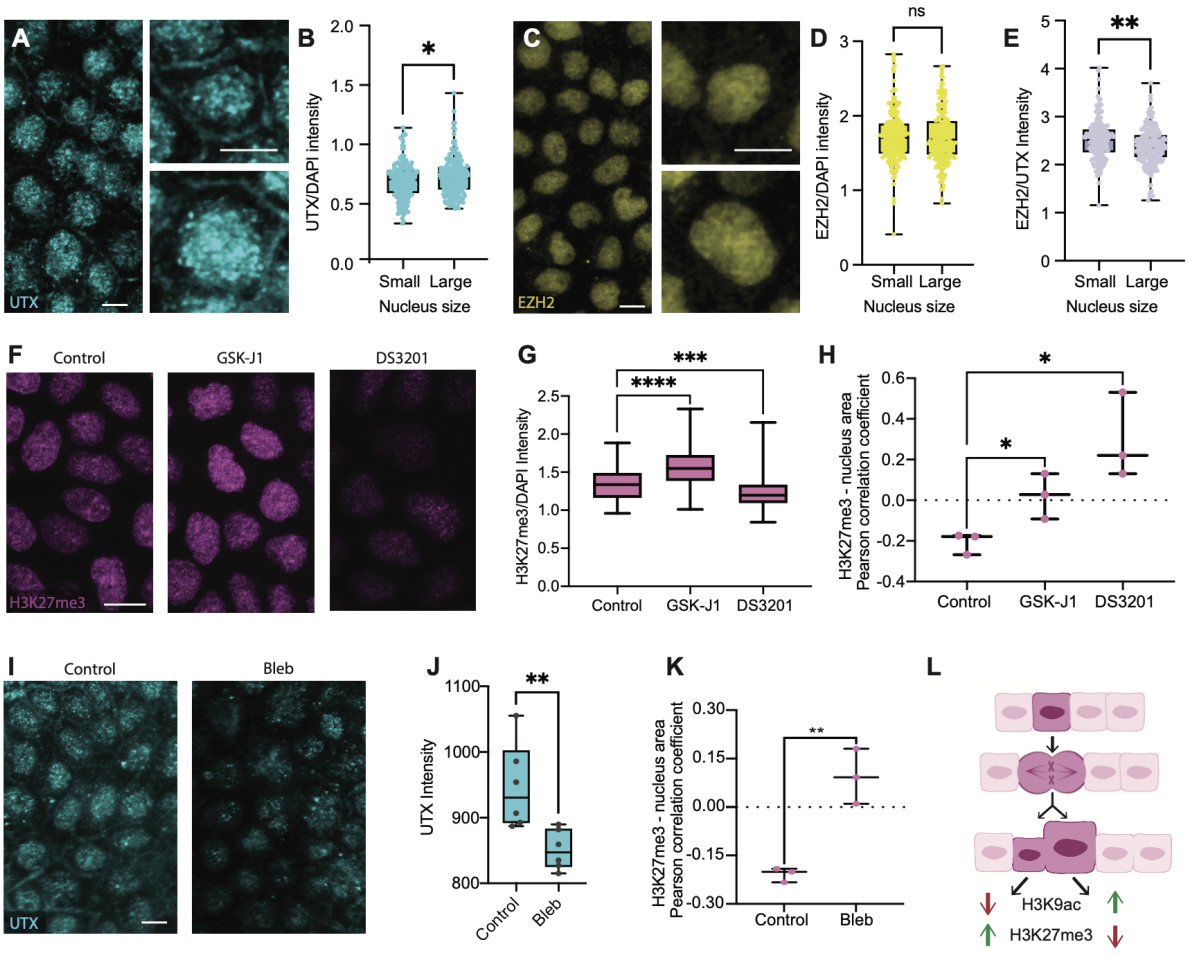

Caption on next page.

Figure 4.5: UTX coordinates with nucleus size and regulates H3K27me3 levels.

(A) MDCK cells stained for UTX with example images of small (upper right) and large nuclei (bottom right). (B) The UTX/DAPI intensity of the smallest 20% of nuclei (Small) is significantly lower than that of largest 20% of nuclei (Large). N = 295 pooled from 3 replicates. (C) MDCK cells stained for EZH2 with example images of small (upper right) and large nuclei (bottom right). (D) EZH2 levels displayed no significant difference between small and large nuclei. N = 295 pooled from 3 replicates. (E) EZH2/UTX intensity ratio is higher in small nuclei than in large nuclei. N = 295 pooled from 3 replicates. (F) MDCK cells stained for H3K27me3 in control, GSK-J1 and DS3201 samples. (G) GSK-J1 and DS3201 respectively increased and decreased the H3K27me3 levels. N = 77, 217, and 294 for control, GSK-J1, and DS3201, respectively. (H) Pearson correlation coefficient between nucleus size and H3K27me3 intensity for control, GSK-J1, and DS3201 treated cells. GSK-J1 and DS3201 treatments reduced the anti-correlation between nucleus size and H3K27me3 intensity. Dotted line denotes no correlation. (I) MDCK cells stained for UTX in control and blebbistatin-treated (Bleb) samples. (J) Bleb samples exhibited lower UTX levels than control. (K) Pearson correlation coefficient between between nucleus size and H3K27me3 intensity for control and Bleb samples. Dotted line denotes no correlation. (L) Proposed mechanism of how heterogeneous cell morphology generates diversity in nucleus size and chromatin states. In a crowded epithelial monolayer, a mother cell divides unevenly into two daughter cells with different sizes, which persists thereafter. Each cell size then propagates through actomyosin tension and intracellular osmotic pressure balance to determine the corresponding nucleus size. Cell size heterogeneity thus gives rise to nucleus size heterogeneity, which in turn contributes to the varying UTX levels and thus chromatin modifications. Scale bar = 10 μm. p-value < 0.05 for B, D, F, H, and K. "ns", *, **, ***, ****, refer to p-values ≥ 0.05, < 0.05, < 0.01, < 0.001, and < 0.0001, respectively.

CHAPTER 5

Conclusions

5.1 Summary

Epithelial cells are integral components of our body's organs, fulfilling vital physiological functions by forming linings throughout. In processes like tissue development, injury repair, and wound healing, these cells undergo a phenomenon known as cell crowding, or jamming, where they migrate and multiply until they form a compact, quiescent layer. To comprehend the transition from fluid-like to solid-like behavior in epithelial tissues, researchers have applied the jamming transition framework originally developed to describe inert granular systems, focusing on factors such as cell density, shape, and movement. However, the molecular mechanisms governing these factors and their biological consequences are still relatively unexplored. In my thesis, I established a methodology to investigate modulus variation within live cell layers, revealing a relationship between cell size and stiffness. To do so, I developed a platform integrating AI, cell stretching, and confocal imaging to reveal supracellular mechanical heterogeneity within an epithelial monolayer. This exploration deepens our understanding of how cellular mechanical properties influence morphology. Additionally, through integrating transcriptomics and metabolomics, I delineated the role of cellular metabolism in regulating motility during crowding. Using a multi-omic approach, I identified metabolism to play a role in regulating jamming. Through inhibition experiments using UK5099, I found that pyruvate plays a role in regulating the cell motility. I also determined that the metabolically-driven motility changes are largely constituted from T1 transitions rather than flocking. Furthermore, I elucidated the origins of morphological diversity in epithelial layers and how such diversity

can impact gene expression patterns. I identified asymmetric cell division to induce cell size heterogeneity which then gets propagated to nucleus size heterogeneity via osmotic pressure and cytoskeletal regulation. I then discovered that nucleus size heterogeneity is correlated with histone modifications for both a heterochromatic and euchromatic mark. Lastly, I found that histone modifying enzymes play an important role in such a coordination. Collectively, these discoveries advance our understanding of epithelial cell behavior, the jamming transition, and mechanobiology with important applications in development and cancer studies.

5.2 Outlook

While this work led to many exciting discoveries in understanding epithelial cell behavior during crowding, it also opened many interesting avenues for future investigation. For example, what regulates cell metabolism during crowding? How does metabolism regulate cell motility? What is actomyosin's role in driving size heterogeneities? Can we engineer a tissue to be morphologically homogeneous? In this section I will discuss the most critical follow up work I envision the field will address in the near future.

Using a multi-omic approach, I identified metabolism as a molecular regulator of the jamming transition, specifically of the fluctuation axis of the jamming phase diagram for active matter. However, to fully understand this regulator, it will be important to further investigate the mechanism of how the cell metabolism is regulating motility. Our preliminary results suggest that the upregulation of the RhoA/Roc activity could be a possible pathway. To understand this regulation, it would be essential to perform traction force microscopy on control and UK5099 treated cells. This could reveal if there is increased traction in the UK5099 system.

It is, however, possible that we do not see any increase in traction. Recent theoretical have demonstrated (Petridou et al., 2021; Bi et al., 2015) that cells can increase their motility without increasing traction forces. In context of our system, I see this as a strong possibility. In our jammed system, we observed that the E-cad junction strength and

thickness is maintained in the UK5099 treated system. This suggests that the cell-cell adhesion strength is likely much stronger than the cell-substrate adhesion. In fact, it is important to note that in an *in vivo* system, many epithelia are not attached to a substrate, but instead float on a fluid layer or yolk, as observed in developmental processes such as Drosophila and Zebrafish early ectoderm and embryonic disks of mammalian and avian embryos. In these systems, forces exerted between the cells dominate the mechanics compared to traction forces with the substrate. Therefore, in our system, it is possible that traction forces are negligible compared to the junctional tensions on the apical side. To assess this possibility functional inference analysis would be required.

Understanding what induces this metabolic reprogramming will also be valuable to developmental and cancer biology fields. Our preliminary results suggests that epigenetics could be the driver of this reprogramming. We observed similar trajectories of chromatin accessibility and gene expression, illustrated by Figs 3.1 H and I. When further investigating genes related to metabolic enzymes, we found not only that the ATAC and RNA expressions were in qualitative agreement (Figs 3.1 N), but also that the Pearson correlation coefficient between the two was moderate to high and significant for most genes (Figs 3.1 O). Performing ATAC-seq on jammed, untreated cells and jammed, UK5099-treated cells would be insightful to reveal any differences in promoter accessibility to guide future inhibition experiments.

To get a more complete picture of how tissue solidification and/or fluidization acts as an upstream cue to induce downstream phenotypic changes, it is important to further investigate how this cue perturb gene expression. Although I demonstrated how nucleus size, which is strongly correlated wit cell size, can perturb epigenetic state, further investigations should explore how this finding translate to the gene expression level. Specifically, future work should harness spatial transcriptomics to unravel the relationship between cell morphology and gene expression. Coupled with the findings presented here, this analysis may provide convincing evidence that cell morphology influences gene expression and thus cell behavior which is in contrast to the current paradigm in the field suggesting that gene expression is the regulator of cell morphology.

Lastly, at a higher-level, the question of how studying heterogeneity advances the biology field should be considered. Heterogeneity is often utilized as a survival mechanism for cancer cells, making it much more difficult to treat as it is more likely at least some population of the tumor is treatment-resistant. This heterogeneity significantly impacts disease prognosis and patient quality of life. Despite its role in diseases, heterogeneity is not always a burden. In developmental biology, Conrad Hal Waddington introduced the concept of the "epigenetic landscape" (Moris et al., 2016) to illustrate how cells differentiate into various cell types during development. This landscape metaphorically depicts the process of differentiation as a ball rolling down a landscape of hills and valleys, with each valley representing a stable cell type. Here, heterogeneity can be thought of as the property that drives cells to different fates. Heterogeneity arises as cells within a population follow different paths or trajectories as they undergo differentiation. Some cells may differentiate into one cell type, while others may follow a different developmental pathway and differentiate into another cell type. Since heterogeneity is essential for determining the biological ecosystem and is also an important survival mechanism, it will be important to explore of findings in context of developmental biology and disease models.

CHAPTER 6

Appendix

Time point	Pearson Coefficient	Spearman Coefficient	p-value	FDR	95% Confidence Interval
24 hr	0.6365	0.766	< 0.0001	$< 10^{-5}$	[0.518, 0.731]
64 hr	0.8326	0.838	< 0.0001	$< 10^{-5}$	[0.810, 0.853]
72 hr	0.7980	0.7506	< 0.0001	$< 10^{-5}$	[0.771, 0.822]
104 hr	0.7007	0.7066	< 0.0001	$< 10^{-5}$	[0.668, 0.731]

Table 6.1: Summary of correlative analyses for MDCK nucleus area vs. cell area. To quantify correlation, both the Pearson (column 2) and Spearman (column 3) correlation coefficient were measured. To quantify statistical significance the p-value (column 4), false discovery rate (FDR) (column 5), and 95% confidence interval (column 6) were computed.

Time point	Pearson Coefficient	Spearman Coefficient	p-value	FDR	95% Confidence Interval
24 hr	0.3031	0.2359	< 0.0001	$< 10^{-5}$	[0.134, 0.455]
64 hr	0.4244	0.4047	< 0.0001	$< 10^{-5}$	[0.366, 0.479]
72 hr	0.4455	0.3858	< 0.0001	$< 10^{-5}$	[0.388, 0.499]
104 hr	0.5749	0.5272	< 0.0075	$< 10^{-5}$	[0.533, 0.614]

Table 6.2: Summary of correlative analyses for MDCK nucleus AR vs. cell AR. To quantify correlation, both the Pearson (column 2) and Spearman (column 3) correlation coefficient were measured. To quantify statistical significance the p-value (column 4), false discovery rate (FDR) (column 5), and 95% confidence interval (column 6) were computed.

Figure	Pearson Coefficient	Spearman Coefficient	p-value	FDR	95% CI
Cell area 6 hr vs. cell area 0 hr	0.568	0.6087	< 0.0001	$< 10^{-5}$	[0.431, 0.679]
Nucleus area 6 hr vs. nucleus area 0 hr	0.586	0.5711	< 0.0001	$< 10^{-5}$	[0.452, 0.694]
Nucleus area vs. cell area (0 hr)	0.727	0.6985	< 0.0001	$< 10^{-5}$	[0.628, 0.803]
Nucleus area vs. cell area (6 hr)	0.811	0.8444	< 0.0075	$< 10^{-5}$	[0.738, 0.865]
MDCK H3K27me3/DAPI vs. nucleus area	-0.326	-0.3280	< 0.0001	$< 10^{-5}$	[-0.447, -0.194]
Mouse ectoderm H3K27me3/DAPI vs. nucleus area	-0.340	-0.319	< 0.0001	$< 10^{-5}$	[-0.459, -0.209]
MDCK H3K9ac/DAPI vs. nucleus area	0.239	0.2969	< 0.0001	$< 10^{-5}$	[0.183, 0.293]
Mouse ectoderm H3K9ac/DAPI vs. nucleus area	0.171	0.1674	< 0.0001	$< 10^{-5}$	[0.0988, 0.241]
Mouse ectoderm H3K9ac P/C intensity vs. nucleus area	0.185	0.1234	< 0.0001	$< 10^{-5}$	[0.131, 0.238]

Table 6.3: Summary of correlation and statistical analyses. Pearson and Spearman correlation coefficients were calculated. Statistical significance was assessed using the p-value, false discovery rate (FDR), and 95% confidence interval (CI).

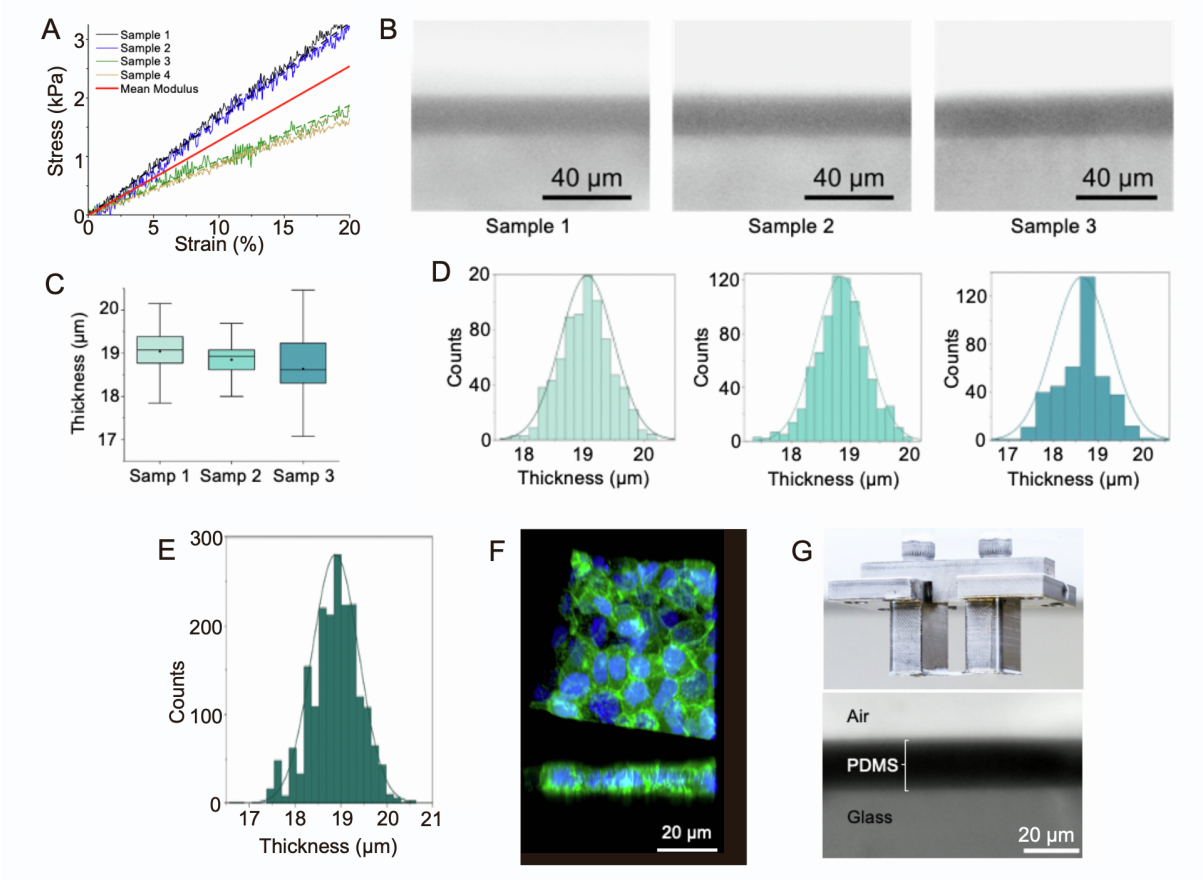

Figure 6.1: PDMS membrane characterization.
(A) Stress-strain curves for 4 independent samples of Sylgard 184 (50:1 base-curing agent formulation). Modulus values were obtained by determining the slope of each curve in the linear regime. The mean modulus (12.7 ± 4.2 kPa) of the 4 samples is shown in red. (B) PDMS sample thickness uniformity. Three representative samples of 50:1 S184 spin coated on glass coverslips were measured to have thicknesses of 19.0 μm, 18.8 μm, and 18.6 μm, respectively. (C) Box plot summarizing the thickness measurement of the samples shown in (D). Results show a mean thickness of 18.9 μm, which is consistent from sample to sample. Standard deviation demonstrates ¡10% thickness fluctuation. This measurement demonstrates high uniformity and reproducibility of membrane thickness. Scale bar = 40 μm. (D) Corresponding thickness histograms of the samples shown in (D). The histograms can be described by a Gaussian distribution, with a relatively small standard deviation, suggesting a uniform thickness across each sample. (E) Thickness histogram of all three samples shown in (D) combined. Similarly, the combined thickness measurements can be fit by a Gaussian distribution centered at 18.9 μm. (F) 3D confocal reconstruction of MDCK cells. MDCK monolayer thickness was measured using confocal z-stack imaging and found to be 9.2 ± 0.7 μm. This cell height measurement was used for FEA. Scale bar = 20 μm. (G) Freestanding PDMS monolayer supported by jig. A PDMS layer suspended between jig legs was measured to be 18.9 ± 0.5 μm. This PDMS thickness measurement was used as an FEA simulation parameter.

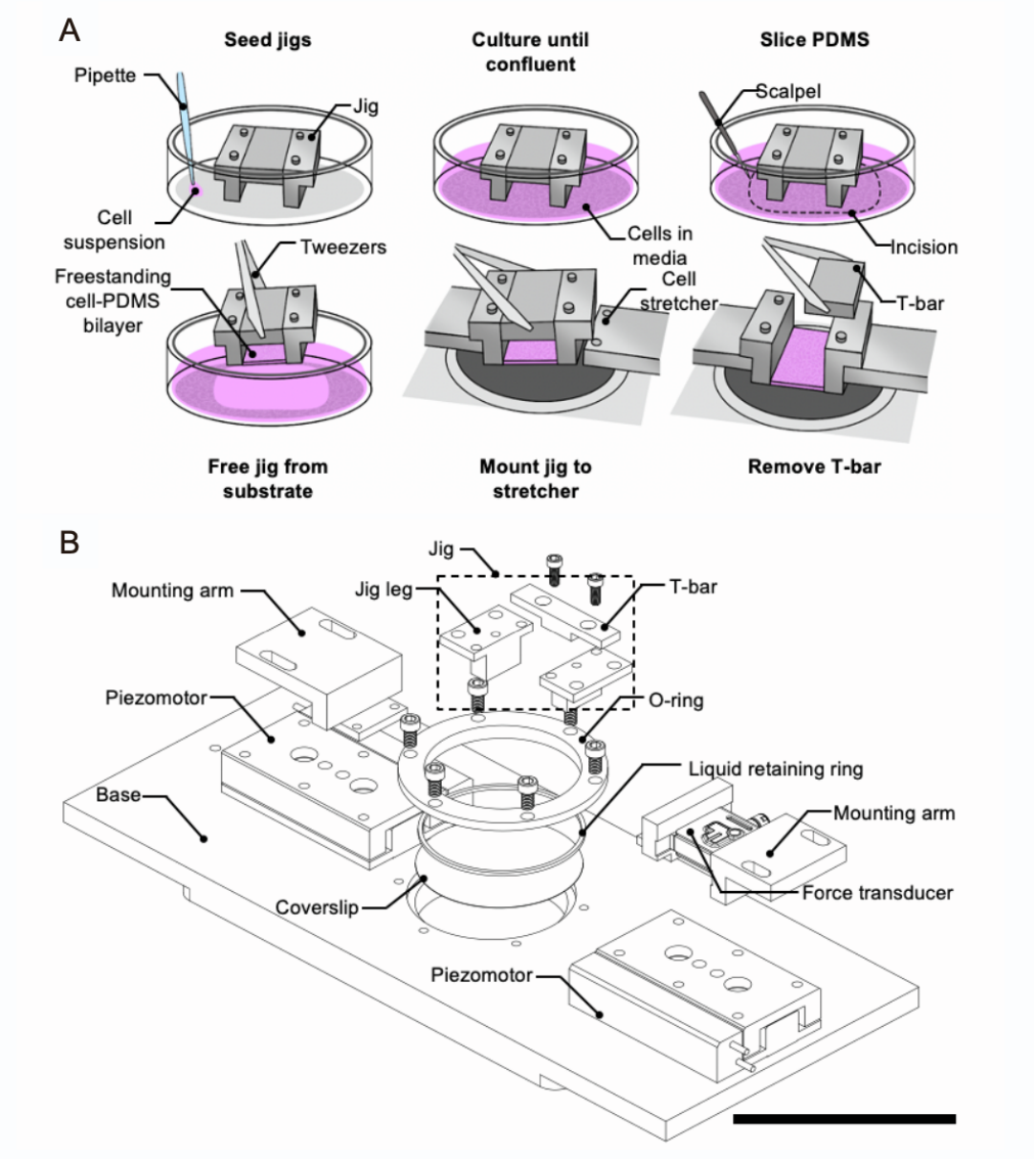

Figure 6.2: Bilayer sample preparation and cell stretcher schematic. (A) Schematic illustrating the main sample preparation steps: cell seeding and sample mounting. Cells are seeded on an autoclaved PDMS membrane that was spin coated on top of a PVA-covered glass coverslip. Cells are then cultured as described in the Materials and Methods, where the culture media dissolves the sacrificial PVA layer. Upon cell confluency, a scalpel is used to make an incision around area spanned by the jig legs. Following this, the jig can be freed from the substrate to yield a freestanding cell-PDMS bilayer, which is then mounted onto the stretcher arms using screws. Finally, the T-bar is removed to enable stretching and imaging. (B) Explosion diagram showing the individual components of our custom cell stretcher. The boxed components (T-bar and jig leg) represent the jig used for sample transportation and mounting. Together, the coverslip, liquid retaining ring, and O-ring form a liquid reservoir that can be imaged through. The base of the cell stretcher can be placed directly on top of a microscope for imaging. Scale bar = 50mm.

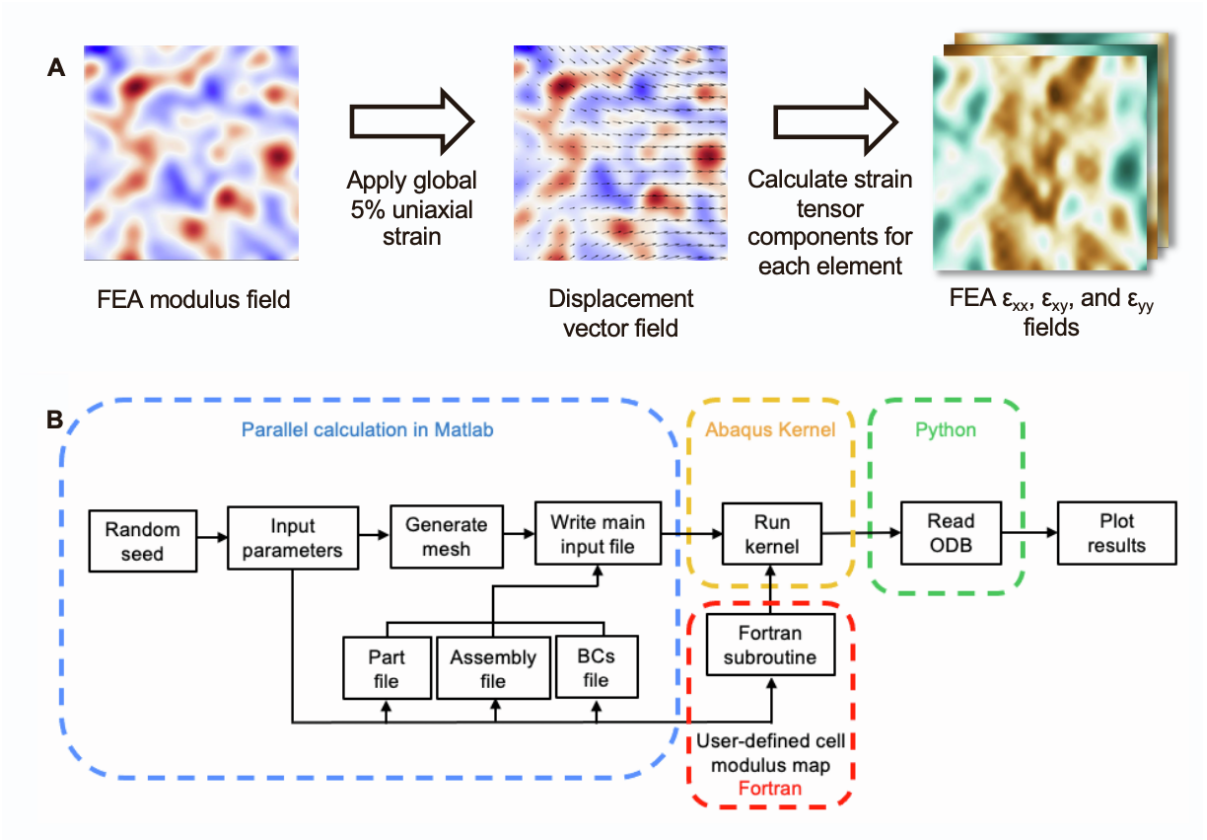

Figure 6.3: Generation of FEA simulation training data.
(A) Approach overview used during FEA simulations to generate AI training data. After ensuring our simulations numerically describe the mechanical response of our cell-PDMS bilayer as previously described, we randomly assigned modulus values to cells in an FEA simulated monolayer. Following this, a 5% tensile strain is applied to the simulated cell-PDMS bilayer to obtain a displacement field. This displacement field was then used to calculate $\epsilon_x x$ (shown), $\epsilon_x y$, and $\epsilon_y y$. This process was repeated to generate $\sim$ 500 training data sets to be used as inputs in our AI inference model. The resulting FEA strain heatmaps exhibit a heterogenous strain distribution due to varying cell stiffness. An example of an FEA $\epsilon_x x$ heatmap is shown. (B) FEA simulation flowchart of strain calculations performed using ABAQUS with a randomly distributed heterogeneous modulus of elasticity. Several parallel calculations are performed in Matlab. For certain randomly generated input parameters, Matlab produces meshes, creates inputs files, assemblies, and boundary conditions, and transfers the user-defined cell modulus map to the Fortran subroutine. The inputs files and assemblies are needed to form parts that record the total number of finite element for different layers, and define how different layers are connected, respectively. The Fortran subroutine is an interface for ABAQUS which allows the program to be customized for particular applications, such as varying the Modulus in our case. Given the input files and input from Fortran subroutine, Abaqus Kernel is performed. The results in the Abaqus output file (ODB file) are read using Python script and are presented in the manuscript.

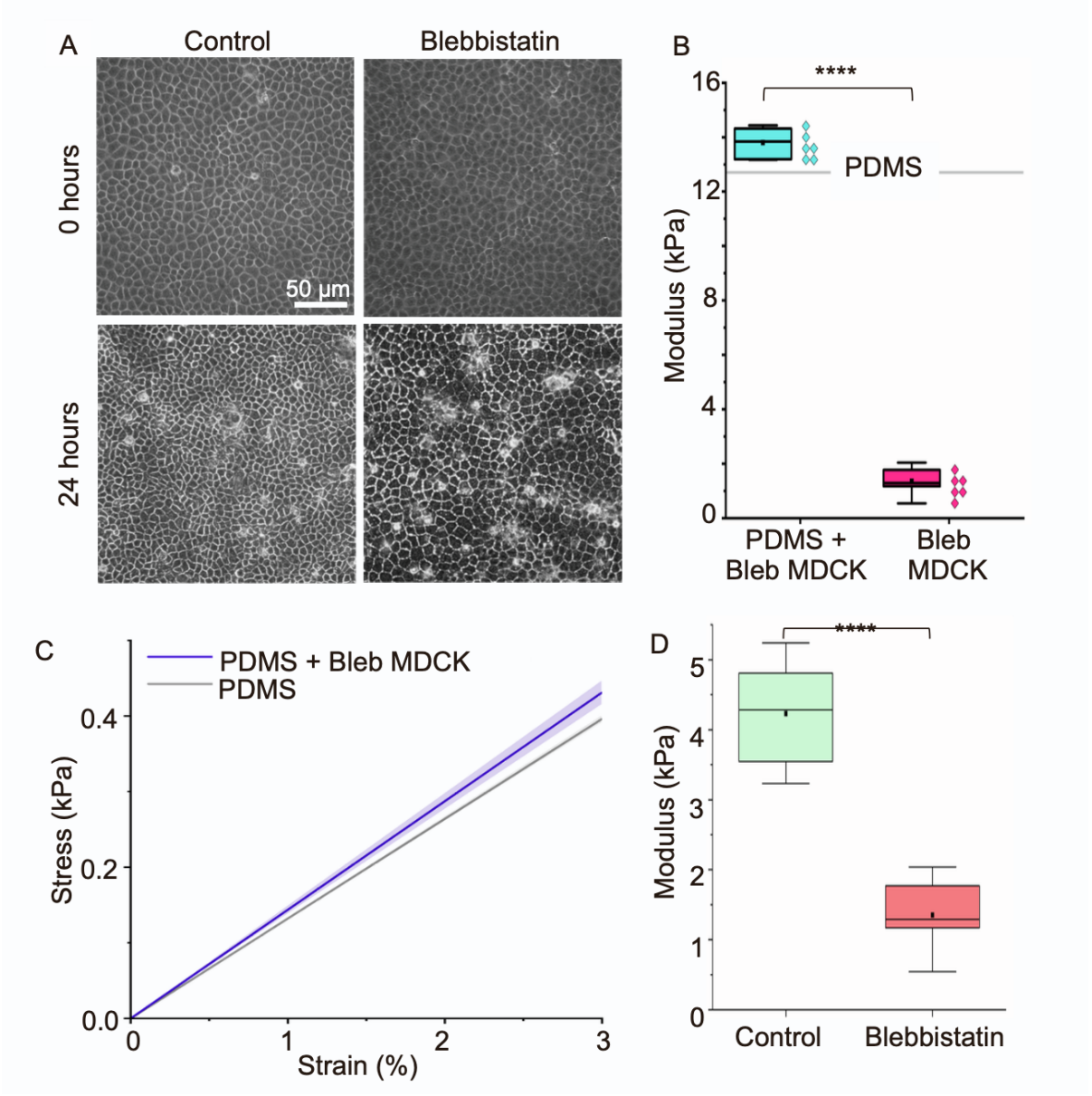

Figure 6.4: Blebbistatin treated MDCK cells demonstrate a 3-fold lower mean modulus compared to control MDCK cells.
MDCK cells were grown to confluence before being treated with 25 μm blebbistatin for 24 hours. (A) Comparison of untreated MDCK cells in DMEM (control) to blebbistatin treated cells (blebbistatin) between 0 to 24 hours. (B) Using the Hookean model illustrated in Fig. 2.1A, blebbistatin treated MDCK cell (Bleb MDCK) stiffness (1.4 $\pm$ 0.5 kPa) was estimated using equation (1). (C) Stress-strain curve for blebbistatin treated MDCK cells-PDMS bilayer (PDMS + Bleb MDCK) and PDMS samples. Shaded area denotes the standard deviation. (D) Comparison of control MDCK modulus to blebbistatin treated MDCK cells. Blebbistatin treated MDCK cells (1.4 $\pm$ 0.5 kPa) display a 3-fold decrease in modulus compared to MDCK control cells (4.2 $\pm$ 0.75 kPa). n=6

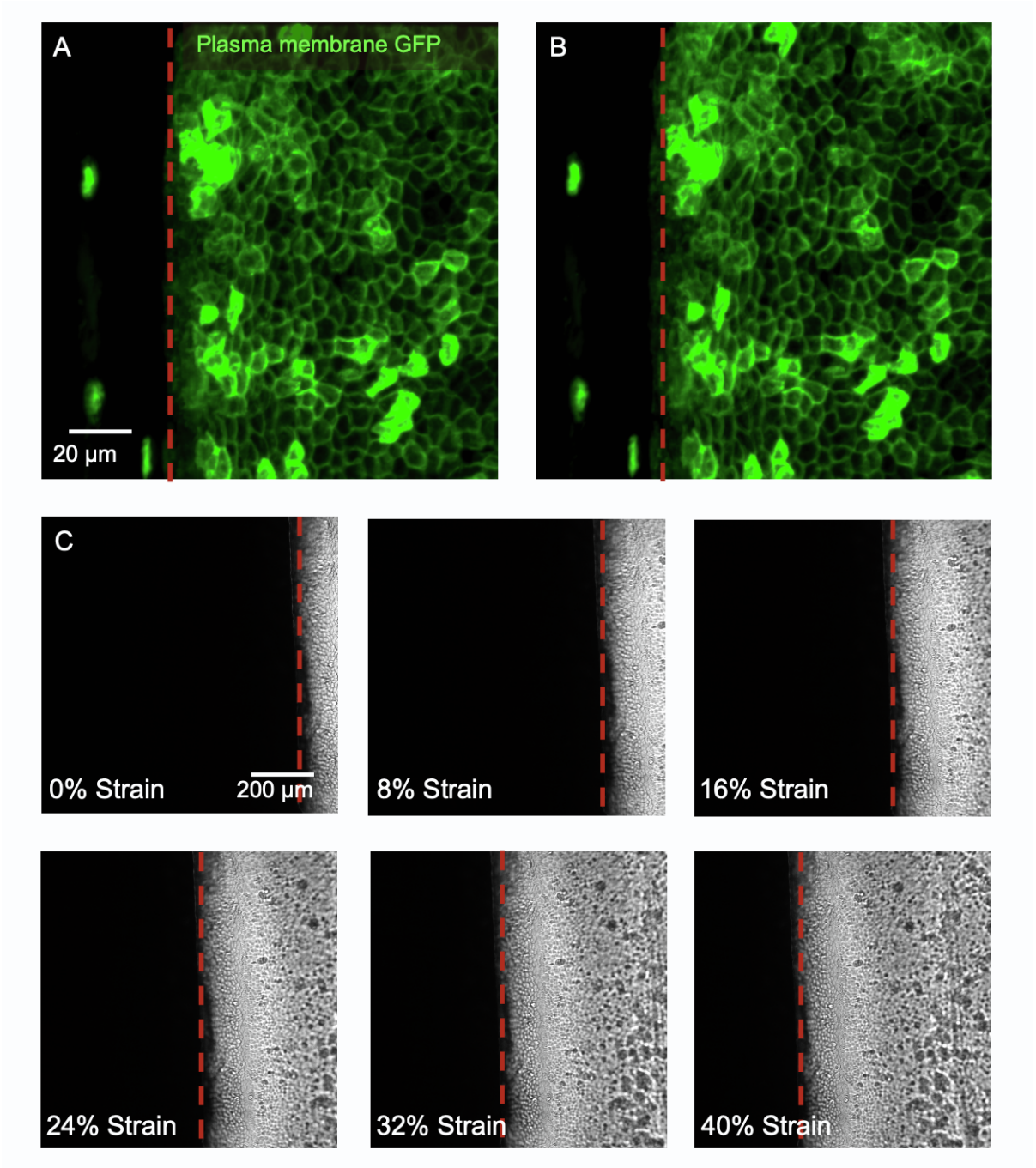

Figure 6.5: Non-slip boundary conditions are demonstrated at the cell-jig interface during stretching.
(A) Plasma membrane GFP (green) florescent image of unstretched MDCK cells cultured on PDMS substrate. Red dashed line denotes the cell-jig interface. (B) Same as (A) except with MDCK cells under 20% strain. Cells remain attached to both the substrate and jig under mechanical deformation. (C) DIC images of MDCK cells cultured on PDMS substrate under various applied strains. Red dashed line denotes the cell-jig interface.

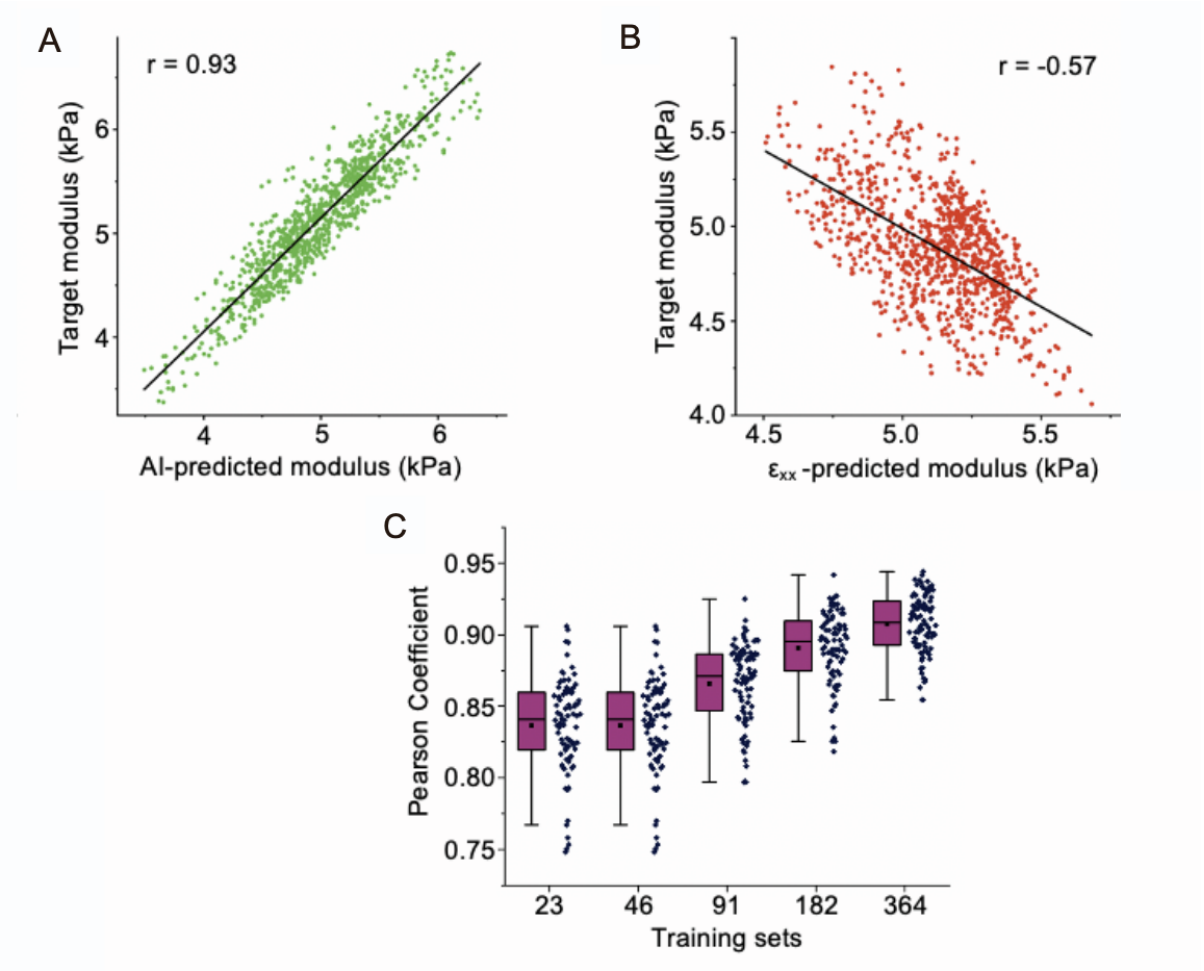

Figure 6.6: Modulus inference model characterization.
(A) Plot of ground truth modulus vs. AI predicted modulus. AI-predicted values and target modulus values yielded a Pearson correlation of 0.93, which is significantly greater than that produced by the $\epsilon_x x$ predicted modulus shown in (A). This increased accuracy relative to (A) further supports that using the three strain components to predict modulus, and thus using AI to identify the relationship between the three strain components, is necessary to yield more accurate results than $\epsilon_x x$ alone. (B) Scatter plot of ground truth modulus vs. $\epsilon_x x$ predicted modulus. $\epsilon_x x$ predicted modulus was obtained using the best fit between FEA simulated $\epsilon_x x$ values and modulus values. The resulting Pearson correlation coefficient of -0.57 between $\epsilon_x x$ values and target modulus values suggests that while $\epsilon_x x$ and modulus are strongly related, $\epsilon_x x$ alone is not sufficient for accurately predicting modulus. n = 1000 (C) Pearson correlation between AI predicted values and target modulus values as a function of increasing training sets. Pearson correlation coefficient increases with the number of training sets and achieves 93% accuracy with 364 sets of training data.

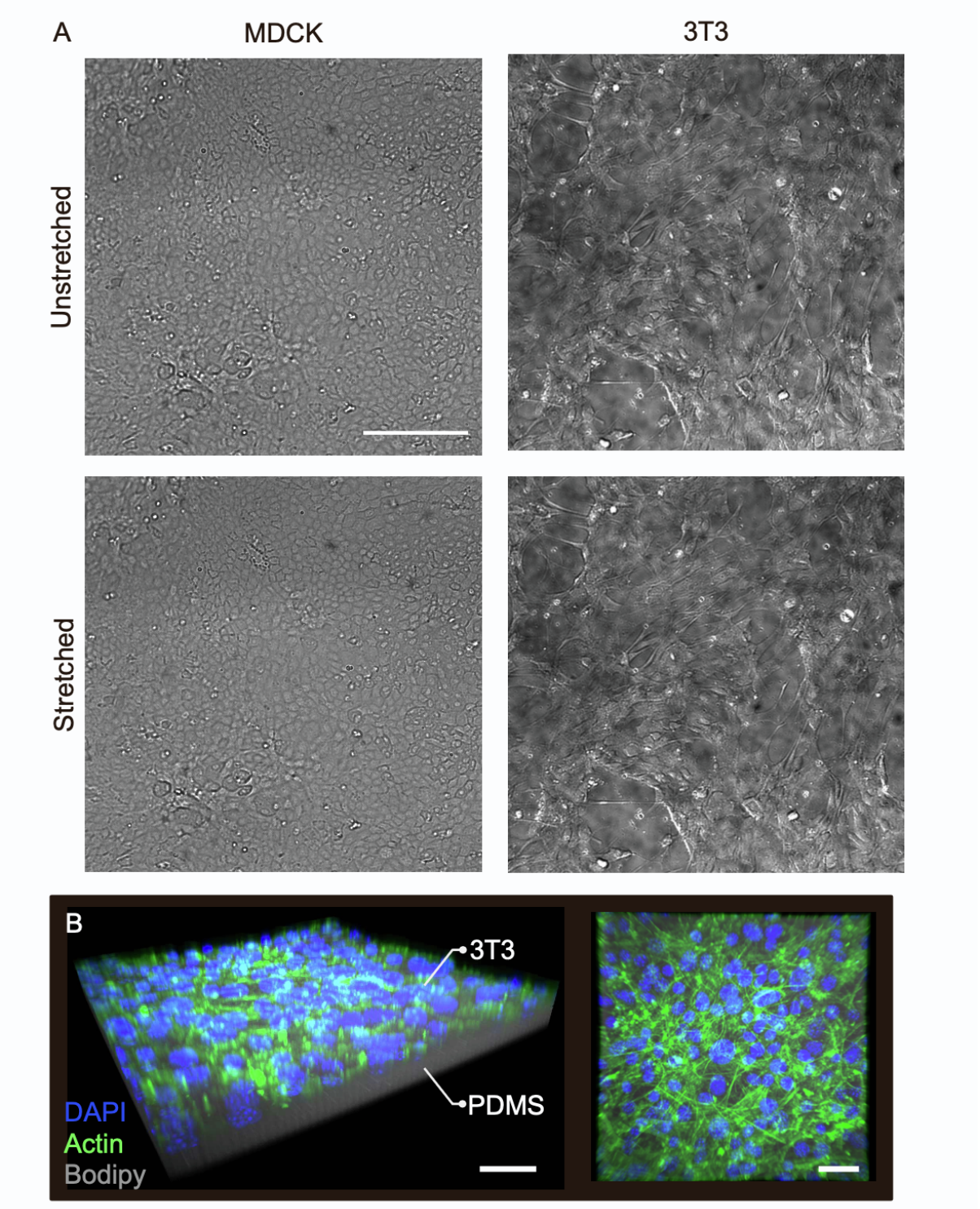

Figure 6.7: Stretched and unstretched images of MDCK and 3T3 cells used for modulus inference in Figs. 2.4A and 2.4D, respectively.
(A) MDCK (left) and 3T3 cells (right) used as PIV inputs to obtain modulus fields presented in Figs. 2.4A and 2.4D, respectively. Both MDCK and 3T3 cells are stretched to 5% strain. Scale bar is 200 μm. (B) 3D reconstruction of a 3T3 cell-PDMS bilayer tested in our experiment. Scale bars are 50 μm.

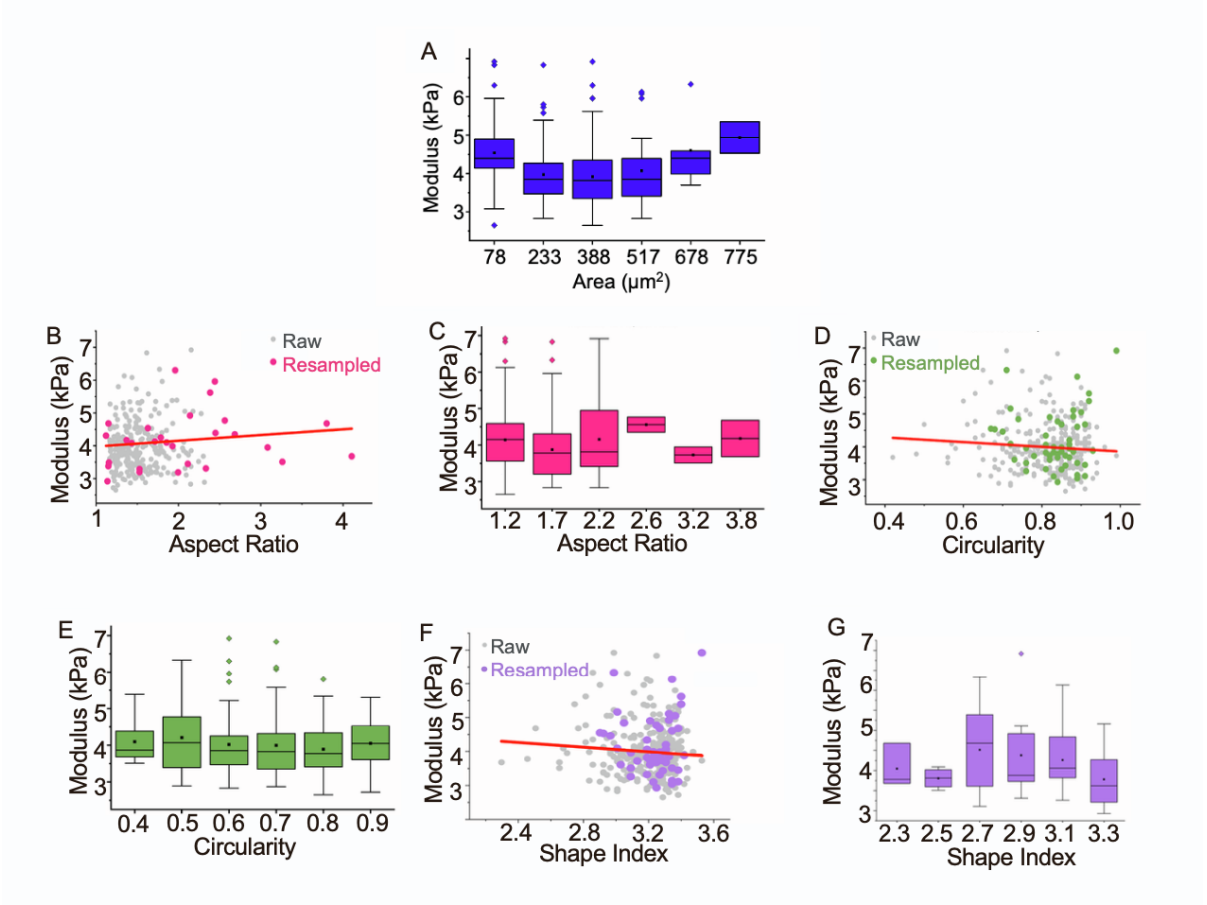

Figure 6.8: Modulus-morphology characterization.
(A) Box plot generated by binning all of the raw data points shown in Fig. 2.4H, confirming the observed effective modulus-area correlation for the large cells (area larger than 233 μm^2). (B) Modulus vs. aspect ratio measurements for individual cells. Fuchsia points denote a resampled dataset that has an even probability distribution across aspect ratio values. The fit for resampled data (red line) shows virtually no correlation between cell modulus and aspect ratio. (C) Box plot generated by binning all the raw data points in (B). Results further demonstrate a lack of modulus-aspect ratio correlation. (D) Modulus vs. circularity measurements for individual cells. Similar to (B), green points denote a resampled dataset that has an even probability distribution across circularity values. The fit for resampled data (red line) shows virtually no correlation between cell modulus and circularity. (E) Box plot generated by binning all the raw data points in (D). Results further demonstrate a lack of modulus-circularity correlation. (F) Modulus vs. shape index measurements for individual cells. Similar to (B), purple points denote a resampled dataset that has an even probability distribution across circularity values. The fit for resampled data (red line) shows virtually no correlation between cell modulus and circularity. (G) Box plot generated by binning all the raw data points in (F). Results further demonstrate a lack of modulus-shape index correlation. n=286

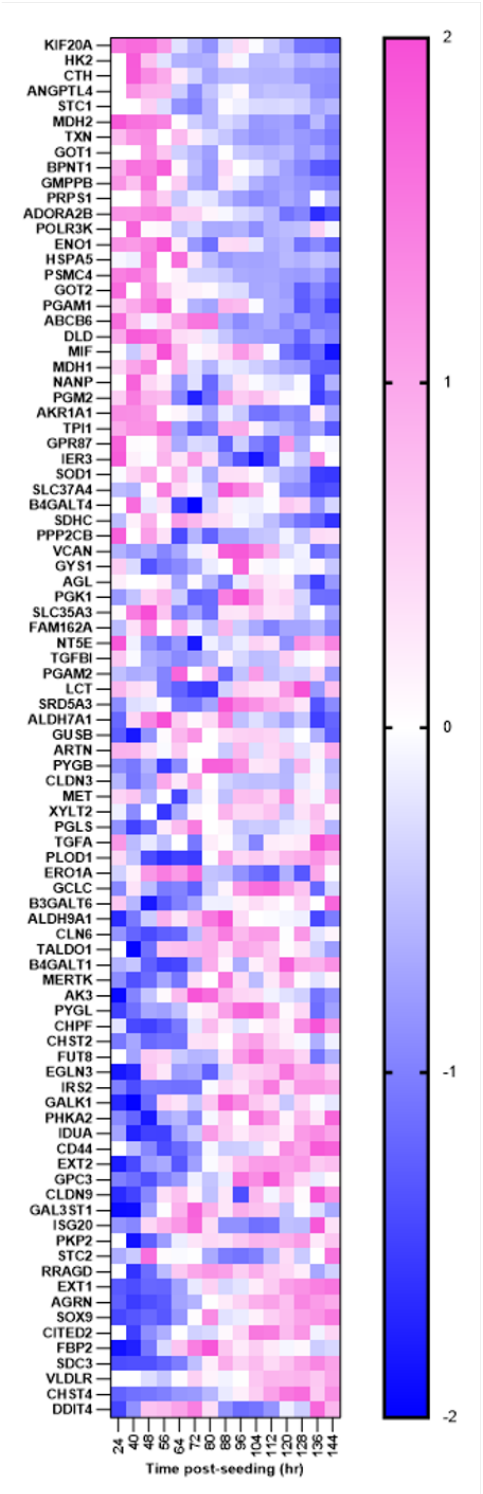

Figure 6.9: Heatmap of genes associated with glycolysis for each timepoint throughout jamming.

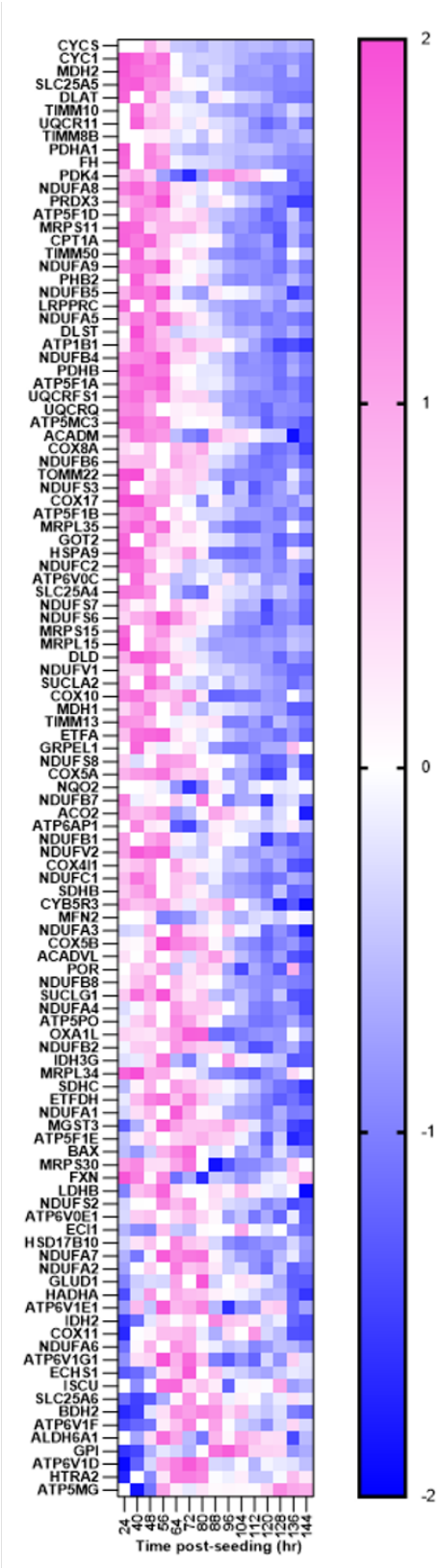

Figure 6.10: Heatmap of genes associated with oxidative phosphorylation for each timepoint throughout jamming.

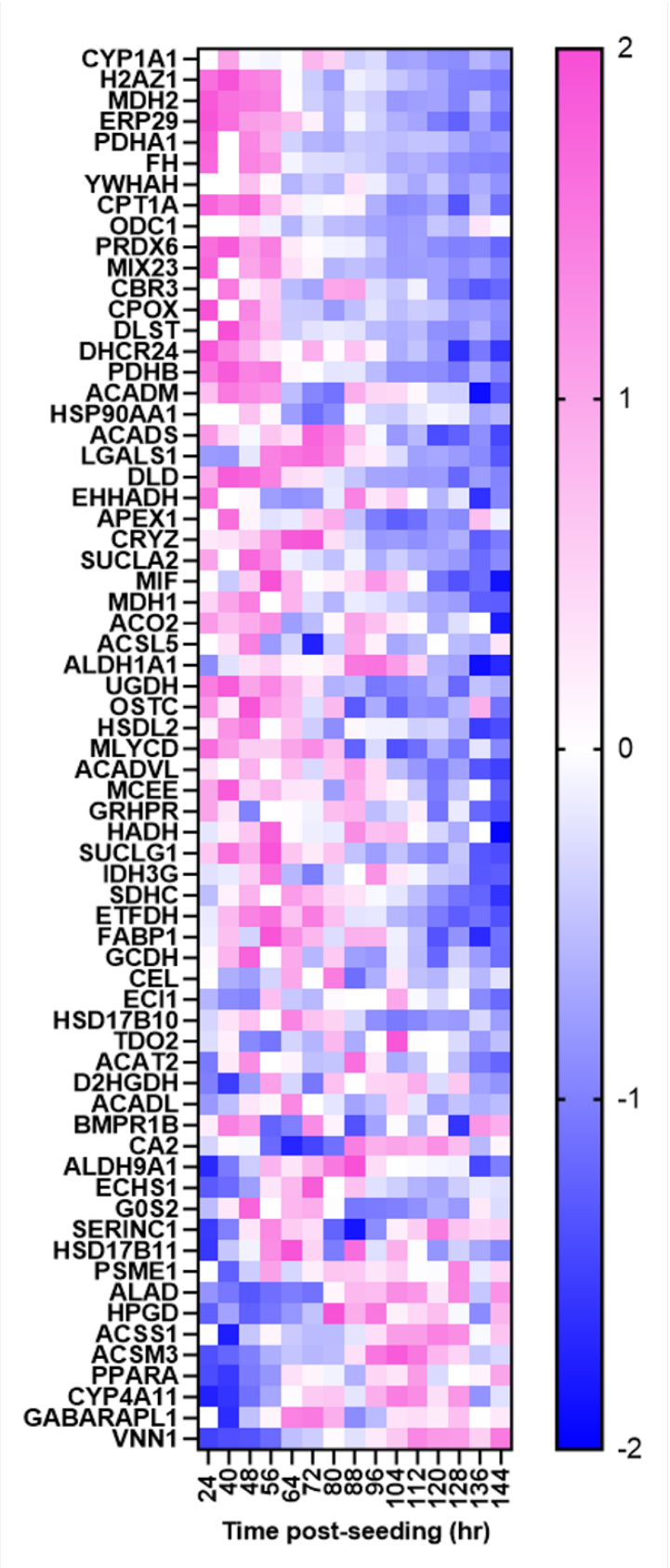

Figure 6.11: Heatmap of genes associated with fatty acid metabolism for each timepoint throughout jamming.

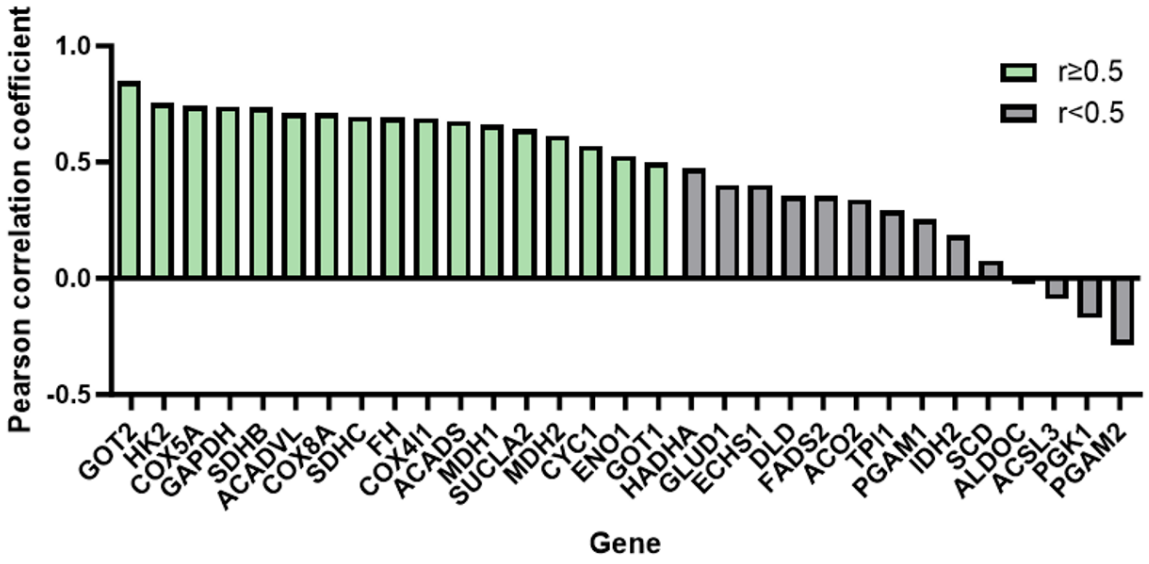

Figure 6.12: Bar chart of the Pearson correlation coefficients between the RNA expression and ATAC peak values for metabolic enzymes.
Pearson correlation coefficient was calculated using three replicates for each timepoint.

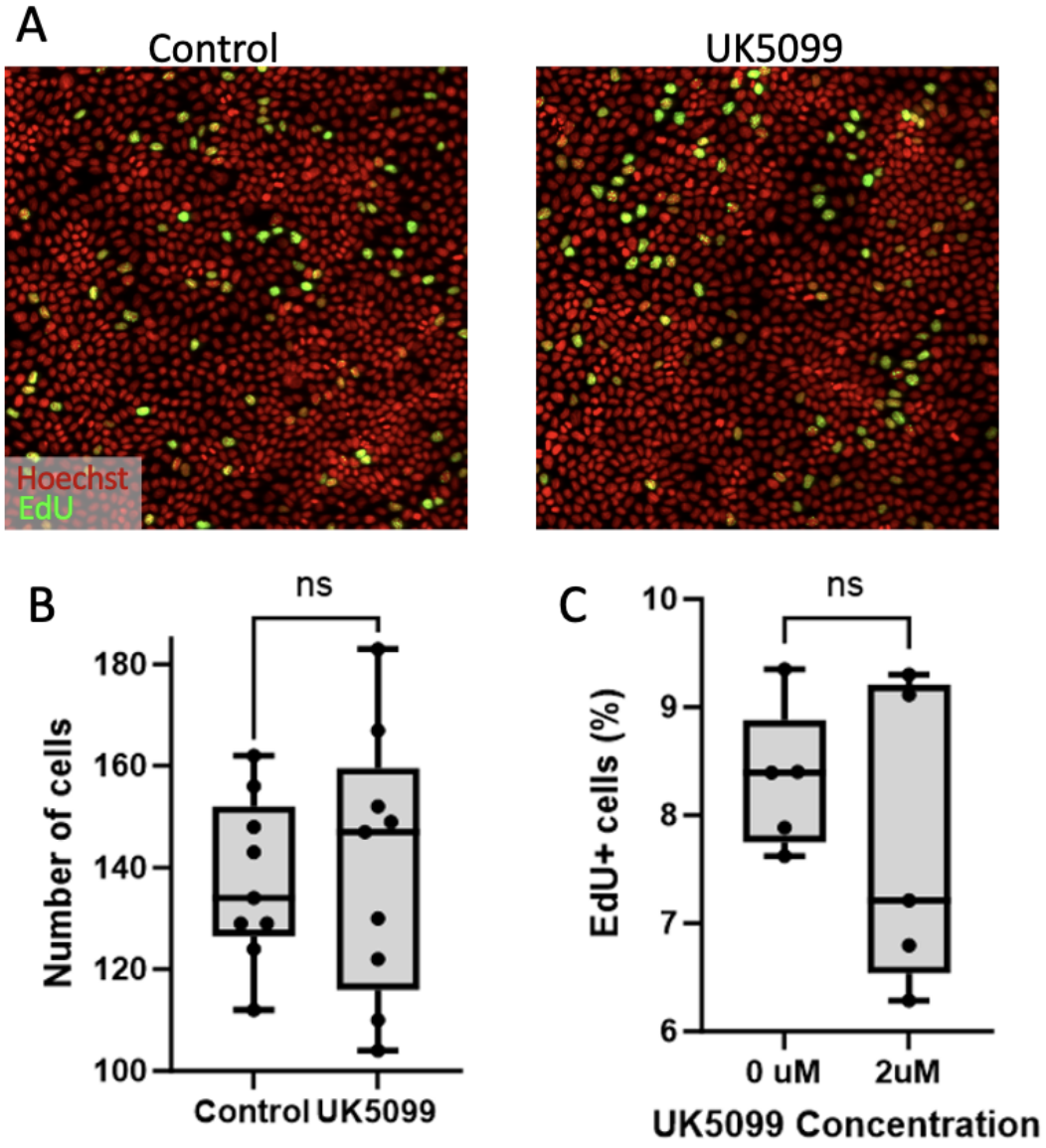

Figure 6.13: UK5099 treatment does not impact cell number or proliferation. (A) Images of control and UK5099 treated 144 hours after seeding. Cells were stained with Hoechst (red) and EdU (green). (B) No significant differences in cell number were detected due to UK5099 treatment. (C) No significant differences in proliferation were detected due to UK5099 treatment.

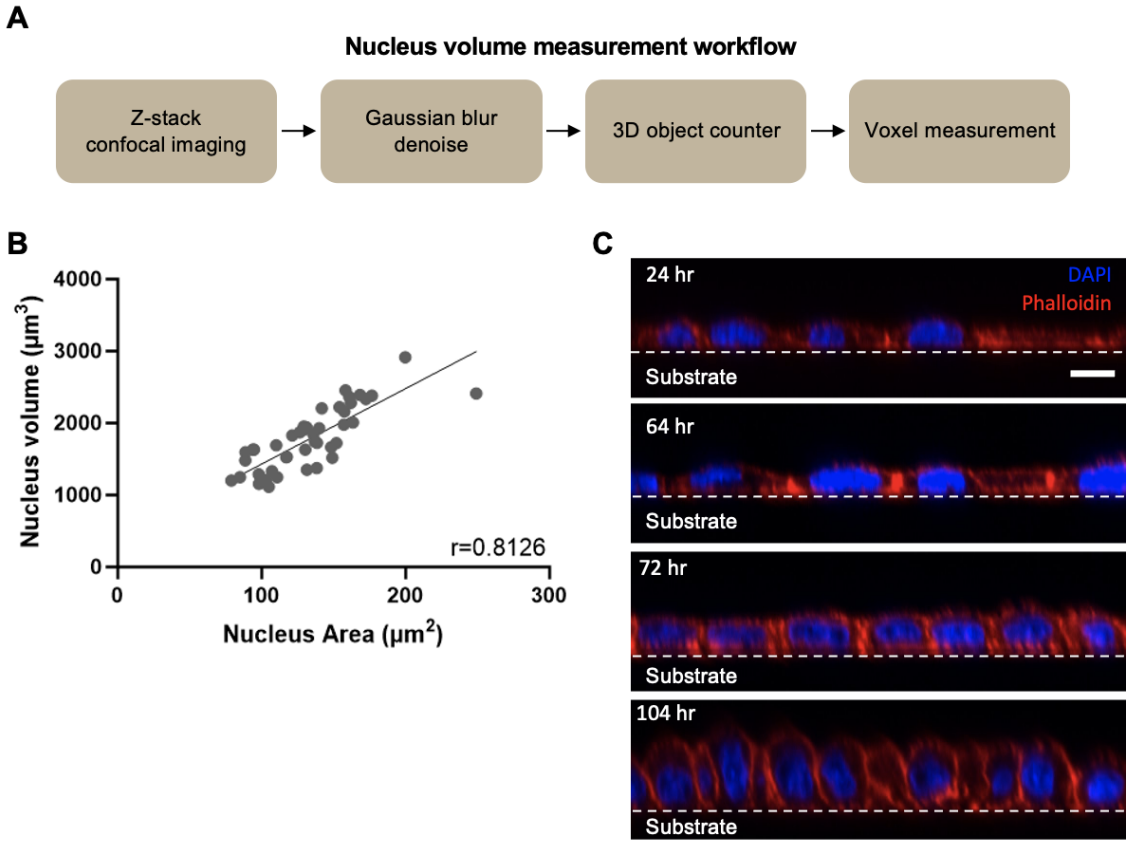

Figure 6.14: Area can be used to approximate volume in MDCK cells. (A) Analysis pipeline overview for volume measurement acquisition. First, z-stack imaging is performed using a fine 0.6 µm step size. Next, the image stack is imported into ImageJ and duplicated. A 3D Gaussian blur is then applied the duplicate stack using $\sigma_{x,y,z}$=2. This blurred duplicate is then used to set the masking threshold using the 3D objects counter analysis feature. Measurements are performed on the unfiltered z-stack. After the 3D objects counter analysis is performed, the 3D voxel measurement is output for each nucleus. (B) High correlation between nucleus volume and nucleus area in confluent MDCK cells suggests that area can be used in place of volume to characterize cell morphological behavior. (C) Orthogonal view of MDCK cells throughout crowding illustrating sample flatness. Time stamp refers to time post seeding at 30k cells/cm^2. Scale bar 10 μm.

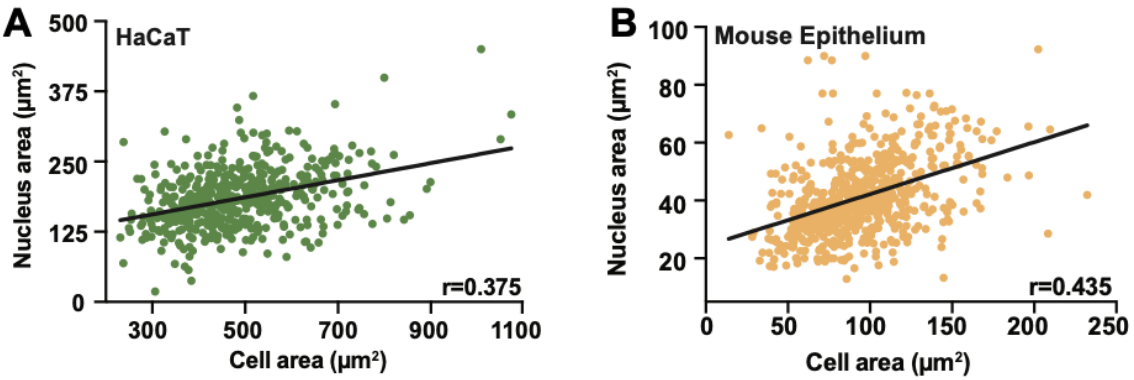

Figure 6.15: Nucleus-to-cell (NC) area correlations are demonstrated in HaCaT and mouse epithelium, akin to MDCK results.
NC area correlation exhibited in (A) confluent HaCaT cells and (B) E12.5 mouse arm epithelium.

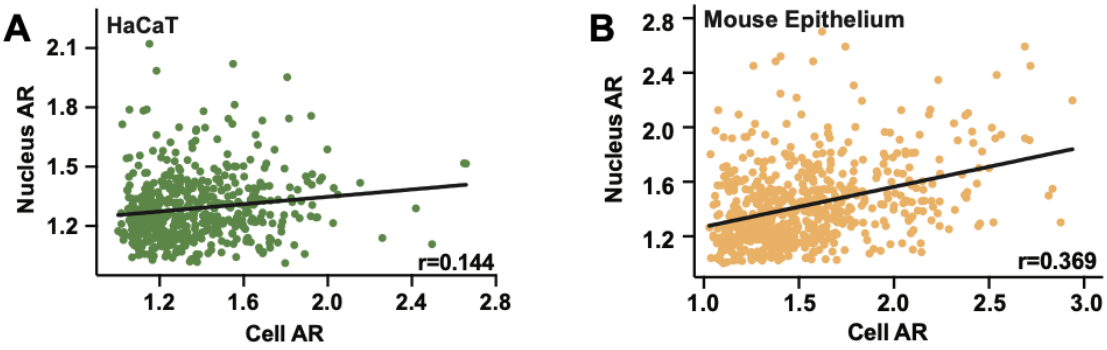

Figure 6.16: Nucleus-to-cell (NC) aspect ratio (AR) correlations are demonstrated in HaCaT and mouse epithelium, akin to MDCK results.
NC AR correlation exhibited in (A) confluent HaCaT cells and (B) E12.5 mouse arm epithelium.

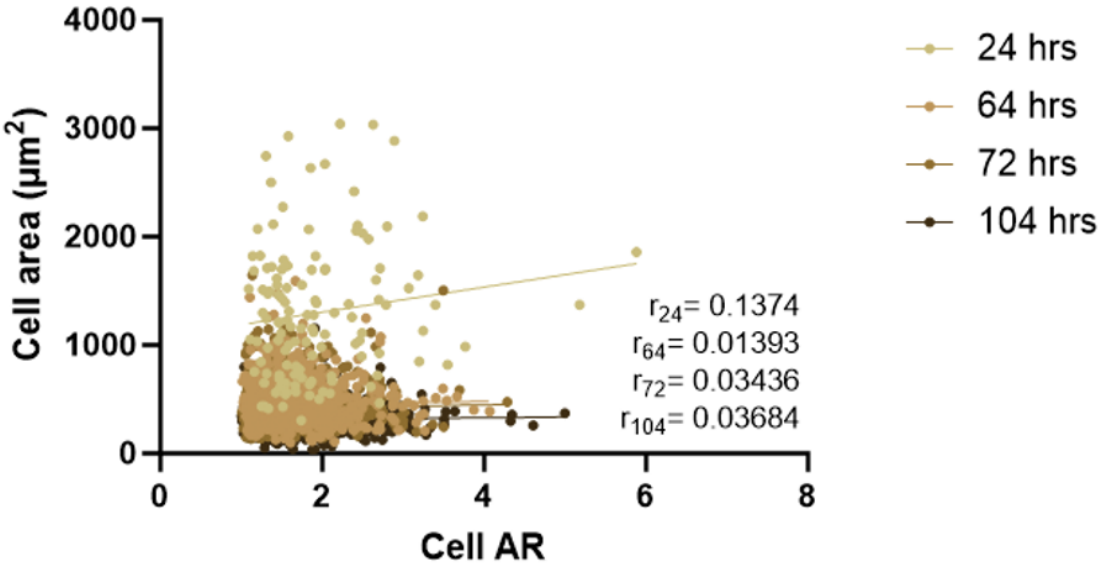

Figure 6.17: Cell area correlation with cell aspect ratio (AR) in MDCK cells. Negligible correlation between cell area and AR is observed at all investigated time points, suggesting that these two morphological features are independent and regulated by distinctive mechanisms.

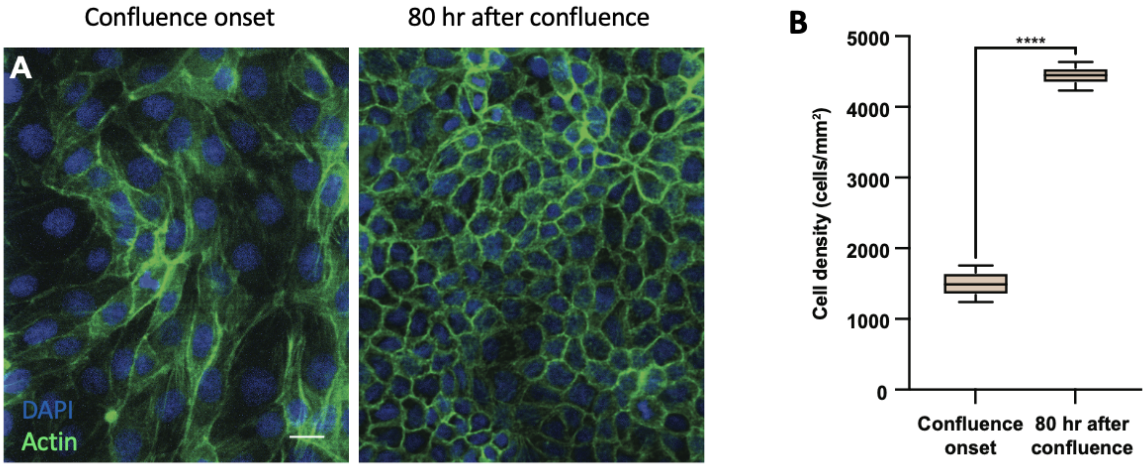

Figure 6.18: Cell division is required to induce cell crowding, and thus required for cell size reduction during crowding.
(A) Confluent MDCK monolayer (left) has less cells and larger cells compared to a crowded monolayer (right). Scale bar 20 µm. (B) Cell density approximately triples 80 hours after reaching confluence, suggesting that cell division and cell area reduction can be coupled.

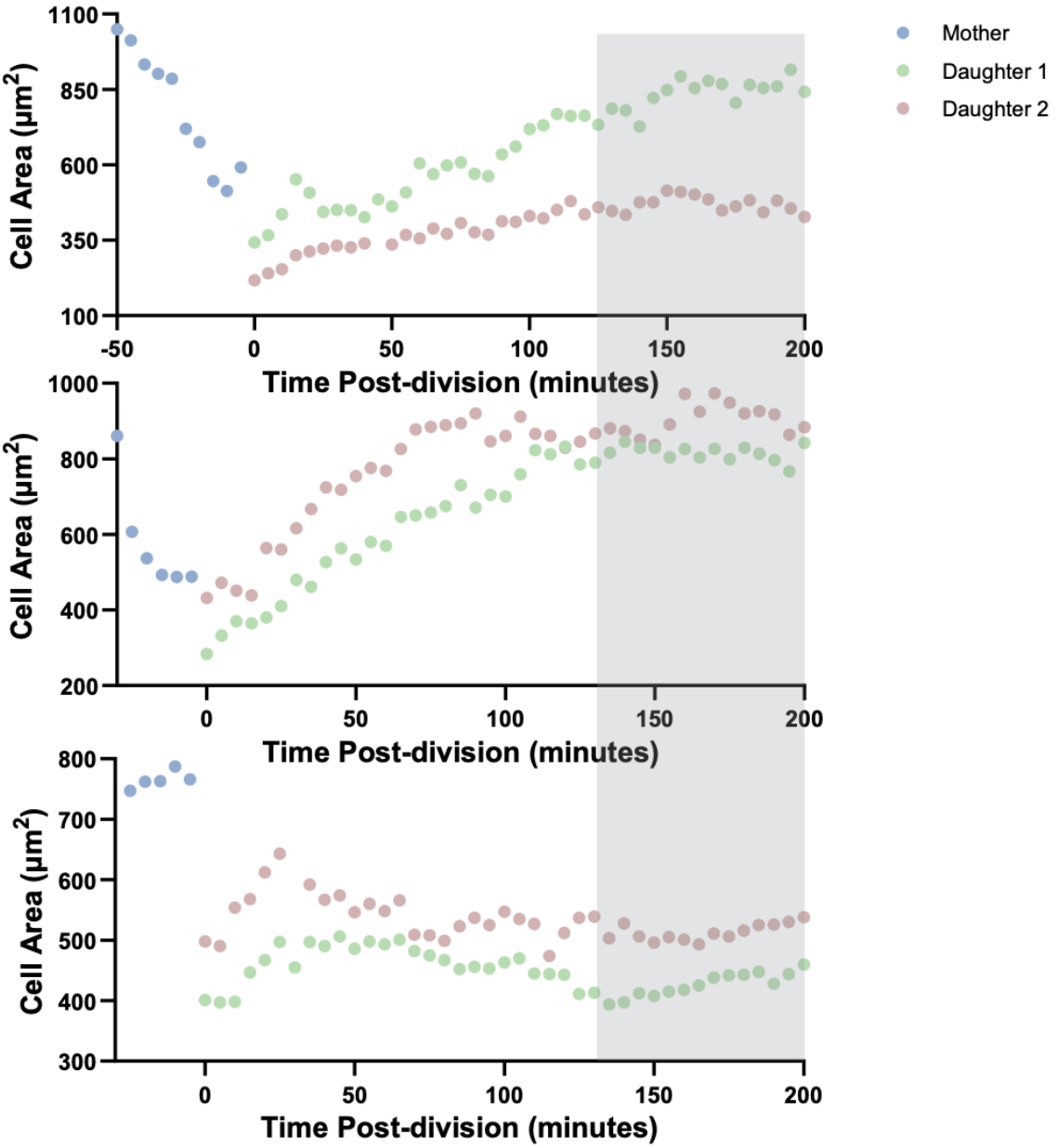

Figure 6.19: Cell growth rate plateaus approximately 2 hours post division. Three representative examples of cell growth trajectories illustrate that the cell growth phase lasts approximately 2 hours after division for most of the analyzed cell pairs. Gray shaded band indicates growth plateau regime.

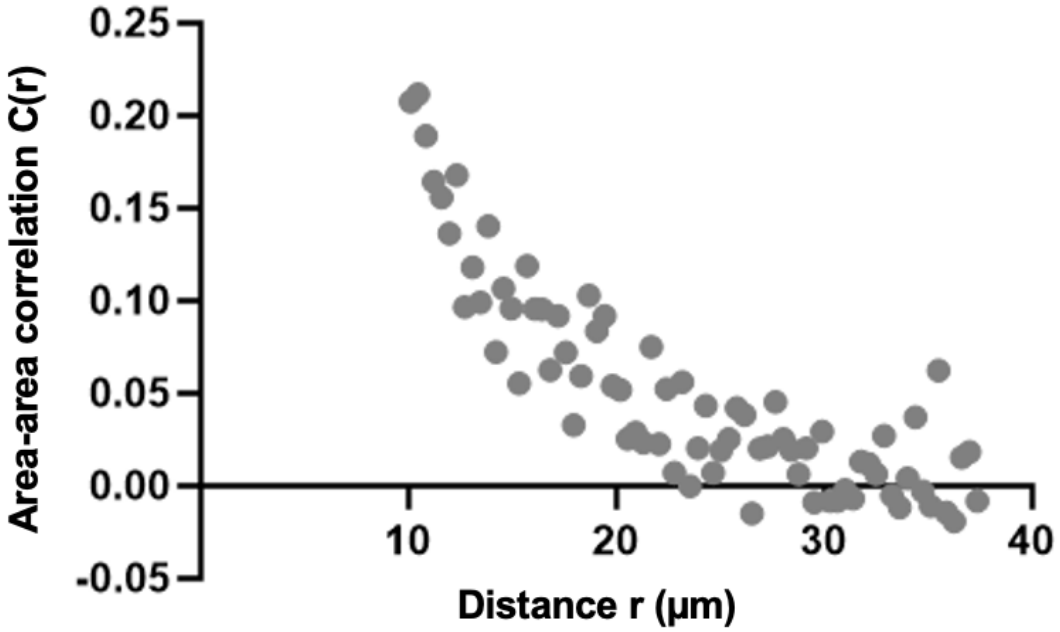

Figure 6.20: Area-area autocorrelation function of crowded MDCK cells reveals essentially no correlation between neighboring cells.
For distances greater than the diameter of a crowded MDCK cell (10-15 µm), no significant correlation is observed, suggesting that there is no genetic memory or inheritance of final cell size. The correlation $C(r)$ is calculated using $C(r) = \Sigma_{i,j} \frac{(A(r_i)-\langle A \rangle)(A(r_j)-\langle A \rangle)}{\langle A^2 \rangle - \langle A \rangle^2}$, where i, r, A and $\langle X \rangle$ denote the cell index, distance, area, and arithmetic mean, respectively.

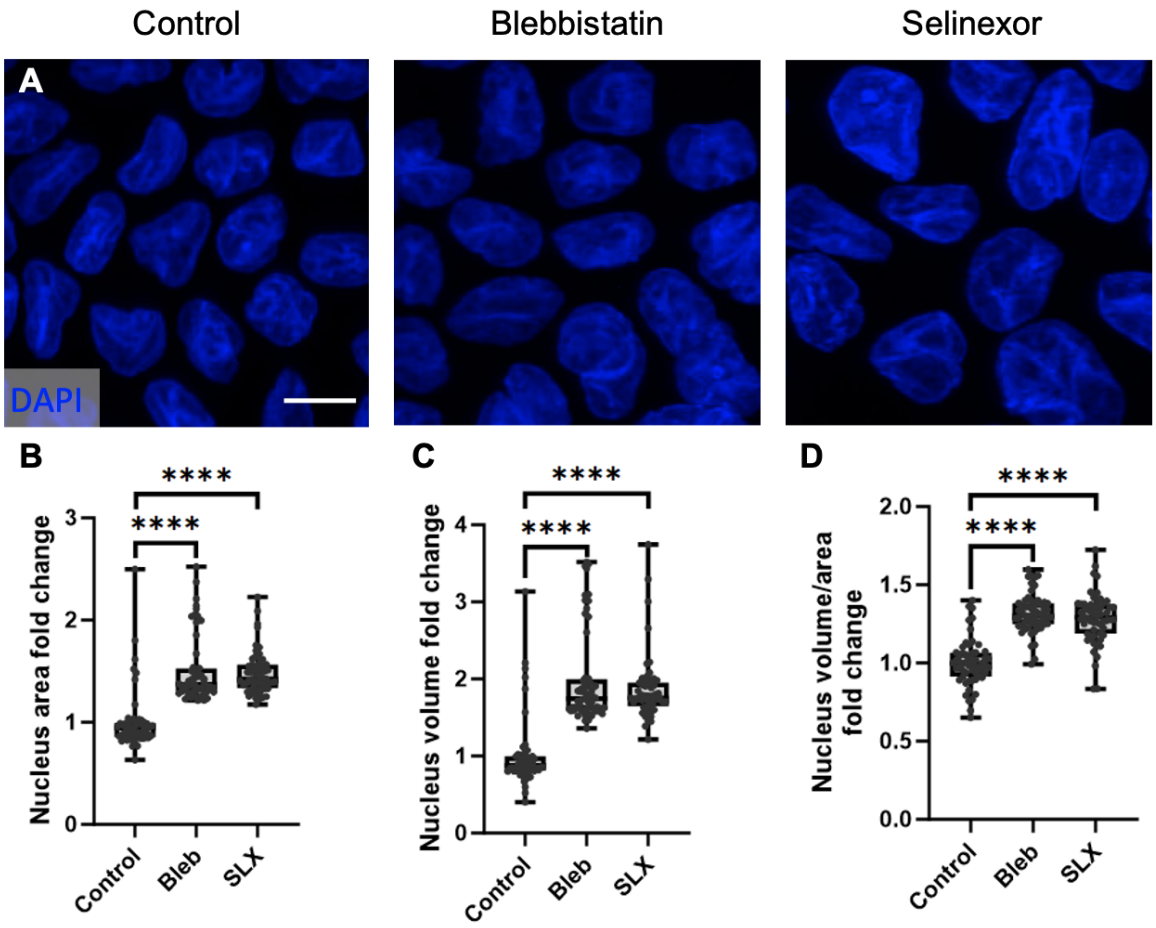

Figure 6.21: Nucleus volume increases in response to blebbistatin (bleb) and Selinexor (SLX) treatments.

(A) 3D projected confocal immunofluorescence images of untreated, bleb, and SLX treated nuclei, illustrating size differences. Scale bar 10 µm. (B) Nucleus area quantification demonstrates a 1.4 fold increase in nucleus area in treated groups. (C) Such a size increase is also reflected in nucleus volume, which was measured using the Imaris volume measurement function. Specifically, we found that bleb- and SLX-treated cells exhibit a 1.75 fold increase in nucleus volume. (D) Nucleus volume/area is used to estimate nucleus height, in which a slight (1.25 fold) increase was observed in both treated groups. Treatment concentration was 10 µM for both bleb and SLX.

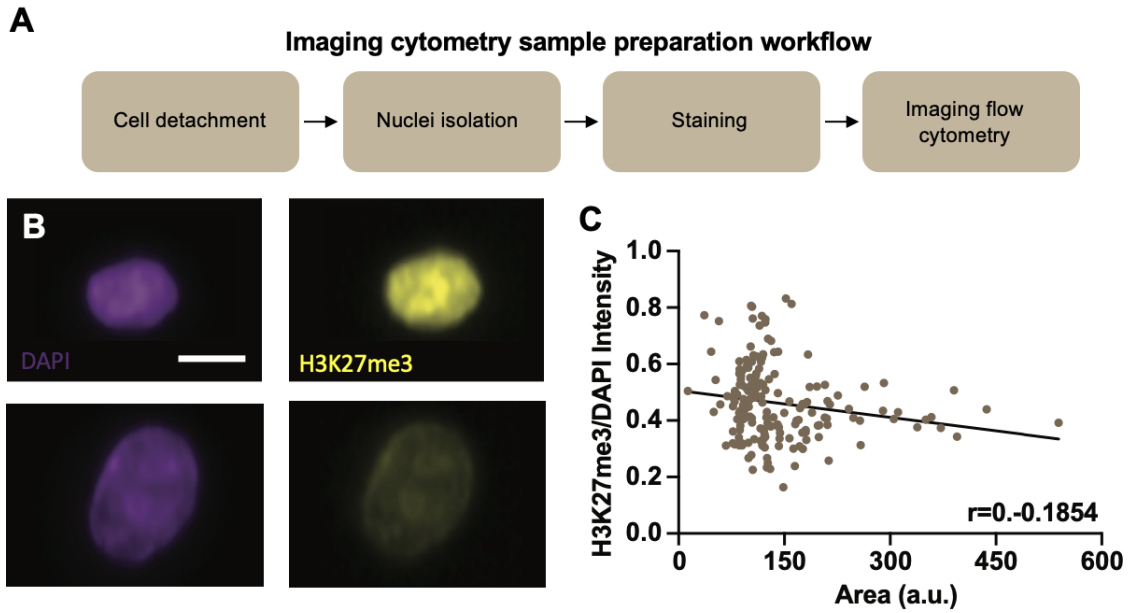

Figure 6.22: Anti-correlation between histone mark correlation with nucleus area in MDCK cells analyzed using imaging flow cytometry (Image Stream). (A) Experiment schematic for preparing samples for imaging flow cytometry analysis. First, cells were detached from the substrate using trypsin before being pelleted by centrifugation. The supernatant was aspirated, and cells were resuspended in a cell lysis buffer containing 0.1% NP40, 0.01% digitonin, and 0.1% Tween20. After a 5-minute incubation on ice, the lysis buffer was quenched using a resuspension buffer containing ultra pure water, 1M Tris0HCL, 5M NaCl, 1M MgCl2, and 0.1% Tween20. Resulting nuclei were then centrifuged to remove supernatant and resuspended in formalin for 10 minutes to perform fixation. Nuclei were then centrifuged to remove the formalin and washed twice using PBS and centrifugation. After the last wash, nuclei were stained for DAPI and H3K27me3 as described in the Materials and Methods section. These samples were then used for imaging flow cytometry analysis. (B) Representative images from imaging flow cytometry analysis demonstrating small and large nuclei express more and less H3K27me3, respectively. (C) Analysis of imaging flow cytometry data quantifying anti-correlation between normalized H3K27me3 intensity and nucleus size.

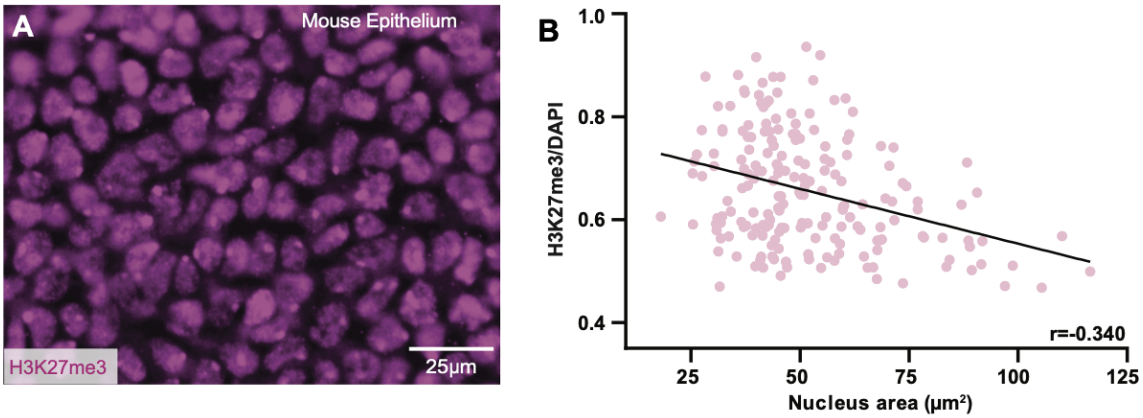

Figure 6.23: H3K27me3 intensity analysis in E11.5 mouse epithelium demonstrates that H3K27me3 is anti-correlated with nucleus size, in agreement with the MDCK result and other mouse epithelium results at E12.
(A) Representative image of mouse arm epithelium stained with H3K27me3. (B) Anti-correlation between normalized H3K27me3 intensity and nucleus size.

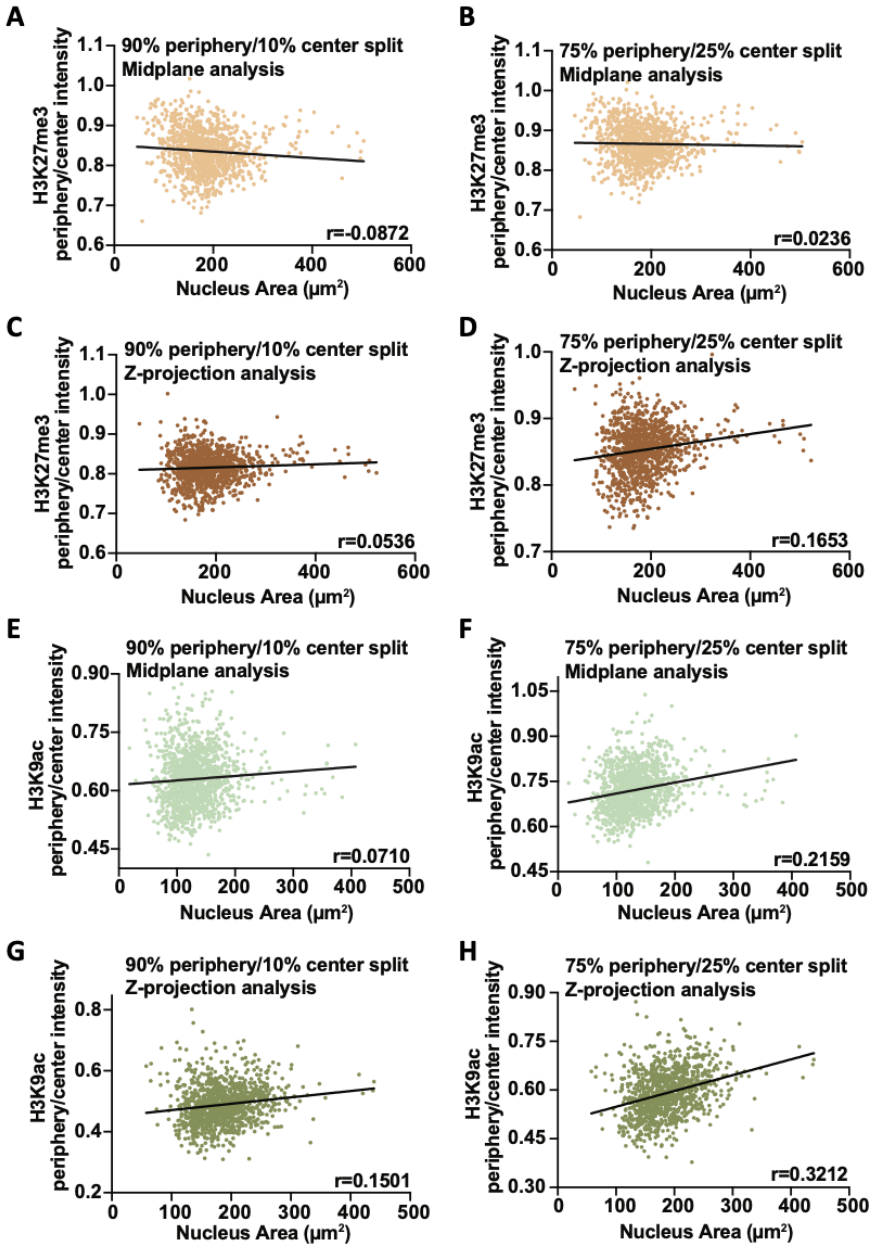

Figure 6.24: H3K27me3 and H3K9ac spatial distribution analysis in MDCK cells.

(A) H3K27me3 localization within the nucleus was examined using a single midplane image using a split ratio in which either the inner 90% of the nucleus was considered the center and the outer 10% was considered the periphery or (B) the inner 75% of the nucleus was considered the center and the outer 25% was considered the periphery. (C) Same analysis as (A) using a maximal z-projection instead of a single midplane slice. (D) Same analysis as (B) using a maximal z-projection instead of a single midplane slice. (E-F) Same analysis as A-D, respectively, investigating H3K9ac instead of H3K27me3.

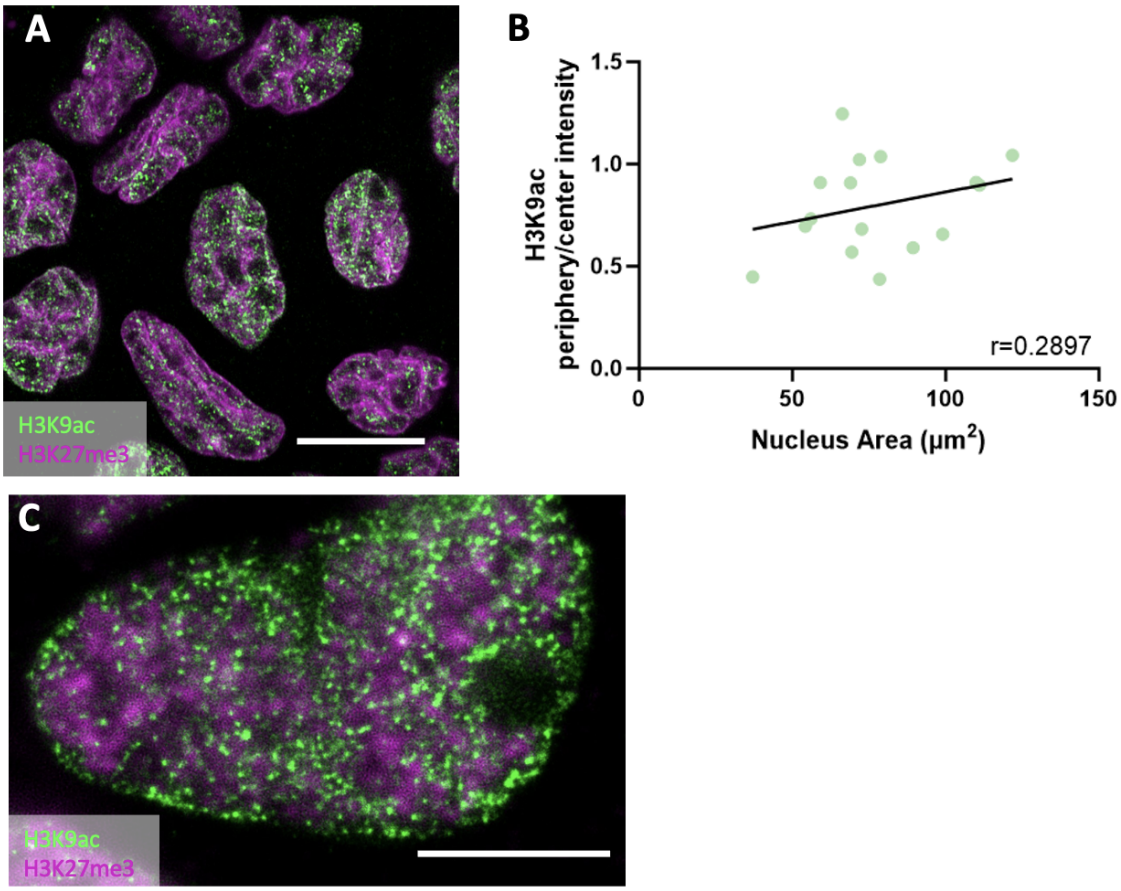

Figure 6.25: Super-resolution analysis of H3K27me3 and H3K9ac in crowded MDCK cells reproduces correlation between H3K9ac localization and nucleus area obtained from confocal microscopy.
(A) Airyscan images of MDCK nuclei illustrates distinct localization of active H3K9ac mark and repressive H3K27me3 mark. H3K9ac is localized as puncta within the nuclei while H3K27me3 localized around nuclear folds and edges. Scale bar 10 µm. (B) Radial analysis of H3K9ac using airyscan images. A positive correlation between H3K9ac periphery/center intensity and nucleus area reproduces confocal result shown in figure 4. FDR = 0.13. (C) STED image of H3K27me3 and H3K9ac stained nucleus demonstrates histone mark localization consistent with airyscan and confocal results. Scale bar is 5 µm.

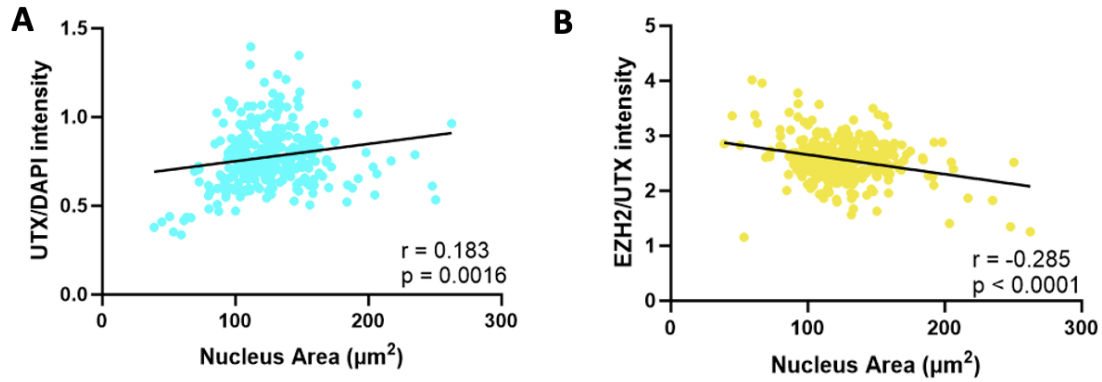

Figure 6.26: Histone demethylation UTX is correlated with nucleus size.
(A) UTX/DAPI intensity is positive correlated with Nucleus size. (B) EZH2/UTX intensity is anti-correlated with nucleus size.

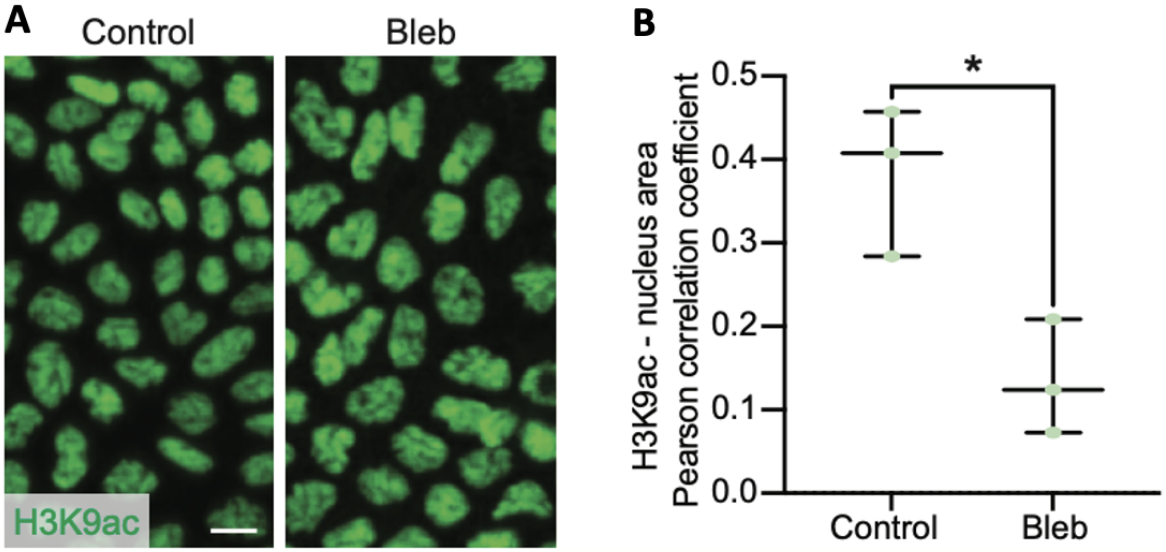

Figure 6.27: Myosin II is required for maintaining the positive correlation between nucleus area and H3K9ac level.
(A) Image of control (left) and Bleb-treated (right) MDCK cells stained with H3K9ac. Scale bar = 10 μm. (B) Pearson correlation coefficient between H3K9ac/DAPI intensity and nucleus area for control and Bleb-treated cells.

Figure	Pearson Correlation	Spearman Correlation	p-value	FDR	95% Confidence Interval
Fig. 1D MDCK nucleus area vs. cell area (24 hr)	0.6365	0.766	<0.0001	$<10^{-5}$	[0.518, 0.731]
Fig. 1D MDCK nucleus area vs. cell area (64 hr)	0.8326	0.838	<0.0001	$<10^{-5}$	[0.810, 0.853]
Fig. 1D MDCK nucleus area vs. cell area (24 hr)	0.7980	0.7506	<0.0001	$<10^{-5}$	[0.771, 0.822]
Fig. 1D MDCK nucleus area vs. cell area (104 hr)	0.7007	0.7066	<0.0001	$<10^{-5}$	[0.668, 0.731]
Fig. 1H MDCK nucleus AR vs. cell AR (24 hr)	0.3031	0.2359	<0.0001	$<10^{-5}$	[0.134, 0.455]
Fig. 1H MDCK nucleus AR vs. cell AR (64 hr)	0.4244	0.4047	<0.0001	$<10^{-5}$	[0.366, 0.479]
Fig. 1H MDCK nucleus AR vs. cell AR (24 hr)	0.4455	0.3858	<0.0001	$<10^{-5}$	[0.388, 0.499]
Fig. 1H MDCK nucleus AR vs. cell AR (104 hr)	0.5749	0.5272	0.0075	$<10^{-5}$	[0.533, 0.614]
Fig. 2D Cell area 6 hr vs. cell area 0 hr	0.568	0.6087	<0.0001	$<10^{-5}$	[0.431, 0.679]
Fig. 2E Nucleus area 6 hr vs. nucleus area 0 hr	0.586	0.5711	<0.0001	$<10^{-5}$	[0.452, 0.694]
Fig. 2H Nucleus area vs. cell area (0 hr)	0.727	0.6985	<0.0001	$<10^{-5}$	[0.628, 0.803]
Fig. 2I Nucleus area vs. cell area (6 hr)	0.811	0.8444	<0.0001	$<10^{-5}$	[0.738, 0.865]
Fig. 4B MDCK H3K27me3/DAPI vs. nucleus area	-0.326	-0.3280	<0.0001	$<10^{-5}$	[-0.447, -0.194]
Fig. 4D Mouse ectoderm H3K27me3/DAPI vs. nucleus area	-0.340	-30.19	<0.0001	$<10^{-5}$	[-0.459, -0.209]
Fig. 4F MDCK H3K9ac/DAPI vs. nucleus area	0.239	0.2969	<0.0001	$<10^{-5}$	[0.183, 0.293]
Fig. 4H Mouse ectoderm H3K9ac/DAPI vs. nucleus area	0.171	0.1674	<0.0001	$<10^{-5}$	[0.0988, 0.241]
Fig. 4K Mouse ectoderm H3K9ac P/C intensity vs. nucleus area	0.185	0.1234	<0.0001	$<10^{-5}$	[0.131, 0.238]

Figure 6.28: Summary of correlative analyses.
To quantify correlation, both the Pearson (column 2) and Spearman (column 3) correlation coefficient were measured. To quantify statistical significance the p-value (column 4), false discovery rate (FDR) (column 5), and 95% confidence interval (column 6) were computed.

Addae-Mensah, K. A., Reiserer, R. S., and Wikswo, J. P. (2007). Poly (vinyl alcohol) as a structure release layer for the microfabrication of polymer composite structures. *Journal of Micromechanics and Microengineering*, 17(7):N41. 25

Agger, K., Cloos, P. A., Christensen, J., Pasini, D., Rose, S., Rappsilber, J., Issaeva, I., Canaani, E., Salcini, A. E., and Helin, K. (2007). Utx and jmjd3 are histone h3k27 demethylases involved in hox gene regulation and development. *Nature*, 449(7163):731–734. 86

Albertson, R. and Doe, C. Q. (2003). Dlg, scrib and lgl regulate neuroblast cell size and mitotic spindle asymmetry. *Nature cell biology*, 5(2):166–170. 90

Alt, S., Ganguly, P., and Salbreux, G. (2017). Vertex models: from cell mechanics to tissue morphogenesis. *Philosophical Transactions of the Royal Society B: Biological Sciences*, 372(1720):20150520. 40

Amir, A. (2014). Cell size regulation in bacteria. *Physical review letters*, 112(20):208102. 81

Amoyel, M. and Bach, E. A. (2014). Cell competition: how to eliminate your neighbours. *Development*, 141(5):988–1000. 19

Andreu, I., Granero-Moya, I., Chahare, N. R., Clein, K., Molina-Jordán, M., Beedle, A. E., Elosegui-Artola, A., Abenza, J. F., Rossetti, L., Trepat, X., et al. (2022). Mechanical force application to the nucleus regulates nucleocytoplasmic transport. *Nature cell biology*, 24(6):896–905. 89

Angelini, T. E., Hannezo, E., Trepat, X., Marquez, M., Fredberg, J. J., and Weitz, D. A. (2011). Glass-like dynamics of collective cell migration. *Proceedings of the National Academy of Sciences*, 108(12):4714–4719. 5, 7, 88

Antico Arciuch, V. G., Elguero, M. E., Poderoso, J. J., and Carreras, M. C. (2012). Mitochondrial regulation of cell cycle and proliferation. *Antioxidants & redox signaling*, 16(10):1150–1180. 55

Atia, L., Bi, D., Sharma, Y., Mitchel, J. A., Gweon, B., A. Koehler, S., DeCamp, S. J., Lan, B., Kim, J. H., Hirsch, R., et al. (2018). Geometric constraints during epithelial jamming. *Nature physics*, 14(6):613–620. 3, 67, 77, 78, 81

Balaban, N. Q., Merrin, J., Chait, R., Kowalik, L., and Leibler, S. (2004). Bacterial persistence as a phenotypic switch. *Science*, 305(5690):1622–1625. 67

Bankhead, P., Loughrey, M. B., Fernández, J. A., Dombrowski, Y., McArt, D. G., Dunne, P. D., McQuaid, S., Gray, R. T., Murray, L. J., Coleman, H. G., et al. (2017). Qupath: Open source software for digital pathology image analysis. *Scientific reports*, 7(1):1–7. 74

Bar-Even, A., Paulsson, J., Maheshri, N., Carmi, M., O'Shea, E., Pilpel, Y., and Barkai, N. (2006). Noise in protein expression scales with natural protein abundance. *Nature genetics*, 38(6):636–643. 67

Bartalena, G., Grieder, R., Sharma, R. I., Zambelli, T., Muff, R., and Snedeker, J. G. (2011). A novel method for assessing adherent single-cell stiffness in tension: design and testing of a substrate-based live cell functional imaging device. *Biomedical microdevices*, 13(2):291–301. 24, 34

Behringer, R. P. and Chakraborty, B. (2018). The physics of jamming for granular materials: a review. *Reports on Progress in Physics*, 82(1):012601. 6

Bermudez, A., Gonzalez, Z., Zhao, B., Salter, E., Liu, X., Ma, L., Jawed, M. K., Hsieh, C.-J., and Lin, N. Y. (2022). Supracellular measurement of spatially varying mechanical heterogeneities in live monolayers. *Biophysical Journal*, 121(18):3358–3369. xi

Bermudez, A., Negrete Muñoz, S., Blaik, R., Rowat, A. C., Hu, J., and Lin, N. Y. (2023). Using histologic image analysis to understand biophysical regulations of epithelial cell morphology. *The Biophysicist*. xii

Bertero, M., Jost, R., et al. (1980). *Inverse scattering problems in optics*, volume 20. Springer Verlag. 29

Bhattacharya, D., Azambuja, A. P., and Simoes-Costa, M. (2020). Metabolic reprogramming promotes neural crest migration via yap/tead signaling. *Developmental cell*, 53(2):199–211. 40

Bi, D., Lopez, J., Schwarz, J. M., and Manning, M. L. (2015). A density-independent rigidity transition in biological tissues. *Nature Physics*, 11(12):1074–1079. 8, 13, 97

Bi, D., Lopez, J. H., Schwarz, J. M., and Manning, M. L. (2014). Energy barriers and cell migration in densely packed tissues. *Soft matter*, 10(12):1885–1890. 3

Bi, D., Yang, X., Marchetti, M. C., and Manning, M. L. (2016). Motility-driven glass and jamming transitions in biological tissues. *Physical Review X*, 6(2):021011. 8

Bi, D., Zhang, J., Chakraborty, B., and Behringer, R. P. (2011). Jamming by shear. *Nature*, 480(7377):355–358. 6

Blonski, S., Aureille, J., Badawi, S., Zaremba, D., Pernet, L., Grichine, A., Fraboulet, S., Korczyk, P. M., Recho, P., Guilluy, C., et al. (2021). Direction of epithelial folding defines impact of mechanical forces on epithelial state. *Developmental Cell*, 56(23):3222–3234. 68

Boulogne, F., Kong, Y. L., Nunes, J. K., and Stone, H. A. (2016). Effect of the polydispersity of a colloidal drop on drying induced stress as measured by the buckling of a floating sheet. *Physical review letters*, 116(23):238001. 25

Boulter, E., Tissot, F. S., Dilly, J., Pisano, S., and Féral, C. C. (2020). Cyclic uniaxial mechanical stretching of cells using a lego® parts-based mechanical stretcher system. *Journal of cell science*, 133(1):jcs234666. 34

Bowman, G. D. and Poirier, M. G. (2014). Post-translational modifications of histones that influence nucleosome dynamics. *Chemical reviews*, 115(6):2274–2295. 67

Brodland, G. W., Conte, V., Cranston, P. G., Veldhuis, J., Narasimhan, S., Hutson, M. S., Jacinto, A., Ulrich, F., Baum, B., and Miodownik, M. (2010). Video force microscopy reveals the mechanics of ventral furrow invagination in drosophila. *Proceedings of the National Academy of Sciences*, 107(51):22111–22116. 3

Burrows, M. T. (1912). Wound healing in vitro. *Proceedings of the New York. Pathol. Soc*, 13. 4

BUSCHKE, W. (1949). Morphologic changes in cells of corneal epithelium in wound healing. *Archives of Ophthalmology*, 41(3):306–316. 4

Cadart, C., Venkova, L., Piel, M., and Lagomarsino, M. C. (2022). Volume growth in animal cells is cell cycle dependent and shows additive fluctuations. *Elife*, 11:e70816. 81

Cadart, C., Venkova, L., Recho, P., Lagomarsino, M. C., and Piel, M. (2019). The physics of cell-size regulation across timescales. *Nature Physics*, 15(10):993–1004. 88

Cadart, C., Zlotek-Zlotkiewicz, E., Le Berre, M., Piel, M., and Matthews, H. K. (2014). Exploring the function of cell shape and size during mitosis. *Developmental cell*, 29(2):159–169. 88, 89

Cai, G., Nguyen, A., Bashirzadeh, Y., Lin, S.-S., Bi, D., and Liu, A. P. (2022). Compressive stress drives adhesion-dependent unjamming transitions in breast cancer cell migration. *Frontiers in Cell and Developmental Biology*, 10:933042. 8

Camilli, S., Lockey, R., and Kolliputi, N. (2023). Nuclear export inhibitors selinexor (kpt-330) and eltanexor (kpt-8602) provide a novel therapy to reduce tumor growth by induction of panoptosis. *Cell Biochemistry and Biophysics*, pages 1–6. 83

Charbonneau, P., Corwin, E. I., Parisi, G., and Zamponi, F. (2015). Jamming criticality revealed by removing localized buckling excitations. *Physical review letters*, 114(12):125504. 6

Chen, C.-L. and Chen, H.-C. (2009). Functional suppression of e-cadherin by protein kinase cδ. *Journal of cell science*, 122(4):513–523. 60

Chepizhko, O., Lionetti, M. C., Malinverno, C., Giampietro, C., Scita, G., Zapperi, S., and La Porta, C. A. (2018). From jamming to collective cell migration through a boundary induced transition. *Soft matter*, 14(19):3774–3782. 4

Chiang, M. Y., Yangben, Y., Lin, N. J., Zhong, J. L., and Yang, L. (2013). Relationships among cell morphology, intrinsic cell stiffness and cell–substrate interactions. *Biomaterials*, 34(38):9754–9762. 19, 33

Cho, K.-H., Choo, S.-M., Jung, S., Kim, J.-R., Choi, H.-S., and Kim, J. (2007). Reverse engineering of gene regulatory networks. *IET Systems Biology*, 1(3):149–163. 29

Choi, D., Gonzalez, Z., Ho, S. Y., Bermudez, A., and Lin, N. Y. (2022). Cell-cell adhesion impacts epithelia response to substrate stiffness: Morphology and gene expression. *Biophysical Journal*, 121(2):336–346. xi, 33

Christ, A. F., Franze, K., Gautier, H., Moshayedi, P., Fawcett, J., Franklin, R. J., Karadottir, R. T., and Guck, J. (2010). Mechanical difference between white and gray matter in the rat cerebellum measured by scanning force microscopy. *Journal of biomechanics*, 43(15):2986–2992. 19

Coghlin, C. and Murray, G. I. (2010). Current and emerging concepts in tumour metastasis. *The Journal of pathology*, 222(1):1–15. 40

Corces, M. R., Trevino, A. E., Hamilton, E. G., Greenside, P. G., Sinnott-Armstrong, N. A., Vesuna, S., Satpathy, A. T., Rubin, A. J., Montine, K. S., Wu, B., et al. (2017). An improved atac-seq protocol reduces background and enables interrogation of frozen tissues. *Nature methods*, 14(10):959–962. 42

Cox, T. R. and Erler, J. T. (2011). Remodeling and homeostasis of the extracellular matrix: implications for fibrotic diseases and cancer. *Disease models & mechanisms*, 4(2):165–178. 32

Crosetto, N. and Bienko, M. (2020). Radial organization in the mammalian nucleus. *Frontiers in genetics*, 11:33. 85

Cui, Y., Hameed, F. M., Yang, B., Lee, K., Pan, C. Q., Park, S., and Sheetz, M. (2015). Cyclic stretching of soft substrates induces spreading and growth. *Nature communications*, 6(1):1–8. 32

Czajkowski, M., Sussman, D. M., Marchetti, M. C., and Manning, M. L. (2019). Glassy dynamics in models of confluent tissue with mitosis and apoptosis. *Soft matter*, 15(44):9133–9149. 7

Darby, I. A., Laverdet, B., Bonté, F., and Desmoulière, A. (2014). Fibroblasts and myofibroblasts in wound healing. *Clinical, cosmetic and investigational dermatology*, 7:301. 18

Das Neves, R. P., Jones, N. S., Andreu, L., Gupta, R., Enver, T., and Iborra, F. J. (2010). Connecting variability in global transcription rate to mitochondrial variability. *PLoS biology*, 8(12):e1000560. 67

Dassule, H. R., Lewis, P., Bei, M., Maas, R., and McMahon, A. P. (2000). Sonic hedgehog regulates growth and morphogenesis of the tooth. *Development*, 127(22):4775–4785. 70

de Bruyn, J. R., van den Brink, G. R., Steenkamer, J., Buskens, C. J., Bemelman, W. A., Meisner, S., Muncan, V., Te Velde, A. A., D'Haens, G. R., and Wildenberg, M. E. (2018). Fibrostenotic phenotype of myofibroblasts in crohn's disease is dependent on tissue stiffness and reversed by lox inhibition. *Journal of Crohn's and Colitis*, 12(7):849–859. 19

DeCamp, S. J., Tsuda, V. M., Ferruzzi, J., Koehler, S. A., Giblin, J. T., Roblyer, D., Zaman, M. H., Weiss, S. T., Kılıç, A., De Marzio, M., et al. (2020). Epithelial layer unjamming shifts energy metabolism toward glycolysis. *Scientific Reports*, 10(1):18302. 41, 62, 63

Desousa, B. R., Kim, K. K., Jones, A. E., Ball, A. B., Hsieh, W. Y., Swain, P., Morrow, D. H., Brownstein, A. J., Ferrick, D. A., Shirihai, O. S., et al. (2023). Calculation of atp production rates using the seahorse xf analyzer. *EMBO reports*, 24(10):e56380. 46

Devany, J., Falk, M. J., Holt, L. J., Murugan, A., and Gardel, M. L. (2023). Epithelial tissue confinement inhibits cell growth and leads to volume-reducing divisions. *Developmental cell*, 58(16):1462–1476. 7

Devany, J., Sussman, D. M., Gardel, M., et al. (2019). Cell division rate controls cell shape remodeling in epithelia. *BioRxiv*, page 804294. 9

Deviri, D. and Safran, S. A. (2022). Balance of osmotic pressures determines the nuclear-to-cytoplasmic volume ratio of the cell. *Proceedings of the National Academy of Sciences*, 119(21):e2118301119. 81, 82

Di Gregorio, A., Bowling, S., and Rodriguez, T. A. (2016). Cell competition and its role in the regulation of cell fitness from development to cancer. *Developmental cell*, 38(6):621–634. 19

Discher, D. E., Janmey, P., and Wang, Y.-l. (2005). Tissue cells feel and respond to the stiffness of their substrate. *Science*, 310(5751):1139–1143. 19, 33

Divakaruni, A. S., Paradyse, A., Ferrick, D. A., Murphy, A. N., and Jastroch, M. (2014). Analysis and interpretation of microplate-based oxygen consumption and ph data. In *Methods in enzymology*, volume 547, pages 309–354. Elsevier. 46

Dobin, A., Davis, C., Schlesinger, F., Drenkow, J., Zaleski, C., Jha, S., Batut, P., Chaisson, M., and Gingeras, T. Star: ultrafast universal rna-seq aligner. bioin-formatics. 2013; 29: 15–21. 43

Earle, A. J., Kirby, T. J., Fedorchak, G. R., Isermann, P., Patel, J., Iruvanti, S., Moore, S. A., Bonne, G., Wallrath, L. L., and Lammerding, J. (2020). Mutant lamins cause nuclear envelope rupture and dna damage in skeletal muscle cells. *Nature materials*, 19(4):464–473. 82

Ebata, H. and Kidoaki, S. (2021). Avoiding tensional equilibrium in cells migrating on a matrix with cell-scale stiffness-heterogeneity. *Biomaterials*, 274:120860. 32

Efremov, A. K., Hovan, L., and Yan, J. (2022). Nucleus size and its effect on nucleosome stability in living cells. *Biophysical Journal*, 121(21):4189–4204. 89

Elitas, M. and Sengul, E. (2021). Optimization of u-net: convolutional networks for u87 human glioblastoma cell line segmentation. In *Emerging Topics in Artificial Intelligence (ETAI) 2021*, volume 11804, page 118041G. International Society for Optics and Photonics. 28

Esfahani, A. M., Rosenbohm, J., Safa, B. T., Lavrik, N. V., Minnick, G., Zhou, Q., Kong, F., Jin, X., Kim, E., Liu, Y., et al. (2021). Characterization of the strain-rate–dependent mechanical response of single cell–cell junctions. *Proceedings of the National Academy of Sciences*, 118(7):e2019347118. 33

Farhadifar, R., Röper, J.-C., Aigouy, B., Eaton, S., and Jülicher, F. (2007). The influence of cell mechanics, cell-cell interactions, and proliferation on epithelial packing. *Current biology*, 17(24):2095–2104. 13

Faubert, B., Solmonson, A., and DeBerardinis, R. J. (2020). Metabolic reprogramming and cancer progression. *Science*, 368(6487):eaaw5473. 62

Fletcher, A. G., Osterfield, M., Baker, R. E., and Shvartsman, S. Y. (2014). Vertex models of epithelial morphogenesis. *Biophysical journal*, 106(11):2291–2304. 67

Foster, H. A. and Bridger, J. M. (2005). The genome and the nucleus: a marriage made by evolution: genome organisation and nuclear architecture. *Chromosoma*, 114(4):212–229. 68

Franze, K., Gerdelmann, J., Weick, M., Betz, T., Pawlizak, S., Lakadamyali, M., Bayer, J., Rillich, K., Gögler, M., Lu, Y.-B., et al. (2009). Neurite branch retraction is caused by a threshold-dependent mechanical impact. *Biophysical journal*, 97(7):1883–1890. 19

Friedl, P. and Gilmour, D. (2009). Collective cell migration in morphogenesis, regeneration and cancer. *Nature reviews Molecular cell biology*, 10(7):445–457. 40

Friedrich, O., Merten, A.-L., Schneidereit, D., Guo, Y., Schürmann, S., and Martinac, B. (2019). Stretch in focus: 2d inplane cell stretch systems for studies of cardiac mechano-signaling. *Frontiers in Bioengineering and Biotechnology*, 7:55. 25

Fujii, Y., Ochi, Y., Tuchiya, M., Kajita, M., Fujita, Y., Ishimoto, Y., and Okajima, T. (2019). Spontaneous spatial correlation of elastic modulus in jammed epithelial monolayers observed by afm. *Biophysical journal*, 116(6):1152–1158. 27, 30, 31, 32, 38

Garcia, S., Hannezo, E., Elgeti, J., Joanny, J.-F., Silberzan, P., and Gov, N. S. (2015). Physics of active jamming during collective cellular motion in a monolayer. *Proceedings of the National Academy of Sciences*, 112(50):15314–15319. 5, 74

Gavara, N. (2017). A beginner's guide to atomic force microscopy probing for cell mechanics. *Microscopy research and technique*, 80(1):75–84. 19, 20

Gdula, M. R., Poterlowicz, K., Mardaryev, A. N., Sharov, A. A., Peng, Y., Fessing, M. Y., and Botchkarev, V. A. (2013). Remodeling of three-dimensional organization of the nucleus during terminal keratinocyte differentiation in the epidermis. *Journal of Investigative Dermatology*, 133(9):2191–2201. 90

Gehrels, E. W., Chakrabortty, B., Perrin, M.-E., Merkel, M., and Lecuit, T. (2023). Curvature gradient drives polarized tissue flow in the drosophila embryo. *Proceedings of the National Academy of Sciences*, 120(6):e2214205120. 3

Ghosh, S., Cuevas, V. C., Seelbinder, B., and Neu, C. P. (2021). Image-based elastography of heterochromatin and euchromatin domains in the deforming cell nucleus. *Small*, 17(5):2006109. 25

Godard, B. G. and Heisenberg, C.-P. (2019). Cell division and tissue mechanics. *Current opinion in cell biology*, 60:114–120. 9

Gómez-González, M., Latorre, E., Arroyo, M., and Trepat, X. (2020). Measuring mechanical stress in living tissues. *Nature Reviews Physics*, 2(6):300–317. 20

Gong, Z., Szczesny, S. E., Caliari, S. R., Charrier, E. E., Chaudhuri, O., Cao, X., Lin, Y., Mauck, R. L., Janmey, P. A., Burdick, J. A., et al. (2018). Matching material and cellular timescales maximizes cell spreading on viscoelastic substrates. *Proceedings of the National Academy of Sciences*, 115(12):E2686–E2695. 24

Goodrich, C. P., Liu, A. J., and Sethna, J. P. (2016). Scaling ansatz for the jamming transition. *Proceedings of the National Academy of Sciences*, 113(35):9745–9750. 6

Guelen, L., Pagie, L., Brasset, E., Meuleman, W., Faza, M. B., Talhout, W., Eussen, B. H., De Klein, A., Wessels, L., De Laat, W., et al. (2008). Domain organization of human chromosomes revealed by mapping of nuclear lamina interactions. *Nature*, 453(7197):948–951. 89

Guevorkian, K. and Maître, J.-L. (2017). Micropipette aspiration: A unique tool for exploring cell and tissue mechanics in vivo. In *Methods in cell biology*, volume 139, pages 187–201. Elsevier. 19

Guillot, C. and Lecuit, T. (2013). Mechanics of epithelial tissue homeostasis and morphogenesis. *Science*, 340(6137):1185–1189. 40

Guimarães, C. F., Gasperini, L., Marques, A. P., and Reis, R. L. (2020). The stiffness of living tissues and its implications for tissue engineering. *Nature Reviews Materials*, 5(5):351–370. 30

Gumbiner, B. M. (1996). Cell adhesion: the molecular basis of tissue architecture and morphogenesis. *Cell*, 84(3):345–357. 74

Han, Y., Glaser, S., Meng, F., Francis, H., Marzioni, M., McDaniel, K., Alvaro, D., Venter, J., Carpino, G., Onori, P., et al. (2013). Recent advances in the morphological and functional heterogeneity of the biliary epithelium. *Experimental Biology and Medicine*, 238(5):549–565. 74

Handorf, A. M., Zhou, Y., Halanski, M. A., and Li, W.-J. (2015). Tissue stiffness dictates development, homeostasis, and disease progression. *Organogenesis*, 11(1):1–15. 18, 19, 32, 34

Harris, A. R., Peter, L., Bellis, J., Baum, B., Kabla, A. J., and Charras, G. T. (2012). Characterizing the mechanics of cultured cell monolayers. *Proceedings of the National Academy of Sciences*, 109(41):16449–16454. 23, 27, 33

Hashemi-Beni, L. and Gebrehiwot, A. (2020). Deep learning for remote sensing image classification for agriculture applications. *The International Archives of Photogrammetry, Remote Sensing and Spatial Information Sciences*, pages 51–54. 28

Hoh, J. H. and Schoenenberger, C.-A. (1994). Surface morphology and mechanical properties of mdck monolayers by atomic force microscopy. *Journal of cell science*, 107(5):1105–1114. 20

Hsia, C.-R., McAllister, J., Hasan, O., Judd, J., Lee, S., Agrawal, R., Chang, C.-Y., Soloway, P., and Lammerding, J. (2022). Confined migration induces heterochromatin formation and alters chromatin accessibility. *Iscience*, 25(9):104978. 86

Hur, S. S., Del Alamo, J. C., Park, J. S., Li, Y.-S., Nguyen, H. A., Teng, D., Wang, K.-C., Flores, L., Alonso-Latorre, B., Lasheras, J. C., et al. (2012). Roles of cell confluency and fluid shear in 3-dimensional intracellular forces in endothelial cells. *Proceedings of the National Academy of Sciences*, 109(28):11110–11115. 76

Hutter, J., Chen, J., Wan, W., Uniyal, S., Leabu, M., and Chan, B. (2005). Atomic force microscopy investigation of the dependence of cellular elastic moduli on glutaraldehyde fixation. *Journal of microscopy*, 219(2):61–68. 30

Ilan, Y. (2023). Making use of noise in biological systems. *Progress in Biophysics and Molecular Biology*. 67

Isola, P., Zhu, J.-Y., Zhou, T., and Efros, A. A. (2017). Image-to-image translation with conditional adversarial networks. In *Proceedings of the IEEE conference on computer vision and pattern recognition*, pages 1125–1134. 28

Jain, N., Iyer, K. V., Kumar, A., and Shivashankar, G. (2013). Cell geometric constraints induce modular gene-expression patterns via redistribution of hdac3 regulated by actomyosin contractility. *Proceedings of the National Academy of Sciences*, 110(28):11349–11354. 63, 68, 86, 87

Jalali, S., Tafazzoli-Shadpour, M., Haghighipour, N., Omidvar, R., and Safshekan, F. (2015). Regulation of endothelial cell adherence and elastic modulus by substrate stiffness. *Cell communication & adhesion*, 22(2-6):79–89. 33

Kaelin, W. G. and McKnight, S. L. (2013). Influence of metabolism on epigenetics and disease. *Cell*, 153(1):56–69. 64

Kalukula, Y., Stephens, A. D., Lammerding, J., and Gabriele, S. (2022). Mechanics and functional consequences of nuclear deformations. *Nature Reviews Molecular Cell Biology*, 23(9):583–602. 68, 73, 82

Kamble, H., Barton, M. J., Jun, M., Park, S., and Nguyen, N.-T. (2016). Cell stretching devices as research tools: engineering and biological considerations. *Lab on a Chip*, 16(17):3193–3203. 32

Kasza, K. E., Supriyatno, S., and Zallen, J. A. (2019). Cellular defects resulting from disease-related myosin ii mutations in drosophila. *Proceedings of the National Academy of Sciences*, 116(44):22205–22211. 3

Khalilgharibi, N., Fouchard, J., Asadipour, N., Barrientos, R., Duda, M., Bonfanti, A., Yonis, A., Harris, A., Mosaffa, P., Fujita, Y., et al. (2019). Stress relaxation in epithelial monolayers is controlled by the actomyosin cortex. *Nature physics*, 15(8):839–847. 28, 33

Kiger, A., Baum, B., Jones, S., Jones, M., Coulson, A., Echeverri, C., and Perrimon, N. (2003). A functional genomic analysis of cell morphology using rna interference. *Journal of biology*, 2(4):1–15. 67

Kiyomitsu, T. (2015). Mechanisms of daughter cell-size control during cell division. *Trends in cell biology*, 25(5):286–295. 88

Koenderink, G. H., Dogic, Z., Nakamura, F., Bendix, P. M., MacKintosh, F. C., Hartwig, J. H., Stossel, T. P., and Weitz, D. A. (2009). An active biopolymer network controlled by molecular motors. *Proceedings of the National Academy of Sciences*, 106(36):15192–15197. 14

Kong, L., Lian, C., Huang, D., Hu, Y., Zhou, Q., et al. (2021). Breaking the dilemma of medical image-to-image translation. *Advances in Neural Information Processing Systems*, 34:1964–1978. 33

Kong, W., Loison, O., Chavadimane Shivakumar, P., Chan, E. H., Saadaoui, M., Collinet, C., Lenne, P.-F., and Clément, R. (2019). Experimental validation of force inference in epithelia from cell to tissue scale. *Scientific reports*, 9(1):1–12. 20

Krajnc, M. (2020). Solid–fluid transition and cell sorting in epithelia with junctional tension fluctuations. *Soft Matter*, 16(13):3209–3215. 9

Kreutzer, J., Ikonen, L., Hirvonen, J., Pekkanen-Mattila, M., Aalto-Setälä, K., and Kallio, P. (2014). Pneumatic cell stretching system for cardiac differentiation and culture. *Medical engineering & physics*, 36(4):496–501. 24, 34

Kubitschke, H., Schnauß, J., Nnetu, K. D., Warmt, E., Stange, R., and Kaes, J. (2017). Actin and microtubule networks contribute differently to cell response for small and large strains. *New Journal of Physics*, 19(9):093003. 33

Lange, J. R. and Fabry, B. (2013). Cell and tissue mechanics in cell migration. *Experimental cell research*, 319(16):2418–2423. 19

Langmead, B. and Salzberg, S. Fast gapped-read alignment with bowtie 2 nature methods. 2012; 9: 357–9. 43

Lee, L. M. and Liu, A. P. (2014). The application of micropipette aspiration in molecular mechanics of single cells. *Journal of nanotechnology in engineering and medicine*, 5(4). 19, 20

Lemière, J., Real-Calderon, P., Holt, L. J., Fai, T. G., and Chang, F. (2022). Control of nuclear size by osmotic forces in schizosaccharomyces pombe. *Elife*, 11:e76075. 81, 82, 83

Lemma, B. and Nelson, C. M. (2023). Spatial patterning of energy metabolism during tissue morphogenesis. *Current Opinion in Cell Biology*, 85:102235. 62

Li, Q., Kumar, A., Makhija, E., and Shivashankar, G. (2014). The regulation of dynamic mechanical coupling between actin cytoskeleton and nucleus by matrix geometry. *Biomaterials*, 35(3):961–969. 81

Li, Q., Makhija, E., Hameed, F. M., and Shivashankar, G. (2015). Micropillar displacements by cell traction forces are mechanically correlated with nuclear dynamics. *Biochemical and Biophysical Research Communications*, 461(2):372–377. 68

Lionetti, M. C., Bonfanti, S., Fumagalli, M. R., Budrikis, Z., Font-Clos, F., Costantini, G., Chepizhko, O., Zapperi, S., and La Porta, C. A. (2020). Chromatin and cytoskeletal tethering determine nuclear morphology in progerin-expressing cells. *Biophysical journal*, 118(9):2319–2332. 90

Liu, C., Yu, J., Song, A., Wang, M., Hu, J., Chen, P., Zhao, J., and Li, G. (2023). Histone h1 facilitates restoration of h3k27me3 during dna replication by chromatin compaction. *Nature Communications*, 14(1):4081. 85

Liu, G. (2019). Fea-ai and ai-ai: Two-way deepnets for real-time computations for both forward and inverse mechanics problems. *International Journal of Computational Methods*, 16(08):1950045. 28

Liu, Y., Mollaeian, K., and Ren, J. (2019). Finite element modeling of living cells for afm indentation-based biomechanical characterization. *Micron*, 116:108–115. 23

Loewe, B., Chiang, M., Marenduzzo, D., and Marchetti, M. C. (2020). Solid-liquid transition of deformable and overlapping active particles. *Physical Review Letters*, 125(3):038003. 8

Lu, J. (2019). The warburg metabolism fuels tumor metastasis. *Cancer and Metastasis Reviews*, 38:157–164. 40

Luciano, M., Versaevel, M., Vercruysse, E., Procès, A., Kalukula, Y., Remson, A., Deridoux, A., and Gabriele, S. (2022). Appreciating the role of cell shape changes in the mechanobiology of epithelial tissues. *Biophysics Reviews*, 3(1). 67

Luo, Q., Kuang, D., Zhang, B., and Song, G. (2016). Cell stiffness determined by atomic force microscopy and its correlation with cell motility. *Biochimica et Biophysica Acta (BBA)-General Subjects*, 1860(9):1953–1960. 30

Maître, J.-L., Niwayama, R., Turlier, H., Nédélec, F., and Hiiragi, T. (2015). Pulsatile cell-autonomous contractility drives compaction in the mouse embryo. *Nature cell biology*, 17(7):849–855. 20

Maître, J.-L., Turlier, H., Illukkumbura, R., Eismann, B., Niwayama, R., Nédélec, F., and Hiiragi, T. (2016). Asymmetric division of contractile domains couples cell positioning and fate specification. *Nature*, 536(7616):344–348. 20

Majmudar, T., Sperl, M., Luding, S., and Behringer, R. P. (2007). Jamming transition in granular systems. *Physical review letters*, 98(5):058001. 6

Makhija, E., Jokhun, D., and Shivashankar, G. (2016). Nuclear deformability and telomere dynamics are regulated by cell geometric constraints. *Proceedings of the National Academy of Sciences*, 113(1):E32–E40. 68

Marcus, P. I., Cieciura, S. J., and Puck, T. T. (1956). Clonal growth in vitro of epithelial cells from normal human tissues. *The Journal of experimental medicine*, 104(4):615–628. 67

Martin, L., Vicario, C., Castells-García, Á., Lakadamyali, M., Neguembor, M. V., and Cosma, M. P. (2021). A protocol to quantify chromatin compaction with confocal and super-resolution microscopy in cultured cells. *STAR protocols*, 2(4):100865. 85

Martin, M. (2011). Cutadapt removes adapter sequences from high-throughput sequencing reads. *EMBnet. journal*, 17(1):10–12. 43

Martin, R., Stroud, I., and Marshall, A. (1997). Data reduction for reverse engineering. *RECCAD, Deliverable Document 1 COPERNICUS project, No 1068*, page 111. 29

Mendez, M. G., Kojima, S.-I., and Goldman, R. D. (2010). Vimentin induces changes in cell shape, motility, and adhesion during the epithelial to mesenchymal transition. *The FASEB Journal*, 24(6):1838. 60

Michaelson, J., Choi, H., So, P., and Huang, H. (2012). Mechanical properties of primary and immortal fibroblasts in cell bi-layers. In *Summer Bioengineering Conference*, volume 44809, pages 685–686. American Society of Mechanical Engineers. 30

Mierke, C. T. The micropipette aspiration technique. 20

Mikołajczyk, A. and Grochowski, M. (2018). Data augmentation for improving deep learning in image classification problem. In *2018 international interdisciplinary PhD workshop (IIPhDW)*, pages 117–122. IEEE. 33

Miroshnikova, Y. A. and Wickström, S. A. (2022). Mechanical forces in nuclear organization. *Cold Spring Harbor Perspectives in Biology*, 14(1):a039685. 68

Mitchel, J. A., Das, A., O'Sullivan, M. J., Stancil, I. T., DeCamp, S. J., Koehler, S., Ocaña, O. H., Butler, J. P., Fredberg, J. J., Nieto, M. A., et al. (2020). In primary airway epithelial cells, the unjamming transition is distinct from the epithelial-to-mesenchymal transition. *Nature communications*, 11(1):5053. 5, 8, 58, 60, 61

Mongera, A., Rowghanian, P., Gustafson, H. J., Shelton, E., Kealhofer, D. A., Carn, E. K., Serwane, F., Lucio, A. A., Giammona, J., and Campàs, O. (2018). A fluid-to-solid jamming transition underlies vertebrate body axis elongation. *Nature*, 561(7723):401–405. 88

Moris, N., Pina, C., and Arias, A. M. (2016). Transition states and cell fate decisions in epigenetic landscapes. *Nature Reviews Genetics*, 17(11):693–703. 99

Moshe, M., Bowick, M. J., and Marchetti, M. C. (2018). Geometric frustration and solid-solid transitions in model 2d tissue. *Physical review letters*, 120(26):268105. 88

Mukherjee, R. N., Chen, P., and Levy, D. L. (2016). Recent advances in understanding nuclear size and shape. *Nucleus*, 7(2):167–186. 83, 89

Müller, D. J. and Dufrêne, Y. F. (2011). Atomic force microscopy: a nanoscopic window on the cell surface. *Trends in cell biology*, 21(8):461–469. 20

Munsky, B., Neuert, G., and Van Oudenaarden, A. (2012). Using gene expression noise to understand gene regulation. *Science*, 336(6078):183–187. 67

Murga, M., Jaco, I., Fan, Y., Soria, R., Martinez-Pastor, B., Cuadrado, M., Yang, S.-M., Blasco, M. A., Skoultchi, A. I., and Fernandez-Capetillo, O. (2007). Global chromatin compaction limits the strength of the dna damage response. *The Journal of cell biology*, 178(7):1101–1108. 85

Murphy, R. J., Buenzli, P. R., Baker, R. E., and Simpson, M. J. (2020). Mechanical cell competition in heterogeneous epithelial tissues. *Bulletin of Mathematical Biology*, 82(10):1–27. 19

Mustafa, A. and Mantiuk, R. K. (2020). Transformation consistency regularization–a semi-supervised paradigm for image-to-image translation. In *European Conference on Computer Vision*, pages 599–615. Springer. 33

Muzumdar, M. D., Tasic, B., Miyamichi, K., Li, L., and Luo, L. (2007). A global double-fluorescent cre reporter mouse. *genesis*, 45(9):593–605. 70

Neelam, S., Hayes, P. R., Zhang, Q., Dickinson, R. B., and Lele, T. P. (2016). Vertical uniformity of cells and nuclei in epithelial monolayers. *Scientific reports*, 6(1):19689. 74

Nehls, S., Nöding, H., Karsch, S., Ries, F., and Janshoff, A. (2019). Stiffness of mdck ii cells depends on confluency and cell size. *Biophysical journal*, 116(11):2204–2211. 30, 31, 32, 38

Niwayama, R., Moghe, P., Liu, Y.-J., Fabrèges, D., Buchholz, F., Piel, M., and Hiiragi, T. (2019). A tug-of-war between cell shape and polarity controls division orientation to ensure robust patterning in the mouse blastocyst. *Developmental cell*, 51(5):564–574. 90

Nobach, H. and Bodenschatz, E. (2009). Limitations of accuracy in piv due to individual variations of particle image intensities. *Experiments in fluids*, 47(1):27–38. 27

Ou, G., Stuurman, N., D'Ambrosio, M., and Vale, R. D. (2010). Polarized myosin produces unequal-size daughters during asymmetric cell division. *Science*, 330(6004):677–680. 88, 89

Ounkomol, C., Seshamani, S., Maleckar, M. M., Collman, F., and Johnson, G. R. (2018). Label-free prediction of three-dimensional fluorescence images from transmitted-light microscopy. *Nature methods*, 15(11):917–920. 27

O'hern, C. S., Silbert, L. E., Liu, A. J., and Nagel, S. R. (2003). Jamming at zero temperature and zero applied stress: The epitome of disorder. *Physical Review E*, 68(1):011306. 6

Pajic-Lijakovic, I. and Milivojevic, M. (2019). Long-time viscoelasticity of multicellular surfaces caused by collective cell migration–multi-scale modeling considerations. In *Seminars in Cell & Developmental Biology*, volume 93, pages 87–96. Elsevier. 28, 33

Palamidessi, A., Malinverno, C., Frittoli, E., Corallino, S., Barbieri, E., Sigismund, S., Beznoussenko, G. V., Martini, E., Garre, M., Ferrara, I., et al. (2019). Unjamming overcomes kinetic and proliferation arrest in terminally differentiated cells and promotes collective motility of carcinoma. *Nature materials*, 18(11):1252–1263. 64

Park, J.-A., Atia, L., Mitchel, J. A., Fredberg, J. J., and Butler, J. P. (2016). Collective migration and cell jamming in asthma, cancer and development. *Journal of cell science*, 129(18):3375–3383. 5, 62

Park, J.-A., Kim, J. H., Bi, D., Mitchel, J. A., Qazvini, N. T., Tantisira, K., Park, C. Y., McGill, M., Kim, S.-H., Gweon, B., et al. (2015). Unjamming and cell shape in the asthmatic airway epithelium. *Nature materials*, 14(10):1040–1048. 5, 47, 60

Pereira, D., Richert, A., Medjkane, S., Hénon, S., and Weitzman, J. B. (2020). Cell geometry and the cytoskeleton impact the nucleo-cytoplasmic localisation of the smyd3 methyltransferase. *Scientific reports*, 10(1):20598. 68

Perez Gonzalez, N., Tao, J., Rochman, N. D., Vig, D., Chiu, E., Wirtz, D., and Sun, S. X. (2018). Cell tension and mechanical regulation of cell volume. *Molecular biology of the cell*, 29(21). 74

Petridou, N. I., Corominas-Murtra, B., Heisenberg, C.-P., and Hannezo, E. (2021). Rigidity percolation uncovers a structural basis for embryonic tissue phase transitions. *Cell*, 184(7):1914–1928. 4, 7, 97

Petridou, N. I., Grigolon, S., Salbreux, G., Hannezo, E., and Heisenberg, C.-P. (2019). Fluidization-mediated tissue spreading by mitotic cell rounding and non-canonical wnt signalling. *Nature cell biology*, 21(2):169–178. 4

Pevsner-Fischer, M., Levin, S., and Zipori, D. (2011). The origins of mesenchymal stromal cell heterogeneity. *Stem Cell Reviews and Reports*, 7:560–568. 67

Phung, T.-K. N., Mitchel, J. A., O'Sullivan, M. J., and Park, J.-A. (2023). Quantification of basal stem cell elongation and stress fiber accumulation in the pseudostratified airway epithelium during the unjamming transition. *Biology Open*, 12(4):bio059727. 8

Pietuch, A., Brückner, B. R., Schneider, D., Tarantola, M., Rosman, C., Sönnichsen, C., and Janshoff, A. (2015). Mechanical properties of mdck ii cells exposed to gold nanorods. *Beilstein Journal of Nanotechnology*, 6(1):223–231. 30, 32, 38

Pinheiro, D., Kardos, R., Hannezo, É., and Heisenberg, C.-P. (2022). Morphogen gradient orchestrates pattern-preserving tissue morphogenesis via motility-driven unjamming. *Nature Physics*, 18(12):1482–1493. 4, 8

Plotnikov, S. V., Sabass, B., Schwarz, U. S., and Waterman, C. M. (2014). High-resolution traction force microscopy. In *Methods in cell biology*, volume 123, pages 367–394. Elsevier. 26

Polio, S. R., Stasiak, S. E., Jamieson, R. R., Balestrini, J. L., Krishnan, R., and Parameswaran, H. (2019). Extracellular matrix stiffness regulates human airway smooth muscle contraction by altering the cell-cell coupling. *Scientific reports*, 9(1):1–12. 19

Powell, K. (2019). These secret battles between your body's cells might just save your life. *Nature*, 574(7778):310–313. 19

Puliafito, A., Hufnagel, L., Neveu, P., Streichan, S., Sigal, A., Fygenson, D. K., and Shraiman, B. I. (2012). Collective and single cell behavior in epithelial contact inhibition. *Proceedings of the National Academy of Sciences*, 109(3):739–744. 74, 77

Ramdas, N. M. and Shivashankar, G. (2015). Cytoskeletal control of nuclear morphology and chromatin organization. *Journal of molecular biology*, 427(3):695–706. 82

Ramírez, F., Ryan, D. P., Grüning, B., Bhardwaj, V., Kilpert, F., Richter, A. S., Heyne, S., Dündar, F., and Manke, T. (2016). deeptools2: a next generation web server for deep-sequencing data analysis. *Nucleic acids research*, 44(Web Server issue):W160. 43

Ranft, J., Basan, M., Elgeti, J., Joanny, J.-F., Prost, J., and Jülicher, F. (2010). Fluidization of tissues by cell division and apoptosis. *Proceedings of the National Academy of Sciences*, 107(49):20863–20868. 9

Remmerbach, T. W., Wottawah, F., Dietrich, J., Lincoln, B., Wittekind, C., and Guck, J. (2009). Oral cancer diagnosis by mechanical phenotyping. *Cancer research*, 69(5):1728–1732. 19

Rens, R., Vahabi, M., Licup, A., MacKintosh, F., and Sharma, A. (2016). Nonlinear mechanics of athermal branched biopolymer networks. *The Journal of Physical Chemistry B*, 120(26):5831–5841. 14

Richardson, R. J., Hammond, N. L., Coulombe, P. A., Saloranta, C., Nousiainen, H. O., Salonen, R., Berry, A., Hanley, N., Headon, D., Karikoski, R., et al. (2014). Periderm prevents pathological epithelial adhesions during embryogenesis. *The Journal of clinical investigation*, 124(9):3891–3900. 76

Ridley, A. J. (2001). Rho gtpases and cell migration. *Journal of cell science*, 114(15):2713–2722. 57

Rinott, R., Jaimovich, A., and Friedman, N. (2011). Exploring transcription regulation through cell-to-cell variability. *Proceedings of the National Academy of Sciences*, 108(15):6329–6334. 67

Ritchie, M. E., Phipson, B., Wu, D., Hu, Y., Law, C. W., Shi, W., and Smyth, G. K. (2015). limma powers differential expression analyses for rna-sequencing and microarray studies. *Nucleic acids research*, 43(7):e47–e47. 43

Romero, A., Arbelaez, P., Van Gool, L., and Timofte, R. (2019). Smit: Stochastic multi-label image-to-image translation. In *Proceedings of the IEEE/CVF International Conference on Computer Vision (ICCV) Workshops*. 33

Ronneberger, O., Fischer, P., and Brox, T. (2015). U-net: Convolutional networks for biomedical image segmentation. In *International Conference on Medical image computing and computer-assisted intervention*, pages 234–241. Springer. 27

Ross, R., Everett, N. B., and Tyler, R. (1970). Wound healing and collagen formation: Vi. the origin of the wound fibroblast studied in parabiosis. *The Journal of cell biology*, 44(3):645–654. 4

Rotsch, C., Jacobson, K., and Radmacher, M. (1999). Dimensional and mechanical dynamics of active and stable edges in motile fibroblasts investigated by using atomic force microscopy. *Proceedings of the National Academy of Sciences*, 96(3):921–926. 30, 32

Sabass, B., Gardel, M. L., Waterman, C. M., and Schwarz, U. S. (2008). High resolution traction force microscopy based on experimental and computational advances. *Biophysical journal*, 94(1):207–220. 26

Sadati, M., Nourhani, A., Fredberg, J. J., and Taheri Qazvini, N. (2014). Glass-like dynamics in the cell and in cellular collectives. *Wiley Interdisciplinary Reviews: Systems Biology and Medicine*, 6(2):137–149. 5, 7

Sadhukhan, S. and Nandi, S. K. (2022). On the origin of universal cell shape variability in confluent epithelial monolayers. *Elife*, 11:e76406. 67, 81

Saw, T. B., Doostmohammadi, A., Nier, V., Kocgozlu, L., Thampi, S., Toyama, Y., Marcq, P., Lim, C. T., Yeomans, J. M., and Ladoux, B. (2017). Topological defects in epithelia govern cell death and extrusion. *Nature*, 544(7649):212–216. 68

Schaus, S. S. and Henderson, E. R. (1997). Cell viability and probe-cell membrane interactions of xr1 glial cells imaged by atomic force microscopy. *Biophysical journal*, 73(3):1205–1214. 32

Schneider, R. and Grosschedl, R. (2007). Dynamics and interplay of nuclear architecture, genome organization, and gene expression. *Genes & development*, 21(23):3027–3043. 68

Schoetz, E.-M., Lanio, M., Talbot, J. A., and Manning, M. L. (2013). Glassy dynamics in three-dimensional embryonic tissues. *Journal of The Royal Society Interface*, 10(89):20130726. 3

Schulze, K., Zehnder, S., Urueña, J., Bhattacharjee, T., Sawyer, W., and Angelini, T. (2017). Elastic modulus and hydraulic permeability of mdck monolayers. *Journal of Biomechanics*, 53:210–213. 23, 33

Seelbinder, B., Scott, A. K., Nelson, I., Schneider, S. E., Calahan, K., and Neu, C. P. (2020). Tenscell: imaging of stretch-activated cells reveals divergent nuclear behavior and tension. *Biophysical journal*, 118(11):2627–2640. 25, 34, 74

Serra-Picamal, X., Conte, V., Vincent, R., Anon, E., Tambe, D. T., Bazellieres, E., Butler, J. P., Fredberg, J. J., and Trepat, X. (2012). Mechanical waves during tissue expansion. *Nature Physics*, 8(8):628–634. 26

Serwane, F., Mongera, A., Rowghanian, P., Kealhofer, D. A., Lucio, A. A., Hockenbery, Z. M., and Campas, O. (2017). In vivo quantification of spatially varying mechanical properties in developing tissues. *Nature methods*, 14(2):181–186. 20

Shivashankar, G. (2011). Mechanosignaling to the cell nucleus and gene regulation. *Annual review of biophysics*, 40:361–378. 84

Siedlik, M. J., Manivannan, S., Kevrekidis, I. G., and Nelson, C. M. (2017). Cell division induces and switches coherent angular motion within bounded cellular collectives. *Biophysical journal*, 112(11):2419–2427. 9

Skinner, D. J., Song, B., Jeckel, H., Jelli, E., Drescher, K., and Dunkel, J. (2021). Topological metric detects hidden order in disordered media. *Physical Review Letters*, 126(4):048101. 67

Smith, P. C., Martínez, C., Martínez, J., and McCulloch, C. A. (2019). Role of fibroblast populations in periodontal wound healing and tissue remodeling. *Frontiers in physiology*, 10:270. 18

Sorba, F., Poulin, A., Ischer, R., Shea, H., and Martin-Olmos, C. (2019). Integrated elastomer-based device for measuring the mechanics of adherent cell monolayers. *Lab on a Chip*, 19(12):2138–2146. 19, 21, 33

Stachecka, J., Kolodziejski, P. A., Noak, M., and Szczerbal, I. (2021). Alteration of active and repressive histone marks during adipogenic differentiation of porcine mesenchymal stem cells. *Scientific Reports*, 11(1):1325. 84

Stark, R., Brown, G., et al. (2011). Diffbind: differential binding analysis of chip-seq peak data. *R package version*, 100(4.3). 43

Stooke-Vaughan, G. A. and Campàs, O. (2018). Physical control of tissue morphogenesis across scales. *Current opinion in genetics & development*, 51:111–119. 18

Storm, C., Pastore, J. J., MacKintosh, F. C., Lubensky, T. C., and Janmey, P. A. (2005). Nonlinear elasticity in biological gels. *Nature*, 435(7039):191–194. 14

Stringer, C., Wang, T., Michaelos, M., and Pachitariu, M. (2021). Cellpose: a generalist algorithm for cellular segmentation. *Nature methods*, 18(1):100–106. 44, 60, 71

Stroka, K. M. and Aranda-Espinoza, H. (2011). Effects of morphology vs. cell–cell interactions on endothelial cell stiffness. *Cellular and molecular bioengineering*, 4(1):9–27. 32

Struhl, K. (2007). Transcriptional noise and the fidelity of initiation by rna polymerase ii. *Nature structural & molecular biology*, 14(2):103–105. 67

Talia, S. D., Skotheim, J. M., Bean, J. M., Siggia, E. D., and Cross, F. R. (2007). The effects of molecular noise and size control on variability in the budding yeast cell cycle. *Nature*, 448(7156):947–951. 67

Tallman, J. A., Osusky, M., Magina, N., and Sewall, E. (2019). An assessment of machine learning techniques for predicting turbine airfoil component temperatures, using fea simulations for training data. In *Turbo Expo: Power for Land, Sea, and Air*, volume 58646, page V05AT20A002. American Society of Mechanical Engineers. 28

Tee, S.-Y., Fu, J., Chen, C. S., and Janmey, P. A. (2011). Cell shape and substrate rigidity both regulate cell stiffness. *Biophysical journal*, 100(5):L25–L27. 32, 33

Tennessen, J. M., Bertagnolli, N. M., Evans, J., Sieber, M. H., Cox, J., and Thummel, C. S. (2014). Coordinated metabolic transitions during drosophila embryogenesis and the onset of aerobic glycolysis. *G3: Genes, Genomes, Genetics*, 4(5):839–850. 62

Tetley, R. J., Staddon, M. F., Heller, D., Hoppe, A., Banerjee, S., and Mao, Y. (2019). Tissue fluidity promotes epithelial wound healing. *Nature physics*, 15(11):1195–1203. 5

Thattai, M. and Van Oudenaarden, A. (2004). Stochastic gene expression in fluctuating environments. *Genetics*, 167(1):523–530. 67

Thevenaz, P., Ruttimann, U. E., and Unser, M. (1998). A pyramid approach to subpixel registration based on intensity. *IEEE transactions on image processing*, 7(1):27–41. 22

Thielicke, W. and Sonntag, R. (2021). Particle image velocimetry for matlab: Accuracy and enhanced algorithms in pivlab. *Journal of Open Research Software*, 9(1). 23

Thiery, J. P., Acloque, H., Huang, R. Y., and Nieto, M. A. (2009). Epithelial-mesenchymal transitions in development and disease. *cell*, 139(5):871–890. 40

Thompson, A. J., Pillai, E. K., Dimov, I. B., Foster, S. K., Holt, C. E., and Franze, K. (2019). Rapid changes in tissue mechanics regulate cell behaviour in the developing embryonic brain. *Elife*, 8:e39356. 19

Thoumine, O. and Ott, A. (1997). Time scale dependent viscoelastic and contractile regimes in fibroblasts probed by microplate manipulation. *Journal of cell science*, 110(17):2109–2116. 28, 33

Tinevez, J.-Y., Perry, N., Schindelin, J., Hoopes, G. M., Reynolds, G. D., Laplantine, E., Bednarek, S. Y., Shorte, S. L., and Eliceiri, K. W. (2017). Trackmate: An open and extensible platform for single-particle tracking. *Methods*, 115:80–90. 71

Trappe, V., Prasad, V., Cipelletti, L., Segre, P., and Weitz, D. A. (2001). Jamming phase diagram for attractive particles. *Nature*, 411(6839):772–775. 7

Tsimring, L. S. (2014). Noise in biology. *Reports on Progress in Physics*, 77(2):026601. 67

Valero, C., Javierre, E., García-Aznar, J. M., and Gómez-Benito, M. J. (2014). A cell-regulatory mechanism involving feedback between contraction and tissue formation guides wound healing progression. *PloS one*, 9(3):e92774. 18

Varady, T., Martin, R. R., and Cox, J. (1997). Reverse engineering of geometric models—an introduction. *Computer-aided design*, 29(4):255–268. 29

Verstappe, J. and Berx, G. (2023). A role for partial epithelial-to-mesenchymal transition in enabling stemness in homeostasis and cancer. In *Seminars in Cancer Biology*, volume 90, pages 15–28. Elsevier. 4

Vichare, S., Inamdar, M. M., and Sen, S. (2012). Influence of cell spreading and contractility on stiffness measurements using afm. *Soft Matter*, 8(40):10464–10471. 32

Villaseñor, R. and Baubec, T. (2021). Regulatory mechanisms governing chromatin organization and function. *Current Opinion in Cell Biology*, 70:10–17. 85

Vincent, R., Bazellières, E., Pérez-González, C., Uroz, M., Serra-Picamal, X., and Trepat, X. (2015). Active tensile modulus of an epithelial monolayer. *Physical review letters*, 115(24):248103. 26

Wang, J. H.-C., Yang, G., and Li, Z. (2005). Controlling cell responses to cyclic mechanical stretching. *Annals of biomedical engineering*, 33(3):337–342. 32

Wang, N., Tolic-Nørrelykke, I. M., Chen, J., Mijailovich, S. M., Butler, J. P., Fredberg, J. J., and Stamenovic, D. (2002). Cell prestress. i. stiffness and prestress are closely associated in adherent contractile cells. *American Journal of Physiology-Cell Physiology*, 282(3):C606–C616. 19

Wang, X., Agrawal, V., Dunton, C. L., Liu, Y., Virk, R. K., Patel, P. A., Carter, L., Pujadas, E. M., Li, Y., Jain, S., et al. (2023). Chromatin reprogramming and bone regeneration in vitro and in vivo via the microtopography-induced constriction of cell nuclei. *Nature Biomedical Engineering*, pages 1–16. 68, 84

Wang, X., Merkel, M., Sutter, L. B., Erdemci-Tandogan, G., Manning, M. L., and Kasza, K. E. (2020). Anisotropy links cell shapes to tissue flow during convergent extension. *Proceedings of the National Academy of Sciences*, 117(24):13541–13551. 3

Wang, Y., Nagarajan, M., Uhler, C., and Shivashankar, G. (2017). Orientation and repositioning of chromosomes correlate with cell geometry–dependent gene expression. *Molecular biology of the cell*, 28(14):1997–2009. 68

Wang, Y., Pan, X., Song, S., Zhang, H., Huang, G., and Wu, C. (2019). Implicit semantic data augmentation for deep networks. *Advances in Neural Information Processing Systems*, 32. 33

Wei, S. C. and Yang, J. (2016). Forcing through tumor metastasis: the interplay between tissue rigidity and epithelial–mesenchymal transition. *Trends in cell biology*, 26(2):111–120. 18

Wells, R. G. (2013). Tissue mechanics and fibrosis. *Biochimica et Biophysica Acta (BBA)-Molecular Basis of Disease*, 1832(7):884–890. 19

Wiegand, C. and White, R. (2013). Microdeformation in wound healing. *Wound Repair and Regeneration*, 21(6):793–799. 18

Wilson, V. G. (2014). Growth and differentiation of hacat keratinocytes. *Epidermal Cells: Methods and Protocols*, pages 33–41. 69

Yamamoto, T., Sussman, D. M., Shibata, T., and Manning, M. L. (2022). Non-monotonic fluidization generated by fluctuating edge tensions in confluent tissues. *Soft Matter*, 18(11):2168–2175. 9

Yang, C., Ko, B., Hensley, C. T., Jiang, L., Wasti, A. T., Kim, J., Sudderth, J., Calvaruso, M. A., Lumata, L., Mitsche, M., et al. (2014). Glutamine oxidation maintains the tca cycle and cell survival during impaired mitochondrial pyruvate transport. *Molecular cell*, 56(3):414–424. 55

Yang, H., Pegoraro, A. F., Han, Y., Tang, W., Abeyaratne, R., Bi, D., and Guo, M. (2021). Configurational fingerprints of multicellular living systems. *Proceedings of the National Academy of Sciences*, 118(44):e2109168118. 3

Yeung, T., Georges, P. C., Flanagan, L. A., Marg, B., Ortiz, M., Funaki, M., Zahir, N., Ming, W., Weaver, V., and Janmey, P. A. (2005). Effects of substrate stiffness on cell morphology, cytoskeletal structure, and adhesion. *Cell motility and the cytoskeleton*, 60(1):24–34. 33

You, H. X. and Yu, L. (1999). Atomic force microscopy imaging of living cells: progress, problems and prospects. *Methods in cell science*, 21(1):1–17. 20

Zhang, T., Cooper, S., and Brockdorff, N. (2015). The interplay of histone modifications–writers that read. *EMBO reports*, 16(11):1467–1481. 84

Zhang, Y., Chen, J.-H., Chang, K.-T., Park, V. Y., Kim, M. J., Chan, S., Chang, P., Chow, D., Luk, A., Kwong, T., et al. (2019). Automatic breast and fibroglandular tissue segmentation in breast mri using deep learning by a fully-convolutional residual neural network u-net. *Academic radiology*, 26(11):1526–1535. 28

Zhang, Y., Liu, T., Meyer, C., Eeckhoute, J., Johnson, D., Bernstein, B., Nusbaum, C., Myers, R., Brown, M., Li, W., et al. (2008). Model-based analysis of chip-seq (macs). genome biol9: R137. *Jothi R, et al.(2008) Genome-wide identification of in vivo protein–DNA binding sites from ChIP-Seq data, Nucleic Acids Re36 (16)*, pages 5221–5231. 43

Zhang, Y., Wei, F., Poh, Y.-C., Jia, Q., Chen, J., Chen, J., Luo, J., Yao, W., Zhou, W., Huang, W., et al. (2017). Interfacing 3d magnetic twisting cytometry with confocal fluorescence microscopy to image force responses in living cells. *Nature protocols*, 12(7):1437–1450. 20

Zink, D., Fischer, A. H., and Nickerson, J. A. (2004). Nuclear structure in cancer cells. *Nature reviews cancer*, 4(9):677–687. 90